VNIVERSITAT DE VALÈNCIA

Departament de Física Atòmica, Molecular i Nuclear

Measurement of neutrino induced charged current neutral pion production cross section at SciBooNE.

TESI DOCTORAL
Joan Català Pérez

Directors:
Michel Sorel y
Juan José Gómez Cadenas
Tutor:
José Díaz Medina

Abstract

SciBooNE is a neutrino scattering experiment located in the Booster Neutrino Beam at Fermilab. It collected data from June 2007 to August 2008 to accurately measure muon neutrino and anti-neutrino cross sections on carbon around 1 GeV neutrino energy. In this thesis we present the results on the measurement of the muon neutrino cross section resulting in a μ^- plus a single π^0 final state ($CC-\pi^0$ channel). The present work will show the steps taken to achieve this result: from the reconstruction improvements to the background extraction. The flux-averaged $CC-\pi^0$ production cross section measurement obtained in this thesis $\langle\sigma_{\mathrm{CC}-\pi^0}\rangle_\phi = (5.6 \pm 1.9_{\mathrm{fit}} \pm 0.7_{\mathrm{beam}} \pm 0.5_{\mathrm{int}} - 0.7_{\mathrm{det}}) \times 10^{-40}$ cm^2/N at an average energy of 0.89 GeV is found to agree well both with the expectation from the Monte Carlo simulation and with a previous result from the MiniBooNE experiment.

Acknowledgments

Quiero agradecer profundamente a toda la gente que directa o indirectamente me ha ayudado a realizar esta tesis.

Antes de nada mis agradecimientos van a mis directores de tesis. A Juan José Gómez Cadenas, por darme la oportunidad de trabajar en su equipo y por contagiarme su pasión por los neutrinos, y a Michel Sorel por trabajar de cerca conmigo guiándome a cada paso, por sus consejos, por su paciencia y porque sin él esta tesis no hubiera podido ser.

Gracias a Ana María Tornero López y a Pau Novella Garijo, por ayudarme en los inicios de esta aventura y por llevarme de la mano en los mundos anglófonos cuando yo todavía no conocía el idioma. A Jordi Burguet por sus consejos linuxeros. A Elena Couce, Justo Martín-Albo, Francesc Monrabal, Raphaël Schroeter, Luis Serra, Lorena Escudero, Paola Ferrario y a todos los que han pasado por el despacho 1.9, por los buenos momentos en el despacho y fuera de él.

Quiero agradecer especialmente a Jose Luís Alcaraz Aunión su amistad y los buenos momentos pasados en los USA: los cafés en el High Rise cuando algo no salía, las Two Brothers en el dorm, el OnTheBorder, NY, SF, Miami, Las Vegas... No quiero olvidar a Gabriel Jover, que compartió con Jose y conmigo hamburguesas de búfalo y el viaje a NY. I really want to thank Paul Russo for his friendship, for his priceless help with ROOT, for the pizza & movie's at his place and for all the good moments we shared.

I want to thank all the people involved in SciBooNE experiment. I want to give special thanks to Morgan Wascko, co-spokesperson of SciBooNE, for his kindness and his advices, and for being the perfect host for the people from around the world that landed in FNAL. I really thank Tsuyoshi Nakaya, another SciBooNE co-spokesperson, Masashi Yokoyama, Lucio Ludovici, Camillo Mariani and Hide Tanaka for pointing out the weaknesses of my analysis and for helping me to solve them. Thanks to R. Napora for leading the work on the construction of the MRD. Many thanks to the SciBooNE

people that shared the 10th floor with me: Joe, Teppei, Nakaji, Yoshi, Hiraide, Takei and Claudio for sharing the hard work but also for being my friends, Chicago wouldn't be the same without you. I would like to thank all the people from MiniBooNE, our elder brother experiment for sharing shifts and work. Gracias también a Teppei Katori por estar siempre disponible para echar una mano o para irse de fiesta y a Natalie Walker por los buenos momentos. Gracias a Cristóbal, Bárbara, Kike, Ernest, Bruno y Miguel por hacer que incluso a 7.000 Km me sintiera en España compartiendo cervezas, jamón y escalada.

Tambien quiero acordarme aquí de Barber, Toni y Cesar, con los que empecé Física y que me han acompañado todos estos años, aunque solo nos veamos de vez en cuando para comer sushi.

Finalmente quiero agradecer encarecidamente a Neus, Emma, Mer, Loli y Pablo su amistad, porque el IFIC no hubiera sido lo mismo sin vosotros, os quiero. A Carmen Cabello, por ser mi editora y mi amiga. A Sergio Alarte y Oliver Mas por haber estado siempre ahí cuando los he necesitado. A mi hermano y mis padres por su paciencia y apoyo. Y a Andrea Sancho, la mujer de mi vida, porque su ilusión me ha dado fuerzas para terminar.

Joan Català
Nov. 2013

Contents

Resumen

En el presente trabajo de investigación se presenta la medida de la sección eficaz de producción de piones neutros a través de corriente cargada ($CC-\pi^0$) inducida por neutrinos muónicos en el experimento SciBooNE, situado en el Fermi National Accelerator Laboratory (FNAL) de Chicago.

SciBooNE es un experimento que utiliza el haz de neutrinos muónicos producidos en el Booster Neutrino Beam (BNB), el cual es utilizado también por MiniBooNE. Los protones acelerados en el Booster a una energía de 8 GeV se hacen colisionar con un blanco (target) de berilio. Esta colisión produce principalmente piones, los cuales son focalizados con ayuda de un cuerno (horn) magnético. El horn magnético nos permite seleccionar piones positivos o negativos, dependiendo de si queremos obtener un haz de neutrinos o de antineutrinos. Tras el blanco de berilio hay un túnel de desintegración de 50 m de longitud, en el que los piones positivos (negativos) se desintegran en dos partículas, un antimuón (muón) y un neutrino (antineutrino). Mientras los muones se detienen en el absorbente que hay al final del túnel, los neutrinos siguen su camino hacia el detector. Se pueden encontrar más detalles sobre SciBooNE en el Capítulo 2.

El detector de SciBooNE consta de tres subdetectores: SciBar, el Electron Catcher (EC) y el Muon Range Detector (MRD).

- SciBar es el detector principal de SciBooNE, el cual hace también las veces de blanco para los neutrinos. SciBar, detector usado anteriormente en el experimento K2K de Japón, consta de 14848 barras de plástico centelleador de $1.3 \times 2.5 \times 300$ cm^3 organizadas en 64 capas formando un cubo de $2.9 \times 2.9 \times 1.7$ m^3 y 15 toneladas de masa. Cada capa de centelleador está compuesta por dos planos de 116 barras cada uno con las barras dispuestas horizontal y verticalmente de manera alterna. Por el interior de las barras centelleadoras cruza una fibra que guía la luz generada hasta un fotomultiplicador multiánodo (MA-PMT por sus

siglas en inglés) de 64 canales. Por cada MA-PMT hay dos Time to Digital Converter (TDC), uno por cada 32 canales. La granularidad del detector junto con una buena resolución de la energía depositada en cada barra, hacen de SciBar un buen detector de trazas a la vez que un buen identificador de partículas.

- El EC es un calorímetro electromagnético situado inmediatamente detrás de SciBar. La misión del EC es recoger la energía de los fotones y electrones que escapan de SciBar. El EC consta de dos planos de 270×270 cm^2 con 32 módulos dispuestos en horizontal y vertical respectivamente. Cada módulo está compuesto de plomo y fibras centelleadoras. El EC tiene una anchura de 11 longitudes de radiación (11 X_0) y es capaz de absorber fotones y electrones por debajo de 2 GeV con una contención de la energía del 90%.
- Finalmente el MRD es un detector de muones situado detrás del EC. Está compuesto por 12 planchas de hierro de 5 cm de grosor intercaladas entre 13 planos de centelleador. Los 60 cm de grosor total de hierro son suficientes para detener muones de aproximadamente 1 GeV de energía con una resolución energética de unos 100 MeV. Las dimensiones de las planchas de hierro son $274 \times 305 \times 5$ cm^3.

SciBooNE tomó datos desde mediados de 2007 hasta mediados de 2008. En ese año de operación consiguió recopilar un total de $2.5 \cdot 10^{20}$ Protons On Target (POT) entre el modo neutrino y el modo antineutrino. POT es una medida que nos indica cuantos protones primarios interactuaron con el target para crear el haz de neutrinos, los POT son directamente proporcionales al número de neutrinos generados en el haz. Para el presente análisis solo se ha utilizado el modo neutrino con $0.99 \cdot 10^{20}$ POT. Se pueden encontrar más detalles del haz y de los detectores de SciBooNE en las Secciones 2.1 a 2.4.

La simulación de Monte-Carlo (MC) en la que se apoyan los análisis de SciBooNE, incluido el presente, estan realizadas con el generador de eventos de neutrinos NEUT para las interacciones de neutrinos con el detector y GEANT4 para la simulación del haz y los detectores así como las interacciones secundarias de las partículas generadas en la interacción de los neutrinos, llamadas interacciones del estado final (FSI por sus siglas en inglés). En el Capítulo 3 se verá la simulación de los detectores y de las interacciones al detalle.

Para la reconstrucción de los eventos en SciBar utiliza un algoritmo de celdas llamado SciBar Cellular Automaton Tracker (sbcat). Este algoritmo trabaja localizando en cada una de las vistas, horizontal y vertical, las barras por las que una partícula ha dejado señal, por cada una de las barras iluminadas tenemos una celda. Las celdas dentro de un mismo plano se agrupan en clústers y sbcat, siguiendo unas sencillas reglas recurrentes, conecta estos clústers longitudinalmente creando proyecciones de trazas. En un paso posterior, se hará el emparejamiento de las proyecciones entre las dos vistas para crear una traza tridimensional (3D-track). En las Secciones 4.4 y 4.5 veremos detalladamente la reconstrucción de trazas.

Para el presente análisis, la medida de la sección eficaz de producción de piones neutros a traves de corriente cargada inducida por neutrinos muónicos, primero tenemos que caracterizar el tipo de eventos que vamos a observar. Los eventos $CC - \pi^0$ se producen principalmente a través de la producción de una resonancia Δ y su posterior desintegración ($\nu_\mu + n \rightarrow \mu + \Delta^+$; $\Delta^+ \rightarrow p + \pi^0$) o a través de una colisión profundamente inelástica (DIS por sus siglas en inglés) en la que se producen varios piones ($\nu_\mu + n \rightarrow p + \mu + multi\ \pi$).

En este análisis, los eventos de señal están caracterizados por un muón y un pión neutro que escapan del núcleo de interacción. Dado que los piones neutros se desintegran a dos fotones casi inmediatamente, la topología típica de los eventos $CC - \pi^0$ en SciBar será de tres trazas, una de ellas, correspondiente al muón deberá alcanzar el MRD y las otras dos que corresponderán a las dos cascadas electromagnéticas provocadas por los dos fotones. En este análisis también están permitidos los eventos que tengan más de tres trazas, estas trazas extra pueden corresponder a protones o piones cargados y serán ignoradas.

Ciñéndonos a la topología de los eventos $CC - \pi^0$ se han diseñado una serie de cortes con el propósito de seleccionar este tipo de eventos. Con la ayuda del MC se ha estudiado cada corte de selección para maximizar la eficiencia a la vez que la pureza de la muestra.

Los cortes aplicados a la muestra de eventos son los siguientes:

- Al menos una traza de SciBar emparejada (matched) con otra en el MRD. Esta traza será considerada como el muón, dado que el muón deja en SciBar una traza muy bien definida y se genera en el vértice de interacción, el inicio de la traza se considerará el vértice de interacción. A las trazas de SciBar emparejadas con el MRD se las llama MRD-matched tracks. En la Sección 4.6 se discutirá el emparejamiento de trazas de manera pormenorizada. Hay tres requisitos que deben cumplir las trazas para emparejarse:
  - Una traza de SciBar apuntando a una traza del MRD. La proyección hacia el MRD de la traza en SciBar debe quedar a menos de 10 cm

    del inicio de la traza en el MRD y con un ángulo entre ellas lo suficientemente pequeño para que las dos trazas puedan ser combinadas en una sola.

  - El vértice de interacción debe estar dentro del Volumen Fiducial (FV por sus siglas en inglés). Es decir, la traza de SciBar candidata a emparejarse con el MRD debe tener su inicio en el volumen definido por -130 cm $< X, Y <$ 130 cm and 2.62 cm $< Z <$ 157.2 cm. Este requisito rechaza eventos que se hayan generado en el exterior del detector y los rayos cósmicos, los cuales son considerados ruido (background) en este análisis.
  - Las trazas candidatas a emparejarse deben generarse dentro de la ventana temporal del haz. Este requisito ayuda también a reducir el background generado por los rayos cósmicos.

- Un solo muón en el evento. Este corte se aplica para evitar ambigüedades en la posición del vértice de interacción.

- El tiempo en el que aparecen las trazas debe estar en una ventana de 20 ns alrededor del tiempo de la traza del muón.

- Al menos 2 candidatos a fotones. Dado que necesitamos reconstruir los piones neutros, debemos encontrar al menos dos trazas que sean compatibles con las cascadas electromagnéticas que producen los fotones. Dependiendo de la reconstrucción clasificamos los candidatos a fotones de tres maneras distintas: contenidos en SciBar, si las trazas empiezan y terminan dentro de SciBar, iniciados en SciBar, si las trazas empiezan en SciBar pero alcanzan el EC, y contenidas en el EC. Para que una traza sea considerada un candidato a fotón, debe cumplir los siguientes requisitos:

  - Las trazas deben estar contenidas en SciBar. Las trazas candidatas a fotones no deben terminar cerca de los bordes del detector excepto para las que se dirigen hacia el EC. Para conseguir una buena resolución en la energía del pión neutro es necesario detectar toda la energía de los fotones, con este corte se rechazan los fotones de los que no se ha recuperado toda su energía. Además, dado que en este análisis todas las trazas se suponen que emanan del vértice de interacción este corte cumple otra función, rechazar trazas que provengan de interacciones que se hayan producido fuera del detector.

  - Muon Confidence Level (MuCL). El nivel de confianza del muón (MuCL por sus siglas en inglés) es una cantidad que caracteriza una partícula por su energía depositada por unidad de longitud de la traza dE/dx y nos indica cuán similar es su traza a una traza producida por un muón. La ecuación para calcular el MuCL de una partícula la podemos encontrar en la Sección 4.6. Un MuCL cercano a 1 nos indica que la partícula es una MIP (Minimum Ionizing Particle) y por tanto que es parecida a un muón en términos de deposición de energía, mientras que un MuCL cercano a 0 nos indica que la partícula es similar a un protón. Aunque esperamos que los candidatos a fotones tengan un MuCL cercano a 1, hemos situado el corte en MuCL > 0.005 porque de este modo se rechazan la mayor parte de los protones y podemos usar los siguientes cortes para rechazar otras partículas como los piones cargados.
  - Desconexión. La mayor parte de los protones y piones cargados presentes en los eventos proceden del vértice de interacción y su traza se inicia en el mismo vértice. Los fotones, por otro lado, viajan de media una longitud de interacción (40 cm en SciBar) antes de interaccionar con el detector y producir una señal visible. Para discriminar entre trazas producidas por fotones y trazas producidas por otras partículas se pide que el inicio de la traza candidata a fotón se inicie a una distancia mínima del vértice de interacción de 12 cm.
  - Energía mínima en el EC. Para los fotones que no dejan traza en SciBar y están únicamente contenidos en el EC se pide que la energía depositada en el primer plano del EC sea al menos de 15 MeV.

- Un solo candidato a pión neutro. Para reconstruir piones neutros necesitamos al menos 2 candidatos a fotones. A través de la energía y del ángulo respecto del haz de los fotones, somos capaces de reconstruir el momento y la masa del pión neutro así como el punto de desintegración del pión y el ángulo respecto del haz. Además, se ha observado que cuando los candidatos a fotones tienen un ángulo pequeño entre ellos la masa reconstruida del candidato a pión neutro resulta muy pequeña. Esto es debido a que en la mayor parte de estos casos lo que ocurre es que un solo fotón se reconstruye como 2 trazas separadas con pequeño ángulo entre ellas, dando lugar a piones neutros mal reconstruidos o directamente reconstruyendo piones neutros en eventos donde no los hay. Por este motivo, para reconstruir un candidato a pión neutro se exige que el coseno del ángulo entre los dos fotones usados para reconstruirlo sea menor o igual a 0.95.

Con esta selección de eventos llegamos a una muestra final de 308 eventos obteniendo una eficiencia en la selección y una pureza de la muestra del 2.08% y del 38.23% respectivamente. En la Tabla 5.1.1 se pueden observar los efectos de cada corte con más detalle.

Dado que la pureza de la muestra sigue siendo relativamente baja, el siguiente paso ha sido realizar un ajuste del MC a los datos con tal de hacer una extracción del background de la muestra. El ajuste se realiza aprovechando las diferencias en las distribuciones de algunas variables entre la señal y los diferentes tipos de background. El ajuste se realiza a través de una minimización del χ^2 sobre dos variables simultáneamente. Estas variables son la masa reconstruida del pión neutro, que nos ayudará a distinguir entre la señal y el ruido que no contiene piones neutros, y la distancia entre el vértice del evento y la posición reconstruida del pión neutro, que nos ayudará a distinguir entre la señal y los eventos en los que habiendo un pión neutro, este se genera fuera del núcleo de interacción a través de FSI. Los detalles del ajuste los podemos encontrar en la Sección 5.3 y el resultado del ajuste se puede observar en la Tabla 5.3.1.

Finalmente, con la muestra seleccionada de 308 eventos y habiendo ajustado el MC a los datos, nos encontramos en posición de extraer la medida de la sección eficaz de producción de piones neutros a través de corriente cargada inducida por neutrinos muónicos. El cálculo de la sección eficaz se realiza utilizando la Ecuación 5.5.2, que podemos encontrar en la Sección 5.5. Esta ecuación toma la fracción de señal que hemos calculado gracias al ajuste corregida por la eficiencia de los cortes y la divide entre el producto del flujo de neutrinos que cruzan el volumen fiducial del detector y del numero de nucleones que contiene el detector en el mismo FV. Para el flujo de neutrinos solo hemos tenido en cuenta aquellos con una energía mayor de 370 MeV, ya que esta es la energía mínima para la producción de piones neutros.

Tras el cálculo de la sección eficaz de $CC - \pi^0$ dedicaremos el Capítulo 6 al análisis de los errores sistemáticos que pueden afectar a la medida. Las fuentes de errores sistemáticos se dividen en tres grandes bloques: las incertidumbres asociadas al haz, las asociadas a los detectores y las asociadas a las interacciones de los neutrinos.

- Las incertidumbres asociadas al haz pueden afectar al flujo de neutrinos. Los errores sistemáticos asociados al haz que han sido estudiados son:
    - Entrega de protones. Se estudian las incertidumbres en la intensidad del haz de protones así como la óptica del haz, los cuales pueden afectar a la predicción de los POT y por tanto a la normalización general del flujo.

  - Producción de partículas en el target. Las incertidumbres en la producción de piones y kaones en el target afectan a la composición del haz de neutrinos así como a su espectro de energías.
  - Campo magnético del horn e interacciones hadrónicas en el horn o el target. Las incertidumbres en el campo magnético del horn y en las posibles reinteracciones de los hadrones en el propio target o dentro del horn pueden afectar también al espectro de energías del haz de neutrinos.

  En la Tabla 6.1.1 se pueden observar los resultados del análisis de los errores sistemáticos asociados al haz.

- Las incertidumbres asociadas a la interacción de los neutrinos pueden afectar a la predicción de las características de la señal frente al ruido y por tanto al resultado del ajuste. Para calcular el error sistemático asociado a las interacciones de neutrinos, se evalúa por separado el efecto de las incertidumbres en los parámetros utilizados por el modelo teórico en el que se basa la simulación de MC. Los parámetros evaluados se pueden ver en la Tabla 6.2.1 y el resultado de la evaluación en la Tabla 6.2.2.

- Las incertidumbres asociadas a la respuesta de los detectores pueden afectar de distintas formas a cómo los eventos son reconstruidos. Hay cinco características del detector SciBar que han sido analizadas:

  - X-talk es el nombre que recibe el cruce de señal entre dos fibras aledañas conectadas al mismo MA-PMT. En este efecto, parte de la luz salta de una fibra a otra creando celdas fantasma. Este efecto incrementa el ruido alrededor de las trazas y puede provocar el mal funcionamiento de sbcat y la reconstrucción de trazas erróneas. Para evaluar este error, se ha aplicado una variación de $\pm 1\sigma$ a los valores medidos del cruce de señal.
  - Constante de Birk. La luz producida en un centelleador no es directamente proporcional a la energía depositada por la partícula que lo atraviesa, sino que sigue la ley de Birk. Un error en la medida de la constante de Birk puede afectar a la reconstrucción de la energía de las partículas. La constante de Birk medida para los centelleadores de SciBar es $0.0208 \pm 0.0023\ cm/MeV$ y se ha aplicado una variación de 1σ a este valor para evaluar este sistemático.

- El nivel umbral de foto-electrones (p.e.) para considerar una celda. Una variación en dicho umbral puede afectar tanto a la reconstrucción de las trazas como a la reconstrucción de la energía. El umbral para considerar que por una barra ha cruzado una partícula está situado en 2 p.e. pero se ha medido, usando rayos cósmicos, que la constante de conversión de foto-electrones a energía depositada puede variar hasta un 20% de un canal a otro. De este modo, se han estudiado los efectos de una variación del 20% en el umbral de photo-electrons (p.e.)
- La resolución del MA-PMT para un solo foto-electrón. En la medida de la resolución realizada en el laboratorio se ha obtenido un valor del 70% de resolución mientras que para reproducir correctamente los rayos cósmicos en la simulación de MC se ha asignado un valor para la resolución del 50%. Para cubrir esta diferencia se ha evaluado una variación del 20% en la resolución del PMT.
- El tiempo muerto del TDC es de 55 ns $\pm$ 20 ns. Para evaluar esta fuente de incertidumbre, se ha aplicado una variación de 1σ.

El resultado del cálculo de la sección eficaz junto con los errores sistemáticos calculados se puede encontrar en el Capítulo 7 donde también se muestra la cinemática de las partículas producidas en los eventos, así como la reconstrucción de la energía del neutrino incidente para una sub-muestra de los datos.

La sección eficaz de $CC-\pi^0$ inducida por neutrinos, teniendo en consideración todos los errores se puede encontrar en la Sección 7.1, Ecuación 7.1.1 a una energía promedio de 0.89 GeV. También el la Sección 7.1 encontraremos la comparación de los resultados del presente análisis con la predicción del MC y con el resultado previo del experimento MiniBooNE. La comparación del resultado con MiniBooNE es bastante directa dado que ambos experimentos utilizan el mismo haz de neutrinos y la composición del blanco del detector principal es muy similar CH para SciBooNE comparado con CH_2 para MiniBooNE.

También la definición de la señal es similar entre ambos experimentos. La señal en MiniBooNE se define como un muón y un pión neutro saliendo del núcleo de interacción, con cualquier número de nucleones pero sin otros mesones en el evento, mientras que en SciBooNE si que se permiten otros mesones en el evento siempre que no sean otros piones neutros. Esta diferencia hace que la señal en SciBooNE sea ligeramente más inclusiva aunque, de acuerdo con las simulaciones de NEUT, la diferencia entre las dos definiciones de señal es muy pequeña a las energías en las que SciBooNE y MiniBooNE hacen su medida.

En la Tabla 7.1.1 se puede observar que los resultados de MiniBooNE y SciBooNE son consistentes entre ellos. Este acuerdo entre los resultados incrementa la confianza en ambos experimentos dadas las diferencias tecnológicas entre los detectores de los dos experimentos. Mientras que MiniBooNE cuenta con la ventaja de una mayor estadística, lo que le permite hacer una medida de la sección eficaz en función de la energía del neutrino, SciBooNE, que cuenta con solo un valor en la medida, tiene la ventaja de apoyarse en una tecnología que le permite una reconstrucción de eventos mucho más detallada y con ello una manera independiente y probablemente más confiable de entender la normalización general de la sección eficaz de $CC - \pi^0$ y proporcionando con esto un punto de anclaje para la medida de MiniBooNE.

Finalmente, se ha estudiado también la cinemática de producción de particulas tanto para muones como para los piones neutros el los eventos $CC - \pi^0$ comparándola con la predicción del MC. Como se puede ver en la Sección 7.3 el acuerdo entre los datos y el MC es muy bueno para todas las cantidades reconstruidas, más aún después de haber ajustado las normalizaciones de la señal y del background utilizando los parámetros del ajuste expuesto anteriormente.

Chapter 1

Introduction: Neutrinos for Beginners

1.1 What is a neutrino? The 'not so technical' explanation.

Neutrino is an elementary particle related to the electron. Neutrinos are almost massless and have no electrical charge.

In the sub-atomic world, there are three families of elementary particles, each family composed of four particles as can be seen in Table 1.1.1. The only difference between the families is the mass of the particles that compose them, keeping the same other particle properties, as the electrical charge. The lightest family is composed by two leptons, the neutrino and the electron, and two quarks, the quark up and the quark down. All the matter we know, can be built with just the particles of the first family. The quarks are the elementary particles that, combined, form the protons and neutrons who live in the atomic nucleus, and many other particles. Because of the greater mass, the particles of the second and third family needs more energy to be created. The particles of the second and third families can be seen as 'big brothers' of the particles of the first family.

Besides this plot, we have to add the anti-particles. Each one of the quarks and leptons has a twin particle with the same mass and properties except for the charge, which is the opposite. The world we interact with is composed only by particles. To find an anti-particle we need to look at some matter

Family:	I	II	III
Quarks:	up (u)	charm (c)	top (t)
	down (d)	strange (s)	bottom (b)
Leptons:	electron (e)	muon (μ)	tau (τ)
	electron neutrino (ν_e)	muon neutrino (ν_μ)	tau neutrino (ν_τ)

Table 1.1.1: *Elemenrary particles divided in families. Particles in the same row share the same properties in each family except for the mass.*

radioactivity, the cosmic rays or particle collisions at particle accelerators.

Neutrinos are the tiniest known particles. In the sub-atomic world, tiny means small probability of interaction. If we are able to visualize the atomic world full of 'little balls', we can say that neutrinos are so tiny that they can pass through the pores of such balls and they can cross even the atomic nucleus without hitting anything. To give a number, only one of each $\sim 10^{40}$ of the neutrinos that comes from the sun will hit an atom on the earth. This is a 0.00000000000000000000000000000000000001% of chances that a single neutrino hits another particle.

Why is that? There are four forces that govern the universe: gravitation, electromagnetism, and the nuclear strong and weak forces. Gravitation and electromagnetism are well known forces. All the particles which have mass are affected by gravitation, and all the particles that have an electrical charge are affected by electromagnetism. What you may not know is what the strong and weak forces do.

As explained before, among the elementary particles, there are leptons (electron and neutrino) and quarks. The difference between those two kinds of particles is which force affects them. While quarks are affected by both weak and strong forces (apart from electromagnetism and gravitation), leptons are only affected by the weak force. The strong force is responsible of keeping together the quarks inside protons and neutrons, and in general the hadrons which are the kind of particles that are composed by quarks. The hadrons are divided into baryons, the particles that are composed by 3 quarks like protons and neutrons, and mesons, the particles composed by 2 quarks like pions and kaons. On the other hand, the weak force is responsible of a nuclear decay called beta decay, in which a neutron transmutes into a proton and an electron and, as we know now, also a neutrino.

Strong and weak forces, unlike gravitation and electromagnetism, have a very small radius of action: the particles have to be very close to each other in order to feel these forces. Given that neutrinos are almost massless and have no electric charge, they are not affected by gravitation and electromagnetism. And given the nature of the neutrinos, which are leptons, they are not affected by strong force either. Then, neutrinos are the only particles that are only affected by the weak force, and therefore the small probability of interaction.

Because of this small probability of interaction, neutrino detection is a tough work. We need to produce lots of neutrinos in order to be able to detect few of them. By analyzing those few detected neutrinos we can infer the neutrino properties and characteristics.

There are three different neutrinos. Since the electron-like particle of the second family receives the name of muon and the one of the third receives the name tau, the neutrinos of each family are called electron neutrino, muon neutrino and tau neutrino. We know they are different because different processes produce different neutrinos and different experiments are needed to study them. For instance, the totality of the neutrinos produced inside the sun are electron neutrinos, the ones from the first family. On the other hand, neutrinos produced when a cosmic ray hits the atmosphere are more commonly muon neutrinos. The tau neutrinos appear in high energy processes where a tau particle can also be created.

Also artificial sources of neutrinos are used in order to have large amounts of neutrinos crossing a detector, allowing to analyze their characteristics. Those sources are nuclear reactors from nuclear power plants, which generate electron neutrinos in each nuclear fission, and particle accelerators which are able to generate, in a way I will explain later on, a beam of muon neutrinos.

Many experiments use accelerator neutrinos and dedicated detectors in order to study the neutrino characteristics and also the way neutrinos interact with matter. Not all the collisions between neutrinos and atoms lead to the same result. Neutrinos may hit an electron knocking it out of the atom with the neutrino continuing almost unaltered, or a muon neutrino may hit a neutron inside the nucleus converting the neutron into a proton and the neutrino into a muon. Also anti-neutrinos interact with matter in many ways, one of them is the process called inverse beta decay. From the reaction just two particles may come out or many of them. This also depends on how energetic is the neutrino involved. All those processes must be fully understood and it has to be known how often each one of them occurs. This is the field SciBooNE [1] is working on. In particular, the process in which a neutrino hits a neutron and produces a muon, a proton, and a particle called neutral pion, is the focus of this thesis.

Neutrinos have an even more outstanding characteristic, neutrinos are able to change their nature and 'jump' from one family into another. This is called oscillation of the neutrino flavour. Oscillation implies that an electron neutrino that comes out from the sun can reach the earth as a muon neutrino. Nowadays there are many experiments studying the oscillating behavior of the neutrinos.

1.2 Brief history of the neutrinos.

Neutrinos were first proposed in 1930 by W. Pauli [2] to save the energy conservation in the beta decay. The beta decay is a process that occurs in the atomic nuclei. In the process, one of the neutrons of the nucleus decays into a proton and an electron and also, as Pauli proposed, a neutrino (technically an antineutrino). Pauli proposal was outstanding at that time because he was proposing a particle he thought at the moment undetectable. It was Enrico Fermi who, using the particle Pauli proposed, wrote the equations that correctly describes the beta decay through the weak interactions [3].

The electron neutrino was first detected in 1954 by Reines and Cowan [4] placing a tank of water with liquid scintillator and cadmium chloride near a nuclear reactor. They were able to detect up to three neutrinos per hour.

Between the theoretical proposal of the electron neutrino and its discovery, the muon neutrino was proposed by Shoichi Sakata to explain another decay, the pion decay into a muon [5]. In this process, similar to what happens with the neutron decay, a neutrino is emitted together with the muon. It was not until 1962 that the muon neutrino was detected and distinguished from the electron neutrino in a particle accelerator [6].

In 1968 Davis succeeded in detecting neutrinos coming from the sun using a tank of chlorine [7]. This was the first measurement of neutrinos coming from a natural source. He measured a neutrino flux that was much lower than the one predicted by the astronomical solar models. It was a rather complicated experiment and this led to different possibilities: The model was wrong, the experiment was wrong or something happened to the neutrinos while travelling. The lack of observed solar neutrinos reaching the earth was called the “solar neutrino problem”.

The neutrino oscillation was proposed to solve the solar neutrino problem. The neutrino oscillation was first proposed by Bruno Pontecorvo [8], but the first approach was a neutrino-antineutrino oscillation. This approach turned out to be wrong. The neutrino flavor oscillation was proposed some years later by Ziro Maki, Masami Nakagawa and S. Sakata [9]. Oscillations can only occur if the different neutrinos have different masses. Then, the oscillation of the neutrinos imply that the neutrinos are not massless but have a tiny mass. The change of the electron neutrinos into muon and tau neutrinos, that is the oscillations, finally solved the solar neutrino problem. Davis was only able to measure electron neutrinos, not muon nor tau neutrinos, so that in his experiment he only saw the neutrinos that have not oscillated and arrived as electron neutrinos.

The tau lepton was discovered in 1976 [10]. Its analysis led to the conclusion that there should be also a tau neutrino, which was not yet observed at that time.

The second natural neutrino source to be studied was atmospheric neutrinos. Atmospheric neutrinos are the neutrinos produced by the cosmic ray radiation interacting with the atmosphere. Most of the atmospheric neutrinos are muon neutrinos. The first detectors that detected them, IMB [11], placed in USA, and Kamiokande [12], placed in Japan, were built in the early 80's for a different mission: to detect the possible proton decay. Those massive water tanks turned out to be great neutrino detectors. Those detectors were able to detect solar electron neutrinos but also atmospheric muon neutrinos. Those detectors found what was called the "atmospheric neutrino anomaly", which is a deficit of the detected muon neutrinos compared with the theoretical prediction. The answer to the atmospheric neutrino anomaly turned out to be the same as the neutrino solar problem. Between them relies a difference of scale. The differences in mass composition of the different neutrinos cause the electron neutrino to oscillate into muon and tau neutrinos in a different way and proportion than the muon neutrinos oscillate into the tau and electron neutrinos. Given a neutrino energy, the probability of a neutrino changing flavor depends on the distance travelled.

Kamiokande and IMB were also the first neutrino telescopes by detecting neutrinos from the Supernova 1987A [13, 14].

In 1996, Super-Kamiokande [15] started taking data. This is the largest neutrino detector ever made. It consists of a tank of 50.000 tons (50 kT) of ultra pure water. This detector and its capacity to reconstruct the incoming direction of the neutrinos was able to measure oscillations of the atmospheric muon neutrinos. This was the needed proof to ensure that neutrinos have mass.

The importance of the directionality of the measurements is that it has been found that the oscillations depend on the energy of the neutrinos but also on the distance travelled by the neutrinos. This means that the oscillation pattern of the neutrinos coming from the zenith of the detector, which have traveled about 10 km, will be different from the one of the neutrinos coming from below, having travelled about 13.000 km, and both will be different from the ones of the intermediate distances that depend on the angle in which the neutrino arrives to the detector. This is the fact that allowed the Super-Kamiokande collaboration to confirm the muon neutrino oscillations.

In 2000, the DONUT collaboration announced the first direct evidence of the tau neutrinos [16].

In 2001 the SNO experiment [17] gives the proof for the solution of the solar neutrino problem by measuring at the same time neutrino interactions sensitive to the electron neutrinos and neutrino interactions sensitive to all kinds of neutrinos, finding the expected amount of interactions in the last case while finding an amount compatible with the Davis experiment of electron neutrinos.

In 2002 KamLAND [18] measures electron neutrino oscillations from nuclear reactions, confirming the solution to the solar neutrino problem using a different neutrino source than SNO.

In the last decade, long baseline experiments using accelerator produced neutrino beam like K2K [19] and MINOS [20] and T2K [21] also confirm muon neutrino oscillation.

Results from Daya Bay [22] and RENO [23] reactor experiments and T2K and MINOS accelerator experiments confirmed the 3-flavor oscillation by measuring the mixing angle θ_{13}, which together with the previously measured θ_{23} mixing angle, determines how often a neutrino can switch to the other two kinds of neutrinos.

Neutrino telescopes as ANTARES [24] and IceCube [25] have been built to search for high energy cosmic neutrinos.

Experiments searching for neutrino cross sections and oscillations will release new measurements in the near future. From the long baseline oscillation searches of T2K and MINOS, to the short baseline and cross section measurements of MiniBooNE [26], MINERνA [27] and of course SciBooNE.

1.3 Neutrino interactions

In order to calculate the neutrino cross section for a given interaction in the simplified case of a low energy interaction (far away from the propagator mass) and small neutrino mass, either a differential cross section or a double differential cross section may be used. We can see in Eq: 1.3.1 a differential cross section with respect to the transferred momentum $q^2 = (p_\nu - p_l)^2$:

$$\frac{d\sigma}{dq^2} = \frac{1}{16\pi}\frac{|\mathcal{M}|^2}{(s - m_l^2)^2} \tag{1.3.1}$$

being $s = (p_\nu + p_q)^2$ the quadratic sum of the 4-momenta p_ν and p_q of the colliding particles in the center-of-mass frame, which is the center of mass

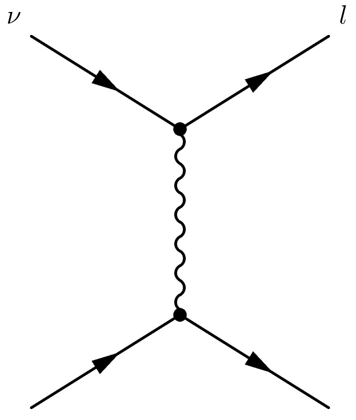

Figure 1.3.1: *Feynman diagram for Quasi-Elastic scattering.*

energy, and m_l the mass of the outgoing lepton. This differential cross section will be integrated in order to find the neutrino cross section.

Depending on the particular process that is being considered, the variables that should be integrated from the differential cross sections are carefully chosen as it is in the case of the Deep Inelastic Scattering (DIS), where transferred momentum and energy to the interacting quark are used. The more interesting part of the differential cross section is its dependence with the matrix element $|\mathcal{M}|^2$, where all the information of the particular interaction is contained.

The cross section calculation for the neutrino interactions is then reduced to the calculation of the matrix element $\mathcal{M}$ and the integration of the differential cross section in terms of the chosen variable.

The matrix element $\mathcal{M}$ can be calculated using a graphical technique introduced by R. Feynman. Each graph, known as a Feynman diagram, represents a contribution to $\mathcal{M}$. There are simple rules to compute the contribution to $\mathcal{M}$ from a specific diagram. These Feynman rules can be derived from the weak interaction Lagrangian (Eq: 1.3.2).

Neutrino interactions with matter are described by the weak interaction Lagrangian. The charged current part of the Lagrangian consists in the weak charged current coupled to the gauge boson $W^{\pm}$ being g the coupling constant.

$$\mathcal{L}_{CC} = -\frac{g}{2\sqrt{2}}\{W_{\mu}^{\dagger}\,\mathcal{J}_{\mu}^{CC} + h.c.\} \tag{1.3.2}$$

Where the current is the sum of the leptonic and the hadronic current: $\mathcal{J}_{\mu}^{CC} = j_{\mu} + J_{\mu}$. The coupling constant g is related with the Fermi coupling constant (G_F) by the expression 1.3.3

$$\frac{G_F}{\sqrt{2}} = \frac{g^2}{8M_W^2} \tag{1.3.3}$$

Given that only left-handed neutrinos interact, the current is of the V - A form. The leptonic part of the current can be written as $j_\mu = \bar{\nu}_l \gamma^\mu (1-\gamma_5) l$ and the hadronic current can be written as: $J_\mu = q' \gamma^\mu (1-\gamma_5) V_{qq'} q$. Therefore:

$$\mathcal{L}_{CC} = -\frac{g}{2\sqrt{2}} \{ W_\mu^\dagger [q' \gamma^\mu (1-\gamma_5) q + \bar{\nu}_l \gamma^\mu (1-\gamma_5) l] + h.c. \} \tag{1.3.4}$$

In the case of the quasi-elastic interaction, the first order Feynman diagram is Figure 1.3.1 and then, the matrix element is given by Eq. 1.3.5.

$$-\imath \mathcal{M} = -\frac{G_F}{2} [q' \; \gamma^\mu (1-\gamma_5) \; q] \; [\bar{l} \; \gamma^\mu (1-\gamma_5) \; \nu] \tag{1.3.5}$$

The leptonic current of the matrix element can be calculated exactly. In general, the hadronic current of the matrix element is more complicated and model dependent due to nucleon structure and has different parameterizations for different final states.

Then, for the relevant interactions regarding the neutral pion production, which is the focus of this thesis, DIS and resonant single pion production, the Feynman diagrams will led to a more complicated matrix element.

In the case of DIS (Figure 1.3.2), the parameterization leads to the differential cross section described in equation 1.3.6 [28].

$$\frac{d^2\sigma}{dxdy} = \frac{G_F^2 M_N E_\nu}{\pi} \Big((1 - y + \frac{1}{2} y^2 + C_1) F_2(x, q^2) \pm y (1 - \frac{1}{2} y + C_2) \big[x F_3(x, q^2) \big] \Big) \tag{1.3.6}$$

where

$$C_1 = \frac{y M_\mu^2}{4 M_N E_\nu x} - \frac{x y M_N}{2 E_\nu} - \frac{M_\mu^2}{4 E_\nu^2} - \frac{M_\mu^2}{2 M_N E_\nu x} \tag{1.3.7}$$

$$C_2 = -\frac{M_\mu^2}{2 M_N E_\nu x} \tag{1.3.8}$$

and $F_2(x, q^2)$ and $xF_3(x, q^2)$ are the nucleon structure functions. The nucleon structure functions $F_2(x, q^2)$ and $xF_3(x, q^2)$ are function of the Bjorken

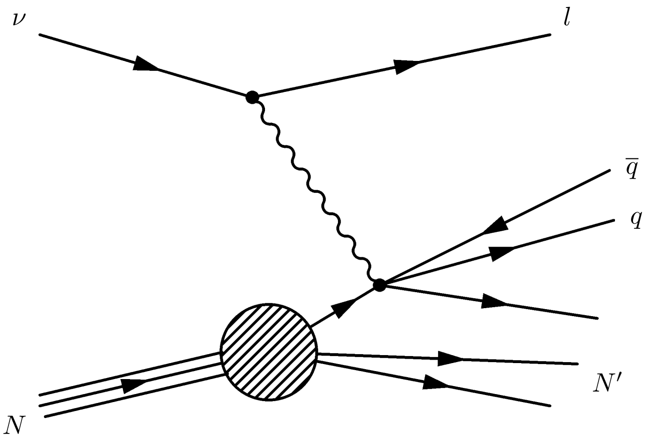

Figure 1.3.2: *Feynman diagram for Deep Inelastic Scattering.*

scaling variable $x = -q^2/2M_N(E_\nu - E_\mu)$ which is the fractional momentum carried by the struck quark. A linear dependence on q^2 is also taken into account in F_2 and F_3. $y = (E_\nu - E_\mu)/E_\nu$ is the fractional energy transferred to the hadronic vertex, M_N is the mass of the nucleon and M_μ the mass of the lepton.

The F_2 and xF_3 are measured using electron-nucleon and neutrino-nucleon scattering in the case of F_2 and neutrino-nucleon scattering only in the case of xF_3. Those measurements can be performed over free nucleons (using Deuterium) and over bound nucleons as inside C or Fe nuclei. The measurements must be corrected due to nuclear effects like nuclear shadowing and the ratios between measurements in different nuclei are tabulated as a function of the energy. The nucleon structure functions express the probability of finding a quark or a gluon inside the nucleon for a given momentum fraction x at a given momentum transfer q^2.

For the case of the resonant production (Fig. 1.3.3) the interaction is split in two steps.

$$\nu + \mathcal{N} \to l + \mathcal{N}^*, \ \ \mathcal{N}^* \to \pi + \mathcal{N}' \tag{1.3.9}$$

Where $\mathcal{N}$ and $\mathcal{N}'$ are nucleons and $\mathcal{N}^*$ is a hadronic resonance. The matrix element for the neutrino interaction step considering one single resonance is given by:

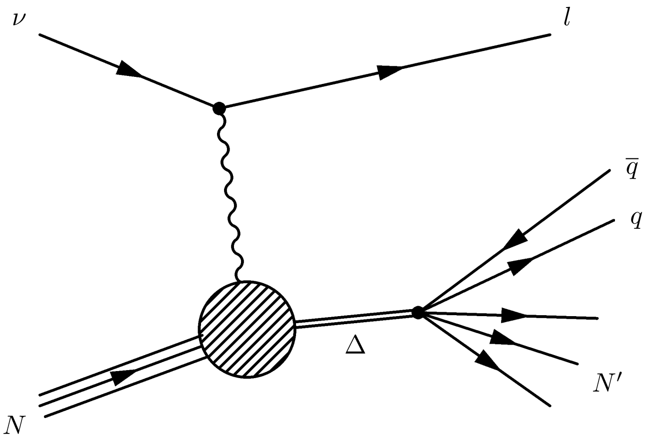

Figure 1.3.3: *Feynman diagram for resonant pion production.*

$$\mathcal{M}(\nu\mathcal{N} \to l\mathcal{N}^*) = \frac{G_F}{\sqrt{2}}[\bar{l}\gamma^\mu(1-\gamma_5)\nu] < \mathcal{N}^* \, |J_\mu(0)| \mathcal{N} > \tag{1.3.10}$$

Where the hadronic current J_μ is also of the V - A form. In order to build a more complete model, resonance interferences together with the decay fraction that leads to the considered final state must be included in the hadronic transition amplitude.

Following Rein and Sehgal's method [29], the final state is treated as a superposition of resonances where the resonances with same spin and orbital angular momentum are allowed to interfere.

The fractional amplitude for a given final state is the sum of each single resonance amplitude leading to the particular final state in the form of Eq: 1.3.11.

$$\mathcal{A}^{CC}(p\pi) = \sqrt{\frac{1}{3}}\sum a^{CC}(\mathcal{N}_3^*) + \sqrt{\frac{2}{3}}\sum a^{CC}(\mathcal{N}_1^*) \tag{1.3.11}$$

Where the resonance amplitudes a^{CC} (Eq. 1.3.12) consist of *production* (f^{CC}) and a *decay* (η^{CC}) factors, showing the two step in which the reaction is split. The subscripts 3 and 1 in Eq. 1.3.11 accounts for resonances of isospin $\frac{3}{2}$ or $\frac{1}{2}$ respectively.

$$a^{CC}(\mathcal{N}^*) = f^{CC}(\nu\mathcal{N} \to \mathcal{N}^*) \cdot \eta(\mathcal{N}^* \to \mathcal{N}\pi) \tag{1.3.12}$$

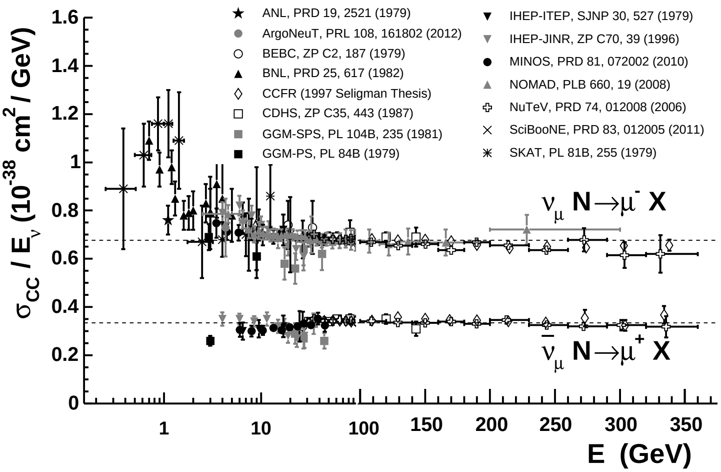

Figure 1.4.1: *Measurements of ν_μ and $\overline{\nu}_\mu$ CC inclusive scattering cross sections divided by neutrino energy as a function of neutrino energy. Note the transition between logarithmic and linear scales occurring at 100 GeV. Figure from [30].*

1.4 Current Status of ν Interaction Measurements

Current status of neutrino and antineutrino cross section measurements is shown in this section. Many experiments measured inclusive neutrino cross sections and also particular channels of interactions such as Quasi-Elastic (QE) or resonant pion production.

Neutrino cross section is proportional to energy at high energies where Deep Inelastic Scattering is dominant. The neutrino cross section over neutrino energy in terms of the neutrino energy is flat for high energies as can be seen in the Figure 1.4.1 where the inclusive charged current cross section measurements for muon neutrinos is shown.

Given that neutrinos have more interaction modes with matter than antineutrinos, neutrino cross section is higher by a factor of 2 or 3 than antineutrino depending on the energy range.

While at high energies the interaction process that dominates the cross section is the Deep Inelastic Scattering, at lower energies, different processes

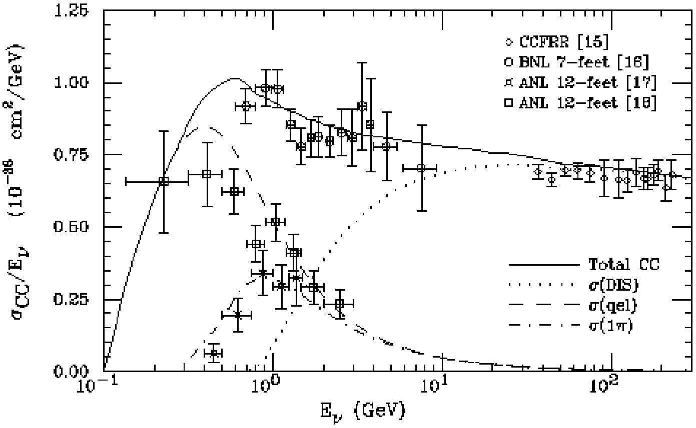

Figure 1.4.2: *σ/E_ν in terms of neutrino energy for different processes that contributes to the total CC neutrino cross section.*

contribute.

The dominant process at low energies (below 1 GeV) is quasi-elastic scattering. At slightly higher energies, single pion production starts to contribute and from a few GeV is the DIS the dominant process.

In Figure 1.4.2 the contributions to the total charged current cross section and thresholds of different processes can be seen.

Quasi-Elastic scattering cross section in terms of the neutrino energy can be seen in Fig: 1.4.3. Notice the asymptotic behavior of the QE cross section for neutrino energies greater than few GeV. Such behavior also applies to the anti-neutrino cross section.

In the case of the single pion production, cross sections can be found in Fig. 1.4.4 for both charged pion and neutral pion. The single pion production cross section rises rapidly once the pion production threshold is reached.

The measurements shown have different signal definitions and experimental conditions. Some of them, the first ones, typically used light targets as Hydrogen or Deuterium and measured specific final states. Most of the new measurements use nuclear targets like Carbon and Oxygen and adopt a more inclusive signal definition. This fact explains why the comparison between measurements has to be handled with care.

Given the topic of this thesis, it is interesting to report the recent results

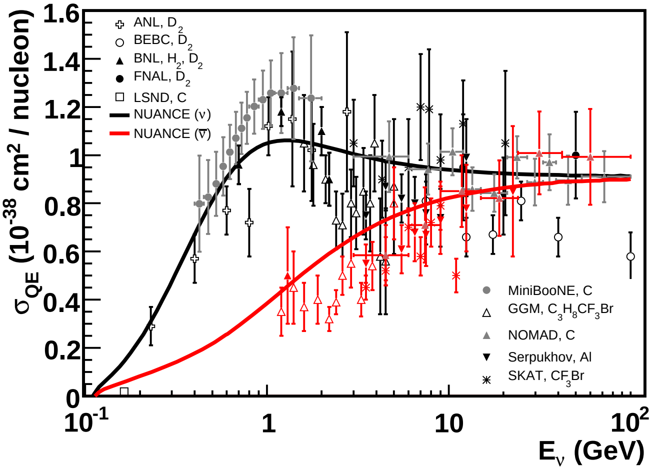

Figure 1.4.3: *Measurements of ν_μ (black) and $\overline{\nu}_\mu$ (red) quasi-elastic scattering cross sections (per nucleon) as a function of neutrino energy. Data on a variety of nuclear targets are shown. Also shown is the QE free nucleon scattering prediction [31] assuming MA = 1.0 GeV. This prediction is significantly altered by nuclear corrections in the case of neutrino-nucleus scattering. Figure from [30]*

on the Charged Current neutral pion production from MiniBooNE. The cross section measured by MiniBooNE is shown in 1.4.5. This measurement is of special interest because the signal definition, neutrino beam and target nucleus are the same as in SciBooNE. In this case, the neutral pion production is quantified in terms of pions leaving the target nucleus rather than for a specific pi+N final state as identified at the neutrino interaction vertex.

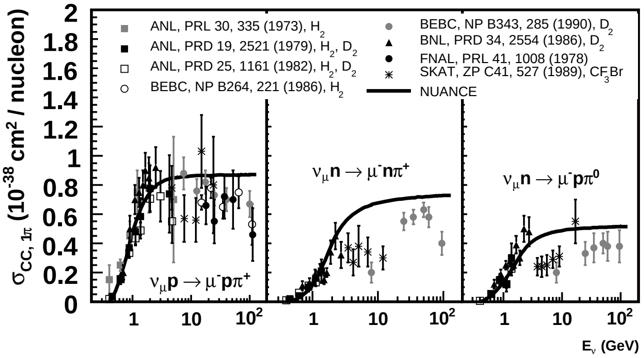

Figure 1.4.4: *Historical measurements of ν_μ CC resonant single pion production. The data appear as reported by the experiments; no additional corrections have been applied to account for differing nuclear targets or invariant mass ranges. The free scattering prediction is from [31] with MA = 1.1 GeV. Figure from [30].*

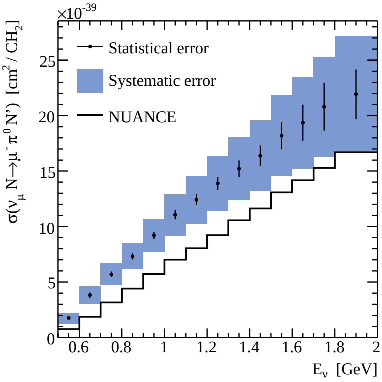

Figure 1.4.5: *The total observable charged current neutral pion production cross section as a function of neutrino energy as measured by MiniBooNE (black dots with blue systematic error band). The superimposed black histogram shows the prediction from the NUANCE generator [31] with MA = 1.1 GeV. Figure from [32].*

Chapter 2

The SciBooNE Experiment

The SciBar Booster Neutrino Experiment (SciBooNE) [33] is a neutrino scattering experiment located at Fermilab. Its goal is to accurately measure the total neutrino and anti-neutrino cross-sections around 1 GeV taking advantage of the fully active and fine grained SciBar detector from K2K, Japan, and of the well understood Booster Neutrino Beam (BNB) from Fermilab, USA.

SciBooNE is composed by three detectors: the SciBar detector [34], which is a fine grained tracking detector serving as neutrino interaction target, an electromagnetic calorimeter called Electron Catcher (EC) [35] located downstream of SciBar, and a Muon Range Detector (MRD) located downstream of EC. For SciBooNE, the detectors have been installed on the neutrino beamline axis, at 100 m distance from the beryllium production target, 7 m below surface level. A chart of the SciBooNE beamline is shown in Figure 2.0.1.

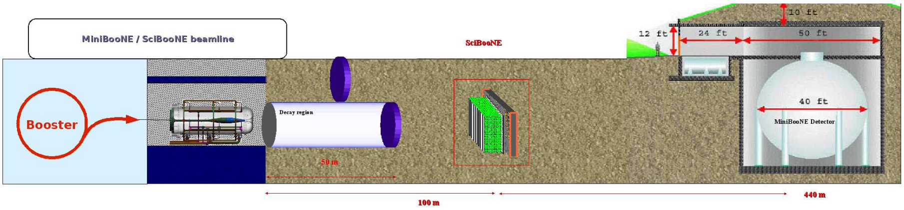

Figure 2.0.1: *SciBooNE/MiniBooNE Beamline.*

SciBooNE was first proposed in January 2006, just one year after the termination of K2K beam operations. The proposal was to develop a short term experiment where the main goal is to accurately measure the ν and $\overline{\nu}$ cross sections at low energies. In particular, SciBooNE is able to measure processes that represent the signal and primary background channels for the T2K experiment [36] . Those background channels are Charged-Current 1 π^+ ($\nu_\mu + N \to \mu^- + N + \pi^+$ or $\nu_\mu + A \to \mu^- + A + \pi^+$), for the ν_μ disappearance, which happens when in the reconstruction the π^+ is missed and the event looks like a CC-Quasi-Elastic event ($\nu_\mu + n \to \mu^- + p$), and the NC-1$\pi^0$ channel ($\nu_\mu + N \to \nu_\mu + N + \pi^0$ or $\nu_\mu + A \to \nu_\mu + A + \pi^0$), that is a background for the ν_e appearance when in the reconstruction the π^0 looks like an electron produced shower. SciBooNE is able to measure CC-1π^+ and NC-1π^0 cross sections and the energy spectrum of the CC channel [37], [38], [39], as discussed below.

Another goal of SciBooNE experiment is to complement the measurements done by MiniBooNE [40]. Since both MiniBooNE and SciBooNE are placed on the Booster Neutrino Beam, SciBooNE will allow for a two detector (MiniBooNE + SciBooNE) measurement of ν_μ and $\overline{\nu}_\mu$ disappearance in the Booster Neutrino Beamline.

SciBooNE started data taking in antineutrino mode in June 2007, and switched to neutrino mode after $\sim 0.5 \cdot 10^{20}$ Protons On Target (POT). By April 2008 neutrino mode run was completed with $1.02 \cdot 10^{20}$ POT ($0.99 \cdot 10^{20}$ POT available for analysis). The second run in antineutrino mode finished on August 2008 with a total of $\sim 1.53 \cdot 10^{20}$ POT of antineutrino data available for analysis. SciBooNE was shut off on August 18 of 2008.

A description of the SciBooNE beam and detectors follow in Secs. 2.1 and 2.2-2.4, respectively. A summary of earlier SciBooNE results is given in Sec.2.5.

2.1 Booster Neutrino Beam

The Booster beamline provided neutrinos to MiniBooNE in 2002-2012 and has provided SciBooNE with $2.64 \cdot 10^{20}$ POT in one year of operation (see Fig. 2.1.1). This same beamline will soon serve the MicroBooNE experiment also [41].

The BooNE neutrino beam begins with an 8 GeV primary proton beam from the Fermilab Booster accelerator [42]. The beam arrives in 1.6 μs pulses, with typically five pulses per second. Within each pulse, the beam arrives in 84 bunches that are 19 ns apart (see Fig. 2.1.2). Protons from the primary beam strike a 71 cm long berillyum target, producing short lived hadrons with a typical transverse momentum of 0.3 GeV/c. The hadrons are focused by the magnetic field generated from a high-current-carrying device called "horn".

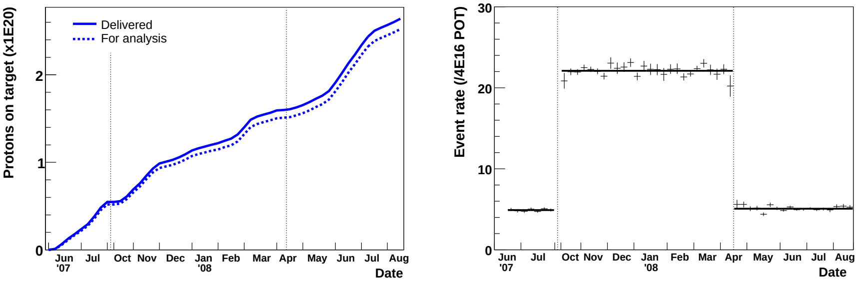

Figure 2.1.1: Left panel: *BNB delivered protons integrated in time. Solid line represents total POT while dashed means POT available for analysis after beam quality cuts.* Right panel: *Number of charged current candidate events in SciBar normalized to the number of protons on target. The event rate difference between neutrino and antineutrino modes can be seen clearly.*

The target is located within the magnetic focusing horn. A horn was chosen because it gives higher angular and momentum acceptances compared to other focusing systems. Also, a horn can be made to withstand high radiation levels, has cylindrical symmetry, and also gives sign selection. A horn (see Fig. 2.1.3) contains a pulsed toroidal magnetic field in the volume between two coaxial conductors. Current flows along the inner (small radius) conductor and back along the outer (large radius) conductor. There is no significant field inside the inner conductor, nor outside the outer conductor. In the volume between the inner and outer conductors, the magnitude of the field is given by B(kG) $\sim$ 0.2 $\cdot I(kA)/R(cm)$, and its direction is azimuthal (the field lines are toroidal, encircling the inner conductor). The inner conductor shape and current were optimized by using GEANT [43] to maximize the ν_μ flux between 0.5 - 1 GeV at the MiniBooNE detector while minimizing the flux above 1 GeV. The horn was designed to run at 170 kA for 10^8 pulses with $< 3\%$ fatigue failure probability. The first BNB horn pulsed 96 million times before failing due to corrosion, while the second horn is still operational and has been pulsed 397 million times as of 2013. Despite focusing, a highly divergent hadron beam exits the horn and enters the decay pipe. This beam consists mainly of unscattered and scattered primary protons and mesons. The decay pipe is 50 m long and 2 m in diameter; most pions and kaons decay before reaching its end. At the end of the decay pipe, 50 m from the target, a beam absorber

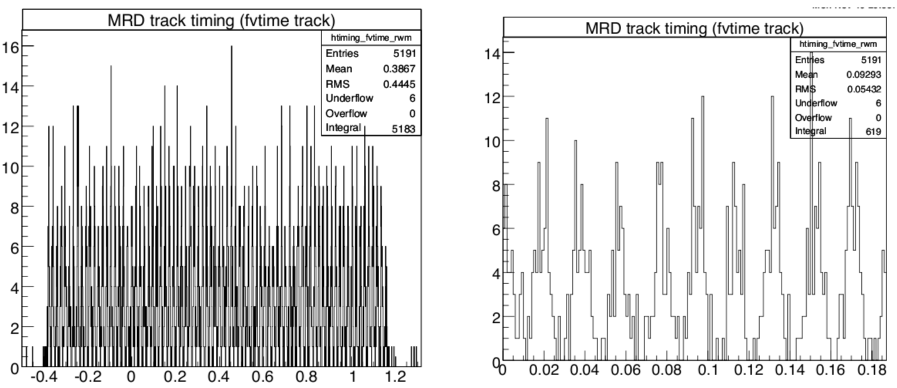

Figure 2.1.2: Left: *Booster batch structure with 84 bunches/batch spaced 18.9 ns apart measured by MRD using beam induced muon track times.* Right: *Detail of left plot. Times are in microseconds.*

which stops all the hadrons and low-energy muons is present. Located 25 m from the target is an intermediate absorber which can be lowered into the beam. This design feature was introduced to provide a systematic check on muon-decay ν_e background for the MiniBooNE ν_e appearance search.

2.2 The SciBar Detector

The SciBar detector [34] is a tracker detector acting also as neutrino target. In this analysis, SciBar is used for the detection of both the final state muon as well as of gammas from pi0 decay. It consists of 14848 extruded scintillator strips, each with dimension of $1.3 \times 2.5 \times 300$ cm^3. The scintillator strips are arranged in 64 layers. Each layer consists of two planes, with 116 strips glued together to give horizontal and vertical position. The total size and weight are $2.9 \times 2.9 \times 1.7$ m^3 and 15 tons, respectively. Each strip is read out by a wavelength shifting (WLS) fiber attached to a 64-channel Multi-Anode Photo-multiplier (MA-PMT). Charge and timing information from MA-PMT is recorded by custom designed electronics.

Figure 2.2.1 shows a schematic view of SciBar. Table 2.2.1 shows the design specifications for each component.

The scintillator strips are made of polystyrene, infused with PPO (1 %) and POPOP (0.03 %), and are produced by extrusion in the shape of rect-

Structure	Dimensions	$3\ m \times 3\ m \times 1.7\ m$
	Weight	15 tons
	Number of channels	14,336
Scintillator strip	Material	polystyrene, PPO(1%) and POPOP(0.03%)
	Size	$1.3\ cm \times 2.5\ cm \times 3\ m$
	Density	$1.021\ g/cm^3$
	Coating	0.25 mm (TiO_2)
	Emission length	420 nm (peak)
Fiber	Diameter	1.5 mmϕ
	Refractive index	1.56 (core), 1.49 (inner), 1.42 (outer)
	Absorption length	430 nm (peak)
	Emission length	476 nm (peak)
	Attenuation length	350 cm
PMT	Model	Hamamatsu H8804
	Cathode material	Bialkali (SB-K-Cs)
	Anode	8×8 pixels (2×2 mm^2/pixel)
	Wavelength sensitivity	300-650nm (Max 420nm)
	Number of dynode stages	12
	Gain(@800V)	3×10^5
	Quantum efficiency	12 % at $\lambda = 500$nm
	Dynode	Metal channel structure, 12 stages
	Gain	typical 6 × 105 at 800 V
	Response linearity	within 10% up to 200 p.e. with the gain of 6 × 105
	Crosstalk	3.15% $adjacentpixel$
DAQ	Shaping time	80 nsec (TA), 1.2μsec (VA)
	ADC Pedestal width	less than 0.3 p.e.
	ADC Linearity	within 5 % up to 300 p.e. with the gain of $5 \cdot 10^5$
	Number of TDC channels	448
	TDC resolution	0.78 nsec
	TDC full range	50 μsec

Table 2.2.1: *Specification of SciBar components.*

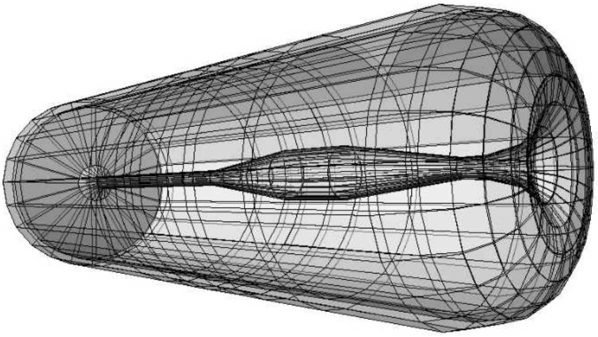

Figure 2.1.3: *The BooNE horn as simulated in the Geant4 beam Monte Carlo.*

angular bar with TiO_2 reflecting coating (0.25 mm thickness). Scintillators were produced at Fermi National Accelerator Laboratory (FNAL). Each scintillator has a 1.8 mm diameter hole where the 1.5 mmϕ WLS fiber is inserted for light collection. The fiber is multi-clad type, Y11(200)MS, made by Kuraray. The light attenuation length of all WLS fibers were measured before the installation. The average attenuation length is 350 cm.

The MA-PMT is H8804 made by Hamamatsu Photonics K.K. Its anodes are arranged in an 8 × 8 array with each anode measuring 2 mm × 2 mm of photocatode sensitive area. The sensitive wave length is from 300 nm to 650 nm, which matches the emission spectrum of the WLS fibers. The cross talk value between neighboring channels in our configuration is less than 4 % (see Fig. 4.1.4 in Section 4.1).

In order to separate protons from pions by the energy deposited per unit track length, a wide dynamic range is required for the readout system. The readout system consists of front-end electronics attached to MA-PMT and a back-end VME module. A combination of ASICs (VA32HDR11 and TA32CG made by IDEAS) is used for the front-end readout electronics. VA is a 32-ch preamplifier chip with shaper and multiplexer. TA provides timing information after taking the OR of 32 channels. Two packages of VA/TA are mounted on a custom-designed PCB board (Front-End board, FEB) to read out signals from 64 anodes. A back-end electronics board (DAQB) has been also newly developed for K2K as a standard VME-9U board. One DAQB controls and

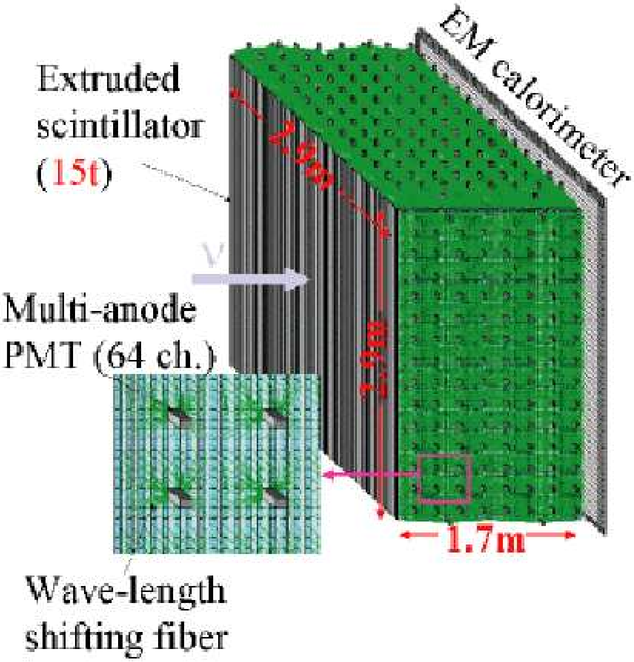

Figure 2.2.1: textitSchematic drawing of the SciBar detector.

reads out eight FEBs. The charge information from MA-PMTs is digitized with a 12-bit flash ADC and read out through VME bus. The gains of all channels have been measured before installation. The linearity is also measured to be 5% up to 300 photo-electrons (30 MeV) while the pedestal width is 2 ADC counts, corresponding to 0.03 MeV.The timing information is processed and recorded by a Time to Digital Converter (TDC). We use a 64-ch, multi-hit TDC developed for the ATLAS muon chambers.

Taking into account the structure of the beam bunches, 4 different detector triggers are set (see Fig. 2.2.2): The beam trigger that starts about 2 μs before the first beam bunch arrives and lasts for about 20 μs. We read all channels from all subdetectors (SciBar, EC, MRD) for every beam trigger, regardless of the hit occupancy, to ensure unbiased beam data. The LED trigger, to monitor dead channels and Photo-Multiplier Tube (PMT) gain variations, uses a LED shining when the beam window is closed. The subsequent pedestal trigger opens the window after the LED trigger to measure the pedestal levels. Pedestal level is the channel ADC value when no light reaches the PMT. Those ADC values are substracted from the signal in the calibration process. Finally, the cosmic ray trigger opens a window where cosmic ray events are stored. We have independent cosmic triggers for SciBar/EC and for MRD, both prescaled to collect 20 cosmic ray triggers per cycle.

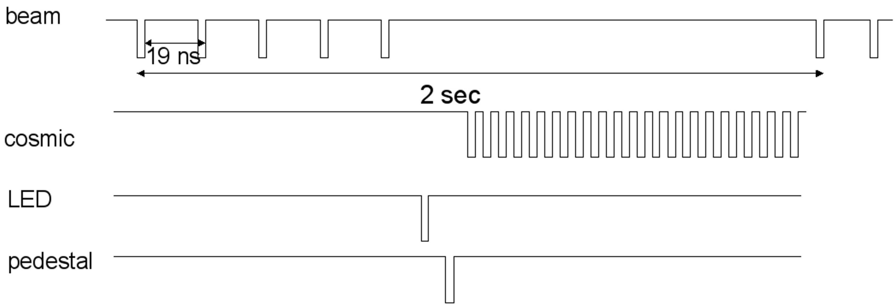

Figure 2.2.2: *SciBooNE trigger structure and timing.*

The hit finding efficiency in SciBar was found to be 99.9% and 99.8% for horizontal and vertical views, respectively. The procedure used to determine efficiency is as follows. The setup for the efficiency studies has a trigger for cosmic ray crossing the whole detector, so it is required to have a hit in the first and last layer in both views to have a clean track. Then, the n^{th} layer is masked and hits are required in the $n-1^{th}$ and $n+1^{th}$ planes and a linear fit is made over the track without taking in account the masked plane. Once the fit is done, the plane is unmasked and we look if there is a hit in the expected position. The hit finding efficiency is defined by Equation 2.2.1.

$$hit\ finding\ eff. = \frac{\#evts\ with\ hit\ on\ the\ n^{th}\ plane}{\#evts\ with\ hits\ on\ the\ n-1^{th}\ and\ n+1^{th}\ planes} \tag{2.2.1}$$

With this analysis, three planes with a dead channel in them where found. Nevertheless, hit finding efficiency is over 99% for all planes. Inefficiency in SciBar comes mainly from the TiO_2 coating, that introduces dead material between the scintillators, and cannot be reduced.

2.3 The Electron Catcher

The Electron Catcher (EC) [35], also recycled from K2K, is located downstream of the SciBar tracker. It is an electromagnetic calorimeter and it is used to measure the neutrino interactions where π^0's are produced. This is because the EC can distinguish electron or photon tracks from muon or pion tracks, in addition to accurately measuring the track energy. As we will see, the EC is used in this analysis for the detection of gammas from pi0 decay.

The EC is composed by a horizontal and a vertical plane with 32 modules each.The modules are made of lead and scintillator fibers . It is placed at a 15 cm distance from the downstream end of SciBar, measuring (“catching”) the part of electron or photon energy that may not have been deposited entirely in SciBar.

The EC was originally part of the calorimeter of the CHORUS experiment [35]. The EC has then been adapted to the SciBar dimensions, with planes that are $270 \times 270\ cm^2$ wide.

The two planes of the EC correspond to 11 radiation lengths (11 X_0), enough to absorb photons and electrons below 2 GeV with 90% energy containment. These dimensions are sufficient, given the Booster neutrino beam energy.

The EC optimal energy resolution attained in the CHORUS setup is given by:

$$\frac{\sigma(E)}{E} = \frac{(13.8 \pm 0.9)\%}{\sqrt(E)} + (-0.2 \pm 0.4)\% \quad for \quad electrons \tag{2.3.1}$$

for electrons and

$$\frac{\sigma(E)}{E} = \frac{(32.3 \pm 2.4)\%}{\sqrt(E)} + (1.4 \pm 0.7)\% \tag{2.3.2}$$

for charged pions, where E is in GeV.

Furthermore, the EC energy response has been measured to be linear, within 10% accuracy, over the energy range 50 MeV - 3 GeV.

The modules (bars) of the EC are made of scintillating fibers immersed in a lead field [1]. A module is obtained by superimposing 20 lead sheets, 2620 mm long, 82.4 mm wide, and 2 mm thick, each. In addition to the lead sheets, each module contains 740 fibres which are 3050 mm long and 1 mm in diameter. The module is wrapped in a 2 mm wide aluminium sheet. The section of a module is shown in Figure 2.3.1. At the end of a module, the fibres are coupled to two Hamamatsu R1355/SM Photo-Multiplier Tubes, in such a way that one single module is read by four Photo-Multiplier Tubes, two at each end.

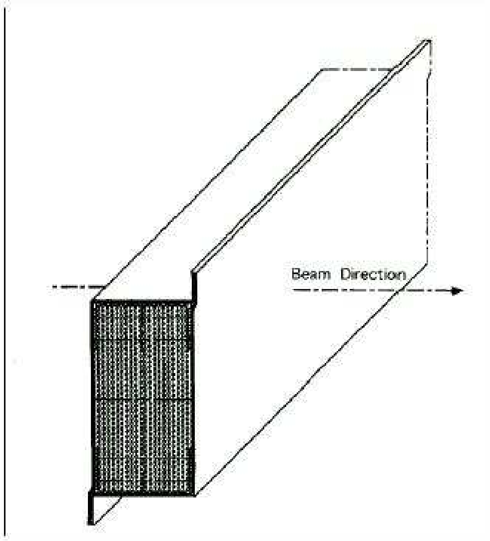

Figure 2.3.1: *Transversal section of a module of the Electron Catcher*

---

[1] This is the reason why this kind of calorimeter is called a “spaghetti calorimeter”.

EC plane	Dimensions	270 cm × 270 cm × 4.2 cm
	Radiation Length	5.5 X_O
	Number of modules	32
EC module	Dimensions	270 cm × 8.4 cm × 4.2 cm
	Material composition	21 lead sheets 740 fibers (Kuraray SCSF81)
	Fiber emission spectrum	420 nm (peak)
	Fiber attenuation length	4 m (average)
PMT	Model	Hamamatsu R1355/SM
	Wavelength sensitivity	300-650 nm
	Peak QE	27% at 350-450 nm
	Gain	$2.1 \cdot 10^6 at 1.6$ kV
Readout electronics	Number of ADC channels	256
	Model	CAEN V792
	ADC pedestal width	0.7 PEs
	ADC response linearity	within 2% up to 600 PEs

Table 2.3.1: *Specification of the EC components.*

In its propagation through the fiber, the light suffers an exponential attenuation with an attenuation length λ of about 3 m, until it reaches the Photo-Multiplier Tubes, where it is converted into a photoelectron pulse.

In order to eliminate the signal amplitude dependence on the hit position caused by light attenuation, the signals at the right (R) and left (L) ends of each module are combined in the following geometric average in the EC clustering algorithm:

$$S = \sqrt{S_R \times S_L} = \sqrt{(Ae^{-\frac{x}{\lambda}}) \times (Ae^{-\frac{L-x}{\lambda}})} = Ae^{-\frac{L}{2\lambda}} \tag{2.3.3}$$

where x is de distance between the light production point and the PMT on the right side, and L is the total module length.

The 256 PMT charges are read out by ADC modules (CAEN V792, 32 channels per module), while no timing information is available for the EC.

2.4 MRD Detector

The Muon Range Detector consists of 12 iron plates 5 cm thick sandwiched between 13 scintillator planes, with alternating horizontal and vertical orientations, starting and finishing with horizontal ones. The 60 cm of total iron thickness gives to the MRD the capability to stop muons with energy up to

1 GeV with an energy resolution around 100 MeV. As for all SciBooNE CC analyses, we use the MRD in this thesis to tag muons.

The MRD was built at FNAL recycling almost all the components from old experiments. The dimensions of the iron plates are $274 \times 305 \times 5$ cm^3 and cover the forward exiting particles (mostly μ). The modules are composed by a scintillator counter glued to a light guide connected to a PMT (see Fig. 2.4.1 for schematics). There are 26 modules in the horizontal planes arranged in two columns of 13 modules each with the PMTs facing opposite sides and 30 modules on the vertical planes, arranged in the same way, two rows of 15 scintillators each with the PMTs facing opposite sides. The dimensions of the horizontal scintillators are 155 cm long, 20 cm high and 0.6 cm thick, for a total scintillator volume per horizontal plane of $310 \times 260 \times 0.6\ cm^3$. The dimensions of the vertical ones are $138 \times 20 \times 0.6$ cm^3, for a total scintillator volume per vertical plane of $276 \times 300 \times 0.6\ cm^3$.

Iron plate	Number of plates	12
	Dimensions	274 cm × 305 cm × 5 cm
	Density	7.841 g/cm^2
Scintillator plane	Number of planes	13
	Segmentation	2 × 15 (V), 13 × 2 (H)
	Counter dimensions	138 cm × 20 cm × 0.6 cm (V)
		155 cm × 20 cm × 0.6 cm (H)
PMT	Model (V)	Hamamatsu 2154-05, RCA 6342A
	(H)	EMI 9954KB, 9839b and 9939b
	Gain (V)	∼ 1 × 106 at 1200V
	(H)	∼ 1 × 107 at 2000V
Readout Electronics	Number of channels	362
	ADC model	LeCroy 4300B
	TDC model	LeCroy 3377
	TDC resolution	0.5 ns
	TDC full range	32 μs

Table 2.4.1: *Specification of the MRD components.*

Because PMTs are also recycled from different previous experiments, a good calibration is particulary important. Among the MRD PMTs there are tubes powered at both negative and positive high voltage values. Three main brands of PMTs are used in different proportions. For the vertical planes Hamamatsu 2154-05 and 5686, and RCA 6342A Photo-Multiplier Tubes are used. EMI 9954KB, 9839B and 9939B PMTs are used in the horizontal planes. EMI 9939B Photo-Multiplier Tubes use a positive high voltage, while all the other PMT uses negative HV. All PMTs operating at positive HV are placed in plane number 8, where the plane numbering scheme increases from upstream to downstream. Both PMT times and charges are recorded.

Efficiency performance studies of MRD have been performed and a good hit finding efficiency was found. For horizontal planes, a mean efficiency of 98% was found. Figure 2.4.2 shows the efficiency of each counter as a function of the cosmic track position for a typical plane.

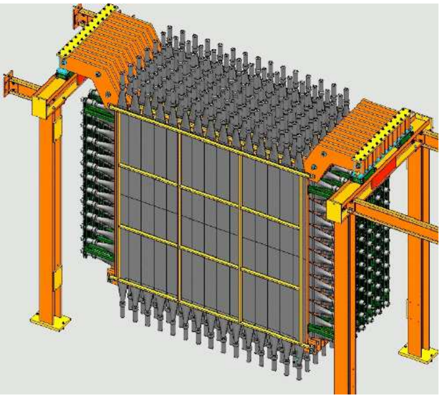

Figure 2.4.1: *Schematics of the MRD detector.*

2.5 Summary of earlier SciBooNE results

SciBooNE performed a search for charged current coherent pion production from muon neutrino scattering on carbon, with two distinct data samples [44]. No evidence for coherent pion production was observed, as was the case for the earlier search in K2K-SciBar [45]. Therefore, a 90% CL upper limit on the ratio of the charged current coherent pion to total charged current production cross sections of 0.67×10^{-2} (1.36×10^{-2}) was obtained at a mean neutrino energy of 1.1 GeV (2.2 GeV) using a sample of MRD stopping (MRD penetrating) muons. This result demonstrates that the Rein-Sehgal model for coherent pion production [46], experimentally tested in the high (several GeV) energy regime and predicting a higher cross section, breaks down in the few GeV energy region, as shown in Fig. 2.5.1. The SciBooNE result has triggered a renewed activity in the modelling of coherent pion production. As shown in

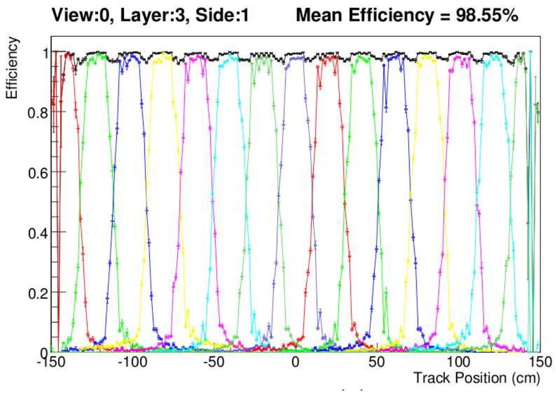

Figure 2.4.2: *Efficiency of a typical plane. Colored points shows the efficiency of each counter as a function of the track position. Black points shows the total efficiency.*

Fig. 2.5.1, several recent models predict a considerably smaller cross section, in agreement with the SciBooNE result. However, these models have not yet been validated against previous experimental results at higher energies.

SciBooNE improved pur understanding of π^0 production via neutrino-nucleus neutral current (NC) interactions. The cross section ratio of NC π^0 production to the total CC interaction has been measured to be $(7.7 \pm 0.5(\text{stat.}) \pm 0.5(\text{syst.})) \times 10^{-2}$ at a mean neutrino energy of 1.1 GeV [38]. This result agrees with the Rein-Sehgal model for resonant pion production [51], which is the model generally used by Monte Carlo event generators. Also, SciBooNE achieved less than 10% uncertainty on this measurement, as required by the current-generation neutrino oscillation experiment T2K for an adequate understanding of the backgrounds to $\nu_\mu \rightarrow \nu_e$ oscillations [52]. The shape of the π^0 momentum and angle distributions also agree with predictions (see Fig. 2.5.2), implying that not only the Rein-Sehgal model but also the intra-nuclear interaction models describe our data well. Also, from this inclusive neutral current π^0 sample, SciBooNE was also able to isolate a neutral current coherent pion production subsample. The cross section ratio of NC coherent pion production to the total CC interaction was measured to be $(1.16 \pm 0.24) \times 10^{-2}$ at a mean neutrino energy of 0.8 GeV [39]. Unlike its charged current counterpart, the neutral current mode of coherent pion production appears in agreement with expectations from the Rein-Sehgal coherent

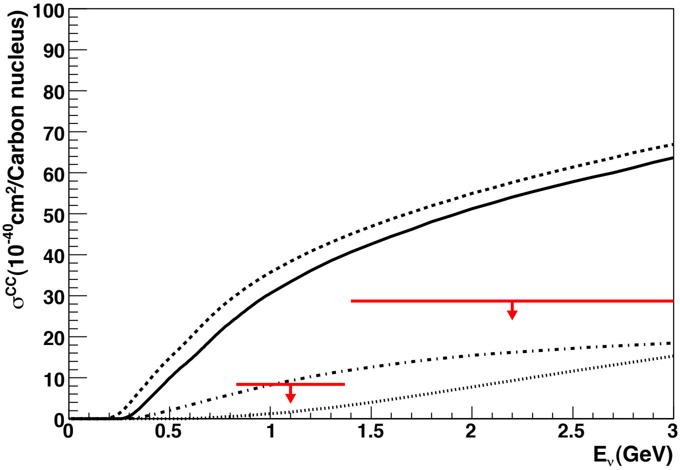

Figure 2.5.1: *Comparison of SciBooNE results on CC coherent pion production with theoretical predictions. The red lines with arrows indicate SciBooNE 90% CL upper limits. The limits are obtained from SciBooNE 90% CL upper limits on the ratio of charged current coherent pion production to total charged current cross sections [44] and total charged current cross section predicted by the NEUT simulation [47]. The Rein and Sehgal model with lepton mass effects (solid line, [48]), the Rein and Sehgal model without lepton mass effects (dashed, [46]), the model of Kartavtsev et al. (dotted, [49]), and the model of Alvarez-Ruso et al. (dashed-dotted, [50]) are shown.*

pion model [46].

SciBooNE extracted energy-dependent inclusive CC interaction rates and cross sections for a wide energy range from 0.25 GeV to 3 GeV [53]. The interaction rates (cross sections) were measured with with 6-15% (10-30%) precision, see Fig. 2.5.3. SciBooNE also made energy integrated measurements, with a precision of 3% for the rate, and 8% for the cross section measurement. This is the first measurement of the CC inclusive cross section on carbon around 1 GeV. This inclusive interaction measurement is nearly free from effects of hadron re-interactions in the nucleus. Hence, it is complementary to other exclusive cross section measurements as the ones described above. Also, this analysis provides the normalization for the above-mentioned SciBooNE cross section ratio measurements for charged current coherent pion production and neutral current neutral pion production.

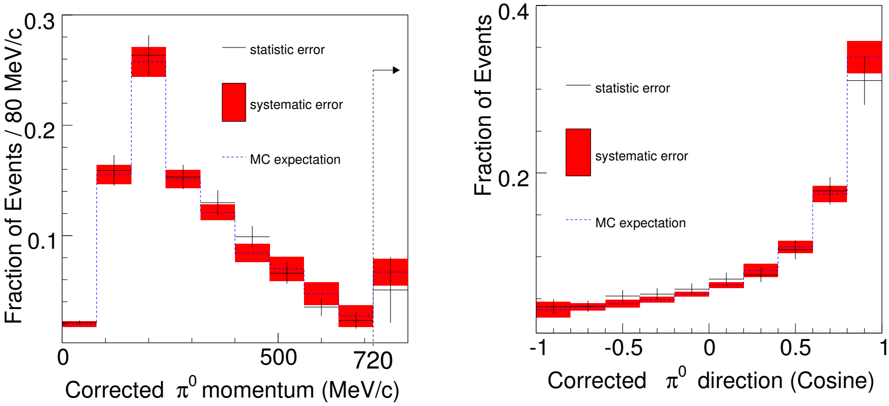

Figure 2.5.2: *The π^0 momentum (left panel) and angle (right panel) distributions measured by SciBooNE [38], with statistical (error bars) and systematic (red boxes) uncertainties. The dashed line shows the Monte Carlo expectation based on the Rein-Sehgal model for resonant pion production [51].*

SciBooNE also measured the absolute charged current quasi-elastic (CC-QE) interaction cross section as a function of neutrino energy [54, 55]. The cross section per proton on a carbon target is shown in Fig. 2.5.4. The measured cross section is consistent with the MiniBooNE result [56] and the NEUT prediction with M_A =1.2 GeV/c^2 [47], but higher than expected from the NOMAD result [57].

Apart from neutrino interaction studies, SciBooNE performed neutrino oscillation searches. The SciBooNE Collaboration joined efforts with the MiniBooNE Collaboration to perform two-detector (and hence dual-baseline) searches for muon neutrino and muon antineutrino disappearance in the BNB [58, 59]. These searches are motivated by the possible existence of light sterile neutrinos in the ∼1 eV mass range, as hinted by several anomalous results [60]. These joint analyses found no indications for either neutrino nor antineutrino oscillations in the muon disappearance channel. In the simplest two-neutrino oscillation model, the upper limits on the neutrino mixing angle $\vartheta_{\mu\mu}$ as a function of the mass splitting Δm^2 are shown in Fig. 2.5.5 for both the neutrino and antineutrino mode searches.

Finally, SciBooNE improved our understanding of the neutrino fluxes produced by the Booster Neutrino Beam, as well as of the underlying hadron

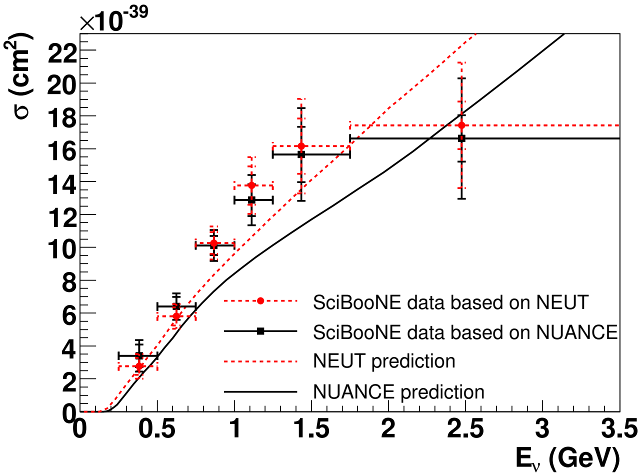

Figure 2.5.3: *Charged Current inclusive interaction cross section per nucleon on a polystyrene target (C_8H_8) measured by SciBooNE [53]. The smaller error bars show the uncertainties of the rate normalization factors, and the larger error bars represents the total error including the flux uncertainties.*

production in the proton interactions with the BNB beryllium target. In particular, using high-energy neutrino and antineutrino interactions in SciBooNE, the double-differential K^+ production cross section was measured to be $d^2\sigma/dpd\Omega = (5.34 \pm 0.76)$ mb/(GeV/c× sr) for p+Be→ K^++X at a mean K^+ energy and angle of 3.9 GeV and 3.7 degrees, respectively [61]. Compared to Monte Carlo predictions using previous higher energy K^+ production measurements, this result is consistent with a normalization factor of 0.85±0.12. This agreement is evidence that the extrapolation of the higher energy K^+ measurements to an 8 GeV beam energy using Feynman scaling [62] is valid. This measurement reduces the error on the K^+ production cross section from 40% to 14%.

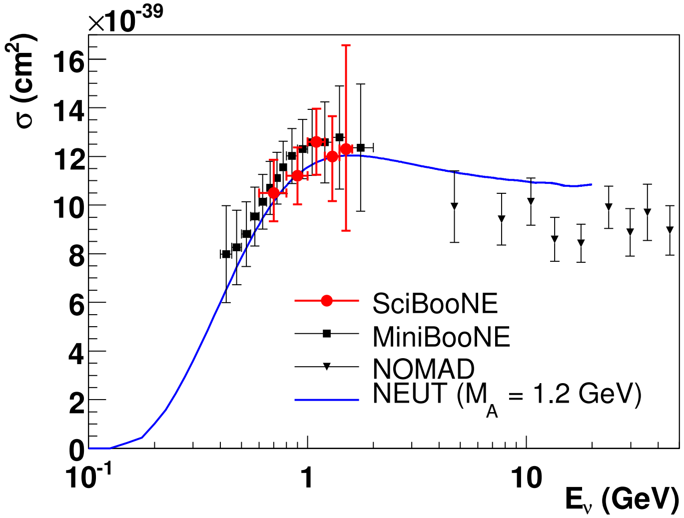

Figure 2.5.4: *CCQE cross section per proton measured in SciBooNE [54, 55]. The prediction of NEUT is shown as a solid curve. The results from MiniBooNE [56] and NOMAD [57] are also shown.*

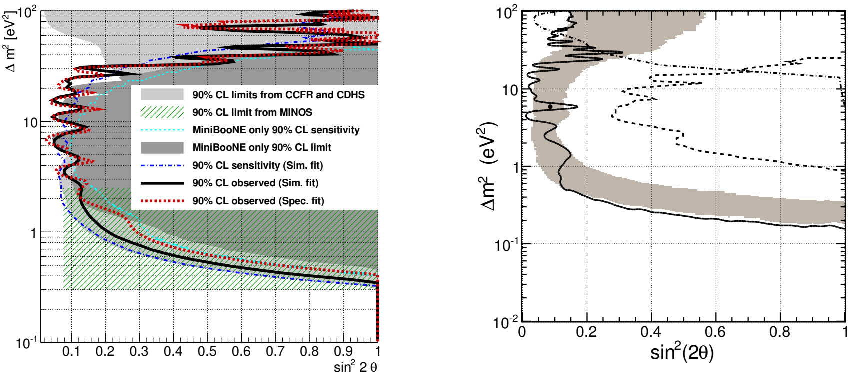

Figure 2.5.5: Left panel: *90% CL exclusion region for the simultaneous fit method (solid black curve) and for the spectrum fit method (red dashed curve) for the joint MiniBooNE, SciBooNE* ν_μ *analysis [58]. The sensitivity for the simultaneous fit analysis is also shown (dot-dash curve) with previous limits by CCFR and CDHS (light gray), MiniBooNE (dark gray) and MINOS (green hash box). The sensitivity for the MiniBooNE-only analysis is also shown (cyan dashed curve).* Right panel: *90% CL exclusion region (solid line) and best-fit point for the joint MiniBooNE, SciBooNE* $\bar{\nu}_\mu$ *analysis [59]. Also shown is the 90% CL result from the 2009 MiniBooNE disappearance analysis (dashed line) and the CCFR experiment (dot-dashed line). The expected 90% CL sensitivity band from fake data studies is also shown (shaded region); 1*σ *(68%) of fake data tests, where the fake data had statistical and systematic fluctuations but no oscillation signal, had 90% CL limit curves in this shaded region.*

Chapter 3

Monte Carlo Simulations

The Monte-Carlo simulation for SciBooNE is composed by three independent simulations. Each one is used as an input to the next simulation.

- GEANT4 [63] is used for the neutrino beam simulation. This simulation is developed in five steps from the generation of the primary protons upstream of the target to the decay processes of the produced particles that result in neutrinos.
- NEUT [47] is used to generate neutrino interactions inside SciBar, EC and MRD detectors and in the dirt surrounding the detectors. Charged current quasi-elastic, neutral current elastic, single π, η, K resonance productions, coherent pion productions and deep inelastic interactions are simulated.
- GEANT4 is used again to simulate the detector geometry and response taking into account all materials and electronics of each detector to simulate the passage of the final state particles exiting the target nucleus into the detector, and energy deposition.

In the next three sections, a more detailed explanation is given.

3.1 Booster Neutrino Beam simulation

The Booster Neutrino Beamline is simulated using GEANT4 [42]. The geometry of the simulation consists of:

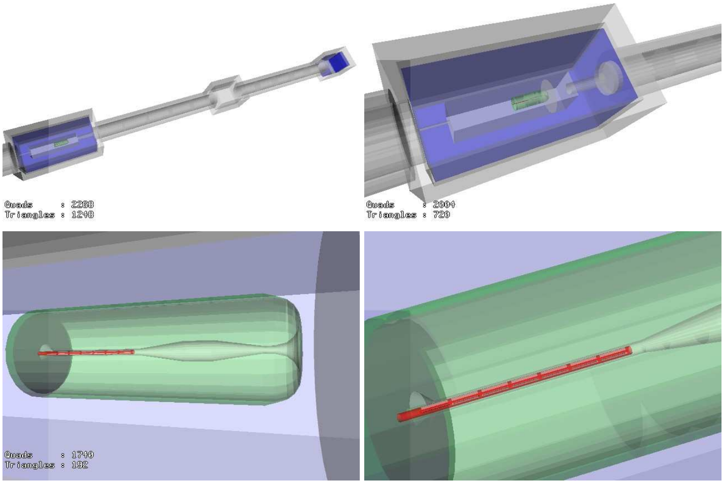

Figure 3.1.1: *The Booster Neutrino Beamline geometry as defined in the GEANT4 Monte Carlo. The images show the full 50 m decay region (top left), the target hall (top right), the horn (bottom left) and the beryllium target (bottom right).*

- The last portion of the Booster neutrino beamline, where the protons are accelerated up to 8 GeV.
- The target hall including the Beryllium target itself, the Aluminum magnetic horn and a collimator system made of concrete.
- The 50 m long decay region placed downstream the target to allow the charged pions decay to muons and neutrinos.

The target hall is simulated with concrete walls. In the interior, the target is placed together with the focusing horn. The Beryllium target is 71.1 cm long and has a 0.51 cm radius. The magnetic horn is made of Aluminum with air filling the space between the inner and the outer conductor. The magnetic field generated by the 174 kA of current passing through the magnetic horn is simulated with its corresponding 1/R geometry. The penetration of the magnetic field inside the conductor leading to the “skin effect” is also simulated.

The decay region is simulated as two pipes 20 m long and 1.8 m diameter, separated by the 10 m long 25 m absorber enclosure. The walls of the pipes are made of concrete and the whole structure is surrounded by dolomite. At the end of the pipe the beam stop absorber is located.

The protons from the beam are simulated individually 1 cm upstream of the target matching the measured beam profile, position and direction. The proton beam properties are measured by the beam monitors located right upstream from the target. The primary p-Be interactions are simulated using customized cross section tables in order to calculate the proton mean free path inside the target. The final state composition and the interaction kinematics for the interactions of protons with momentum between 8.8 GeV and 8.9 GeV with Be are also calculated using customized double differential cross section tables. From those interactions, seven secondary particles are produced: $\pi^{\pm}$, $K^{\pm}$, K^0_L, n, and p. The cross section tables for $\pi^{\pm}$ production are based on HARP [64] data.

For the secondary p-Be, n-Be and $\pi^{\pm}$-Be interactions, and also for the interactions with Aluminum nuclei, the mean free path is calculated using customized cross section tables, while the final state composition and kinematics of the interaction are managed by the default GEANT4 models.

The propagation of the particles through the 1/R magnetic field produced by the focusing horn, including the skin effect, the energy loss of the particles and the possible re-interactions of the particles with materials other than Be and Al are managed by GEANT4 models.

In the decay region, the neutrino beam is produced by the decay of the pions and kaons that come from the primary p-Be interactions and the muons produced by the pion and kaon decays. While the decaying point is determined by GEANT4, the kinematics of the decay are determined by a custom decay model to properly take into account polarization effects and decay form factors. The branching ratios, decay modes and lifetime of the neutrino parent particles are shown in table 3.1.1. Finally, to enhance the Monte-Carlo (MC) statistics, every decay is repeated 10 times. It is at this point, while introducing random kinematic variations every time, where correct kinematics are accounted for.

Figures 3.1.2 and 3.1.3 show neutrino flux predictions at the SciBooNE detector location for neutrino and antineutrino running modes, respectively. The expected flavour composition in neutrino running mode is 93.0% of ν_μ, 6.5% of $\overline{\nu_\mu}$, 0.6% in ν_e and $\overline{\nu}_e$, with flux-averaged energy of 0.72 GeV.

3.2 Simulation of neutrino interactions

Neutrino interactions are simulated using the NEUT neutrino event generator [47]. NEUT implements neutrino interactions above ~100 MeV. Simulated

Particle	Lifetime (ns)	Decay mode	Branching ratio (%)
π^+	26.03	$\mu^+ + \nu_\mu$	99.9877
		$e^+ + \nu_e$	0.0123
K^+	12.385	$\mu^+ + \nu_\mu$	63.44
		$\pi^0 + e^+ + \nu_e$	4.98
		$\pi^0 + \mu^+ + \nu_\mu$	3.32
K_L^0	51.6	$\pi^- + e^+ + \nu_e$	20.333
		$\pi^+ + e^- + \overline{\nu}_e$	20.197
		$\pi^- + \mu^+ + \nu_\mu$	13.551
		$\pi^+ + \mu^- + \overline{\nu}_\mu$	13.469
μ^+	2197.03	$e^+ + \nu_e + \overline{\nu}_\mu$	100.0

Table 3.1.1: *Particle lifetimes and neutrino-producing decay modes and branching ratios considered in the simulation.*

CC quasi-elastic scattering	$\nu_l + n \to l^- + p$
NC elastic scattering	$\nu_l + N \to \nu_l + N$
CC/NC single π, η, K resonant	$\nu_l + N \to l/\nu_l + N' + \pi(\eta, K)$
CC/NC coherent pion production	$\nu_l + X \to l/\nu_l + X' + \pi$
CC/NC deep inelastic scattering	$\nu_l + N \to l/\nu_l + N' + multi - \pi(\eta, K)$

Table 3.2.1: *Neutrino interactions generated by NEUT. In the table, l accounts for lepton, N/N' for nucleon and X/X' for nucleus.*

neutrino interactions can be found in Table 3.2.1. In this section the way the neutrino events are simulated will be described.

The neutrino energy distribution of interactions expected in the SciBooNE detector is given by the convolution of the neutrino flux (Figures 3.1.2 and 3.1.3) with the total cross-section (Figure 3.1.4). Once the flavour, energy and interaction location in the detector for the neutrino participating in the interaction are fixed, and using the known cross-section for individual interactions, an interaction mode is selected between the ones listed on Table 3.2.1 and one event is simulated.

The primary interaction simulation is done in three steps. First one is to fix the number of particles in the final state according to the selected interaction type. The second step consists in fixing and storing the type and momentum of each final state particle. Then, if applicable, nuclear effects and secondary interactions inside the nucleus are also simulated modifying the final state

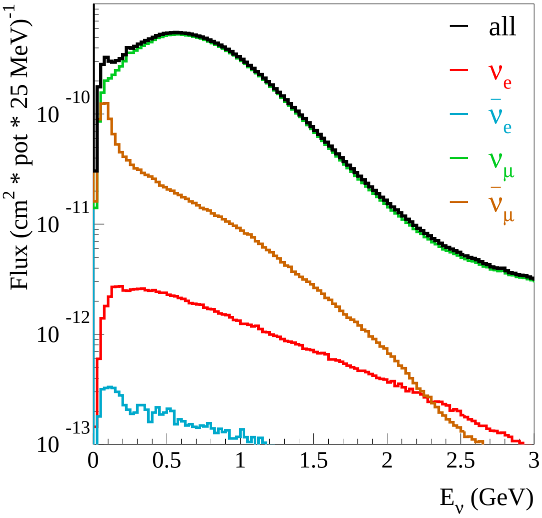

Figure 3.1.2: *Neutrino flavour spectrum in neutrino beam mode.*

particles and properties.

The following interaction types are simulated[1]:

- Quasi-elastic scattering simulation is based in C.H. Llewellyn Smith formalism [65] assuming dipole form factor for $F_A(Q^2)$ and $F_V(Q^2)$. The only free parameter of this model is M_A which is set to 1.1 GeV/c^2. For the bound nucleons, a relativistic Fermi-gas model is used from Smith and Moniz calculations, with a Fermi momentum of 217 (250) MeV/c for carbon (iron) target.

- Resonant single meson production implementation is based on Rein and Sehgal model [29] (see Section 1.3), with resonant axial mass value of $M_{A,1\pi}$ = 1.1 GeV. All resonances up to 2 GeV mass are taken into account. However $\Delta^+(1232)$, $\Delta^{++}(1232)$ are the resonances more largely produced in SciBooNE beam energies.

---

[1] Among the simulated interaction types, single pion production and DIS are the main contributions to neutral pion production. For this reason, a more detailed explanation of such interactions is given.

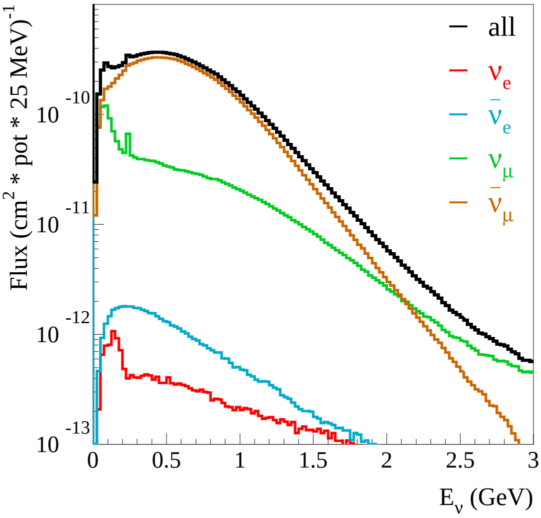

Figure 3.1.3: *Neutrino flavour spectrum in antineutrino beam mode.*

.

For the determination of the pion angular distribution, we use Rein and Sehgal's method for the $\Delta(1232)$ resonance. For the other resonances, an isotropic distribution in the resonance rest frame is assumed. The Pauli blocking effect is also simulated in the decay of resonances, by requiring the nucleon momentum to be larger than the Fermi surface momentum. This suppresses the interaction cross section by a few percent. In addition, pion-less Δ decay is also accounted for, and 20% of the resonant events are simulated with no pions produced at the neutrino interaction vertex.

In the Rein and Sehgal method, the neutrino induced single pion production occurs in two steps (equation 3.2.1).

$$\nu + N \to l + N^*; \quad N^* \to \pi + N' \tag{3.2.1}$$

Where N and N' are nucleons and N^* are the baryon resonances. The pion production cross section is obtained with the product of both steps

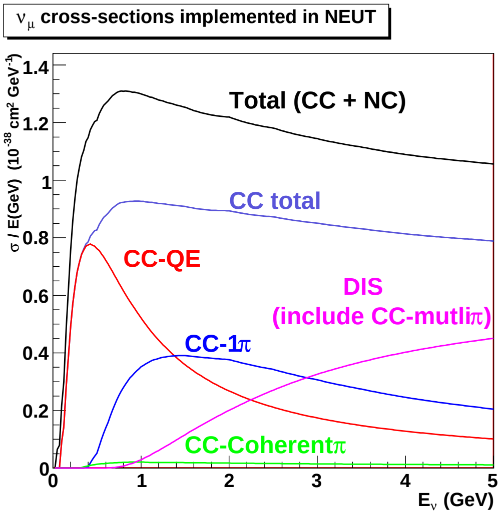

Figure 3.1.4: *Charged current neutrino cross sections divided by neutrino energy as a function of energy (in GeV).*

in equation 3.2.1. In the first step, the resonance production amplitude is calculated. In the second the probability of the pion and nucleon production through the resonance decay is calculated. Eighteen resonances with masses below 2 GeV/c^2 and their interferences are taken into account. Among them, the main contribution to the single pion production comes from the $P_{33}(1232)$ resonance at SciBooNE energies.

- Deep Inelastic Scattering (DIS) is the dominant interaction in the high energy region, above few GeV. Equation 1.3.6 in Section 1.3 is used to simulate the deep inelastic scattering. The DIS manages interactions with W above 1.3 GeV. However, the pion production in the range 1.3 GeV $< W <$ 2 GeV is modified by the probability function of pion multiplicity to avoid double-counting, given that the DIS can also produce single pion events.

  The parton distribution functions, F_2 and xF_3 [66], are extracted from charged lepton and neutrino scattering experiments at high energies. However, parton distributions derived in this way are not applicable in the small W or q^2 region and corrections have been applied. Corrections

	# of ν_μ events
CC-QE	38,900
CC-1pi	23,900
CC-coherent	1,200
CC-multi pi	5,300
NC-1pi	8,600
NC-coherent	700
NC-multi pi	1,700
NC-elastic	17,400

Table 3.2.2: *Number of neutrino events expected for* 10^{20} *POT and 10 tons of fiducial volume in neutrino mode. Antineutrino events in neutrino run mode is expected to be less than* 2%*.*

were proposed by Bodek and Yang [67] and the correction parameters are obtained by fitting various existing experimental results.

- Coherent pion production is simulated using the model by Rein and Sehgal [68], with a value for the coherent axial mass of $M_{A,coh} = 1.1$ GeV and the nuclear radius parameter set to $R_0 = 1.0$ fm.

Tables 3.2.2 and 3.2.3 give the number of neutrino and antineutrino events expected for 10^{20} POT and 10 tons of SciBar fiducial mass in neutrino and antineutrino running modes, respectively.

Finally, nuclear effects affecting produced hadrons are also implemented on NEUT. Nuclear effects take into account the re-scattering in the nucleus of the pions, kaons and many other hadrons. NEUT uses the cascade model where each particle is tracked inside the nucleus until it escapes. Regarding pions, inelastic scattering, charge exchange and absorption interactions are taken into account. Also, for high energy pions, particle production is accounted.

The mean free path of these various intranuclear mechanisms are calculated from a Delta-hole model [69] at low energy, $p_\pi < 500$ MeV/c, and from pion-proton scattering cross sections at high energy, $p_\pi > 500$ MeV/c. At SciBooNE energies, approximately 15% of pions are absorbed in carbon, about 20% undergo inelastic scattering, and the probability of pion charge-exchange is about 5%.

	# of $\overline{\nu}_\mu$ events	# of ν_μ events
CC-QE	7,500	3,000
CC-1pi	2,100	2,000
CC-coherent	500	90
CC-multi pi	500	660
NC-1pi	1,300	700
NC-coherent	300	60
NC-multi pi	130	200
NC-elastic	2,900	1,300

Table 3.2.3: *Number of antineutrino and neutrino events expected for* 10^{20} *POT and 10 tons of fiducial volume in antineutrino mode.*

3.3 Simulation of the SciBooNE Detector Response

Detector simulation chain starts taking the output from NEUT interactions and using it as input for the GEANT4 software. The geometry (Fig. 3.3.1) of the detectors was introduced using the measurement during the installation and the results from the survey group.

NEUT final state particles are passed to GEANT4 for propagation in the detector material, taking into account all relevant strong and electromagnetic processes, and weak particle decays. For the neutrino target mass, we simulate the density of the SciBar scintillator to be 1.021 g/cm^3, as obtained from a measurement before installation.

Using the "true" energy deposited and timing information of the GEANT4 tracks, Analogical to Digital Converter (ADC) and TDC from SciBar is simulated. The conversion from MeV of deposited energy into PEs is done in two steps. First, an energy deposit of 2.04 MeV/cm is assumed for minimum ionizing particles (MIP). Second, cosmic ray muons are used to infer the conversion from MIP deposited energy units into PEs. This second step is simulated separately for each channel, as explained in the calibration section (Figs.4.1.2 and 4.1.3 in Sec.4)

For the energy, the scintillator quenching for every bar crossed by the track is simulated, with a Birk's saturation parameter of 0.0208 cm/MeV. Given the deposited energy in every bar in the detector, the fiber attenuation is taken into account as explained in Section 4.5. Next step is to simulate the PMT response taking into account the single photoelectron charge resolution of the

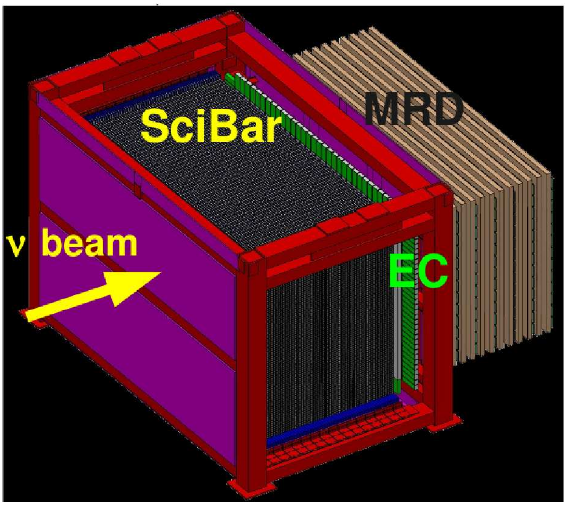

Figure 3.3.1: *GEANT4 detector display using the implemented geometry information.*

Hamamatsu PMTs measured at Kyoto University and FNAL. We assume a 50% resolution for all SciBar PMTs. Cross talk in the multi anode PMT is also simulated introducing “fake” hits around the actual track. For a more detailed description of the cross talk effect, see Section 4.1. Finally, the photoelectron to ADC counts conversion is performed and some electronics noise is introduced.

The timing information simulation takes the “true” timing from GEANT4 and adds the propagation time through the fiber. An OR gate is used for hits above the TDC threshold for all 32 channels in each TDC. If there are hits above the threshold, the time is converted to TDC counts and stored in the event. A TDC dead time of 55 ns is also simulated, as is the TDC multi-hit capability.

Electron Catcher simulation starts also with the true information from GEANT4. The EC fibers attenuation is considered as well as the PMT response to the photo-electrons. We assume 9.76 photo-electrons per MeV of deposited energy, and a single photo-electrons (p.e.) charge resolution of 35%. EC PMT have a time-dependent gain, also called bunch to bunch gain dependency, that is due to the positive tail on the signal produced by the PMT’s. This time-dependent gain is also simulated in the detector response software to be able to use the same exact calibration and reconstruction software for the data and the Monte-Carlo. Finally, the produced photo-electrons are converted to ADC counts assuming 7.7 ADC counts per p.e.

MRD response simulation takes also in acount energy and time information. To simulate the response of the energy deposit, we simulate the scintillator quenching and the attenuation of the light through the scintillator and light guide. Gaps between scintillator counters, which cause about a 1% hit finding inefficiency, are also simulated. Then, photo-electrons are converted to ADC counts and also the electronic noise is added. For time information, the propagation time is computed before converting time to TDC counts.

Once the detector simulation is processed, Monte-Carlo events are introduced into the SciBooNE Analysis Framework for parallel processing with the data.

Chapter 4

Detector calibration, track reconstruction and particle identification

In this chapter, calibration (Secs. 4.1-4.3) and event reconstruction (Secs. 4.4-4.7) details for the SciBooNE experiment are given. During the course of this thesis, I have been directly involved in several calibration and reconstruction tasks. For this reason, a detailed explanation of those follows.

4.1 SciBar Calibration and alignment

As explained in Section 2.2, SciBar has 4 different triggers. Three of them (LED, pedestal and cosmic triggers) are used for calibration. In this section calibration of SciBar will be described step by step.

As already mentioned, SciBar readout is done by 64-channel multi-anode PMTs (Section 2.2). Time and charge information must be calibrated and the calibration is done in several steps starting from the raw data.

The first step is to calculate the ADC pedestals and subtract them from the signals. To calculate the pedestals, the mean ADC counts of all the pedestal trigger events is calculated in a subrun timescale for each of the 14336 channels. A typical subrun is set to contain around 740 pedestal trigers, and typically lasts about 30 minutes.

The pedestal values for each channel and subrun are stored in the Sci-

BooNE database. As can be seen in Figure 4.1.1, average ADC mean values for pedestals are 2000 counts with a RMS average of 1.6 counts. We remind that SciBar uses 12 bit ADCs, corresponding to an ADC dynamic range of $[0, 2^{12} - 1] = [0, 4095]$.

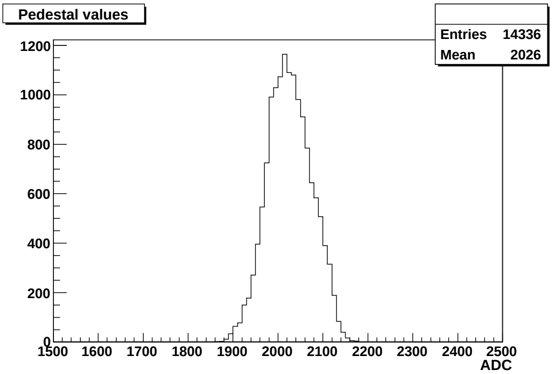

Figure 4.1.1: *ADC pedestal values for all SciBar channels in a typical subrun.*

Once calculated, the pedestals are used to filter the signal over the electronic noise. Only channels with ADC counts 3σ above the mean pedestal values are considered. PMT gain variation in time is corrected before any conversion to energy or photoelectrons. The MA-PMT gain is corrected using the LED trigger, when a monitoring LED injects light to all channels. The MA-PMT gain is given by Equation 4.1.1. Gain variation correction is done channel by channel in a run by run time scale and the corrected ADC value is given by Equation 4.1.2, where run 11002 (the beginning of the neutrino run) is used as the baseline run. Gain variation corrections for typical channels are of the order of 1%. At this stage, the channel ADC value can be converted to photoelectrons (p.e.), and to energy in Minimum Ionizing Particle (MIP) units. The conversion constants differ channel-by-channel, but (unlike pedestal values) have the same value for the entire SciBooNE data-taking period.

$$MAPMT\ gain = \frac{MAPMT\ ADC\ counts}{LED\ monitor\ ADC\ counts} \tag{4.1.1}$$

$$corrected\ ADC = ADC \times \frac{gain\ (baseline\ run)}{gain\ (current\ run)} \tag{4.1.2}$$

For the ADC to photoelectron conversion (Fig. 4.1.2) values come from single p.e. ADC measurements done in Kyoto University and FNAL for every one of the MA-PMTs. The procedure is to histogram the ADC counts for very low light levels and make a fit over the 1 pe peak. The ADC to p.e. conversion value is the inverse value of the ADC count for the 1 p.e. peak, resulting in 0.159 p.e./ADC count in average.

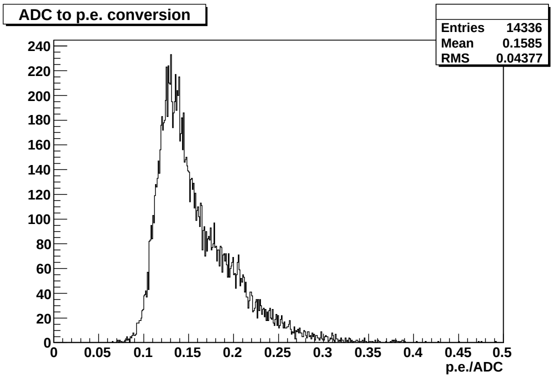

Figure 4.1.2: *Mean value for the ADC to photoelectron conversion constants for all SciBar channels.*

The MIP is the energy unit that corresponds to the energy that a Minimum Ionizing Particle deposits per cell (1.3 cm in the beam direction). To calculate ADC to MIP conversion values (Fig. 4.1.3), cosmic rays are used. After reconstructing cosmic ray tracks and correcting the number of ADC counts for the muon track length in the bar and for the attenuation length (see Section 4.5), the inverse of the mean value of ADC counts per cell is taken as the ADC to MIP conversion value. This is calculated channel by channel. In addition to this conversion, a global energy scale factor to convert energy from MIP to MeV units is applied for all channels, corresponding to the known energy deposit per unit track length of a Minimum Ionizing Particle in SciBar detector material of 2.04 MeV/cm [70].

At this stage, the calibrated charge information still contains around 0.3% of electronic noise. In addition, the charge information is also affected by the so called Cross Talk effect. In principle, the light from each fiber should be entirely collected by a single channel whose anode is perfectly aligned to the fiber end. In practice, light can spill to neighboring channels in the same MA-

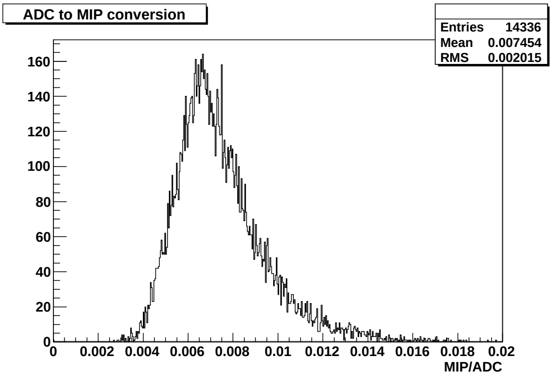

Figure 4.1.3: *Mean value for the ADC to MIP conversion constants for all SciBar channels.*

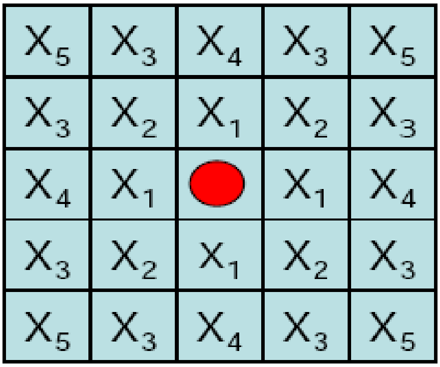

Figure 4.1.4: *Schematic X-Talk effect.* X_1*=3.55%,* X_2*=1%,* X_3*=0.6%,* X_4*=0.6%,* X_5*=0.1%*

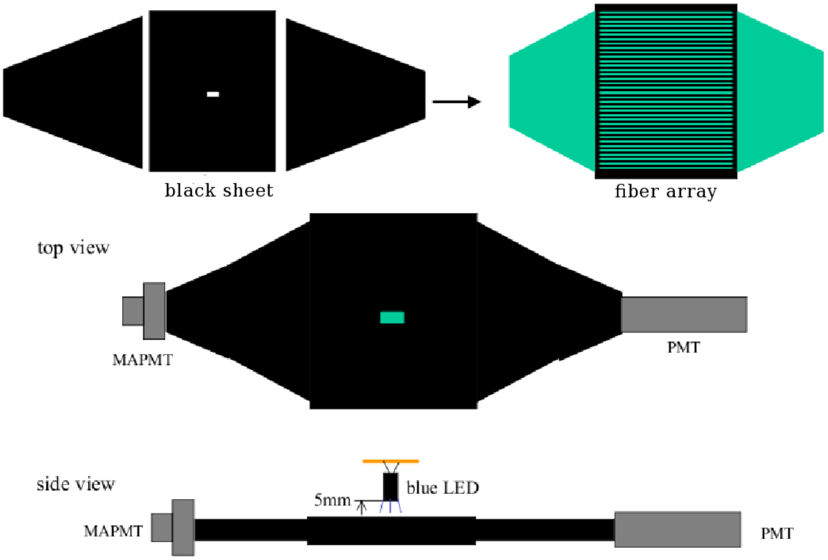

Figure 4.1.5: *X-Talk measurement experimental setup.*

PMT, causing cross talk among channels. That light is distributed following the scheme shown in Figure 4.1.4. This effect must be corrected to avoid "ghost" tracks generation.

The crosstalk correction is applied to both data and MC before event reconstruction. Let M be the 64×64 crosstalk matrix, where M_{ij} is the fraction of channel j's signal that migrates to channel i due to crosstalk. If q_i is the charge in channel i before crosstalk and q_i' is the charge in channel i after crosstalk, then

$$q_i' = \sum_j M_{ij} q_j. \tag{4.1.3}$$

The crosstalk correction is just the inverse process,

$$q_i = \sum_j M_{ij}^{-1} q_j'. \tag{4.1.4}$$

To calculate X-Talk values an experimental setup is used as follows. An array of 64 fibers with one end connected to the 64-channel MA-PMT and the

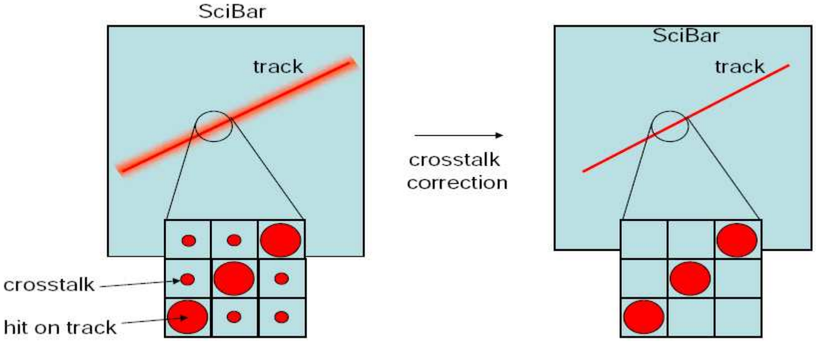

Figure 4.1.6: *Chart of the X-Talk algorithm correction effect.*

other end connected to a 2-inch PMT is used, as can be seen in Figure 4.1.5. One LED illuminates one fiber at the time through the window in the coating and the amount of light in all channels in the PMT is recorded. The X-Talk value is calculated as the ADC count ratio between channels corresponding to non illuminated fibers over the channel corresponding to the illuminated one.

This step removes the noise around the real track (see Figure 4.1.6). X-Talk correction parameters are calculated by inverting the matrix of light distribution shown in Figure 4.1.4 around each signal hit.

One more calibration step is performed for SciBar, that is to correct ADC counts by the fiber attenuation length. Since we need the 3D reconstructed track to know how far from the PMT the particle crosses the bar, this calibration will be discussed in Section 4.5.

In SciBar, time information is also important. Each multi-anode PMT has 2 TDC readouts, governing 32 channels each. TDC readouts are sensitive to the amount of charge deposited in the channel, triggering earlier for larger amount of charge: this is the so called time slewing effect, introducing a correlation between raw charge and time values. To compute the correction we have to apply, we calculate the difference betwen the time of the channel to be corrected (T_i) and a neighboring channel (T_0). A scatter plot of $T_i - T_0$ versus ADC counts (q_i) is made for each channel i. The dependence is close to an exponential function, so we make a fit using the following function:

$$T_i - T_0 = \frac{A}{q_i + B} + C \tag{4.1.5}$$

A,B and C are the fitting parameters and q_i the amount of charge in ADC counts.

To adjust the origin of time across all channels we use cosmic rays crossing all planes in SciBar. We first select cosmic rays crossing one single channel in the first layer and, taking into account muon time of flight and the propagation of light along the fiber, we use them to adjust T_0 in all channels of the last layer of SciBar. The T_0 of the channels of the remaining layers is adjusted using this last layer as a reference and the cosmic rays crossing such channels.

The reference time is set to be zero at the start of the beam spill. The average time resolution after corrections among all channels is 1.6 ns.

Layer spatial alignment is determined by surveying the position of four points per layer. Deviations up to 2 mm are found with respect the position of the first layer. The alignment of the layers and planes inside the detector is improved using cosmic ray data, as described in the following.

Having a cosmic ray crossing all layers in SciBar, we are able to make a linear fit over the track, but masking a layer every time. The alignment is done by calculating the deviation between the theoretical point where the cosmic hits a bar calculated from the fit and the nominal position of the hit determined by survey data. The alignment is calculated as the mean deviation from several events (around 60,000 events). Since all layer positions, except the first one that is our reference plane, are changed during the alignment, we perform 3 iterations in the process to reach better accuracy. After all iterations, the detector alignment deviation is smaller than 0.05 cm.

4.2 EC Calibration

As for SciBar, before proceeding to the hit level calibration, the pedestals must be subtracted. The pedestal ADC counts have been measured with pedestal triggers and found to be around 300 ADC counts. Next, light attenuation effects in the fibers are corrected. To calculate the attenuation length correction values, cosmic ray events have been used. Each EC module is divided into 8 longitudinal bins (33.75 cm each). Using SciBar track information, we determine the position of each EC hit along the module. Eight histograms are filled (one for each longitudinal bin) with ADC counts from the hits corresponding to each bin. Then a fit is made on the resulting distributions with the convolution of a Landau distribution and a Gaussian resolution function, to get the ADC most probable value (MPV) for each bin. We construct with the obtained MPV values a graph for each channel as function of the bin number i. The MPV values as a function of the distance are well fitted by a single exponential.

$$MPV_i = k \cdot e^{-x_i/\lambda} \tag{4.2.1}$$

Where x_i is the distance between the PMT and the EC longitudinal bin i, and λ is the attenuation length. Values of $\lambda \sim 4$ m are obtained on average. In addition, the double-ended readout of the EC modules allows to correct for any residual fiber attenuation effects, by using the geometric average of Eq. 2.3.3.

The bunch to bunch dependence is an effect related with the gain dependence from the integration time. The signal in the EC has a duration of 350-400 ns with a negative pulse height of ~150 mV and presents a very long positive tail called overshoot. The charge signal integrates this pulse, considering a larger fraction of this overshoot tail from early beam bunches compared to late ones in one spill. Time dependence effect is corrected for each channel i by using Eq. 4.2.2. The correction constants α have been calculated individually for each channel by using different integration times with cosmic rays:

$$C_{time[i]}(b) = \frac{b_{ref} + \alpha[i]}{b + \alpha[i]} \tag{4.2.2}$$

where b and b_{ref} refer to bunch numbers within the spill, the correction defined to be unity for the central bunch ($b_{ref} = 42$).

4.3 MRD Calibration

In the reconstruction of the muon, the energy is reconstructed using the range by using MRD TDC hit information only, discussed below.

First, TDC counts are converted into raw absolute times according to TDC module design specifications (0.5 ns per TDC count).

Then, the cosmic trigger is used. The cosmic trigger consists in the coincidence between the 1st and 13th planes or between the 2nd and 12th. Those are the first and last horizontal planes, and first and last vertical planes, respectively. Then, times must be corrected for light propagation and time of flight of the muon, where the light propagation was measured to be ~ 7 ns/m. Subsequent TDC calibration is performed with light propagation and TOF corrections applied.

Taking as a reference one TDC from the first plane, the time difference is measured for all other counters. For each channel a fit is performed over the time differences from a cosmic sample to calculate the time correction offset.

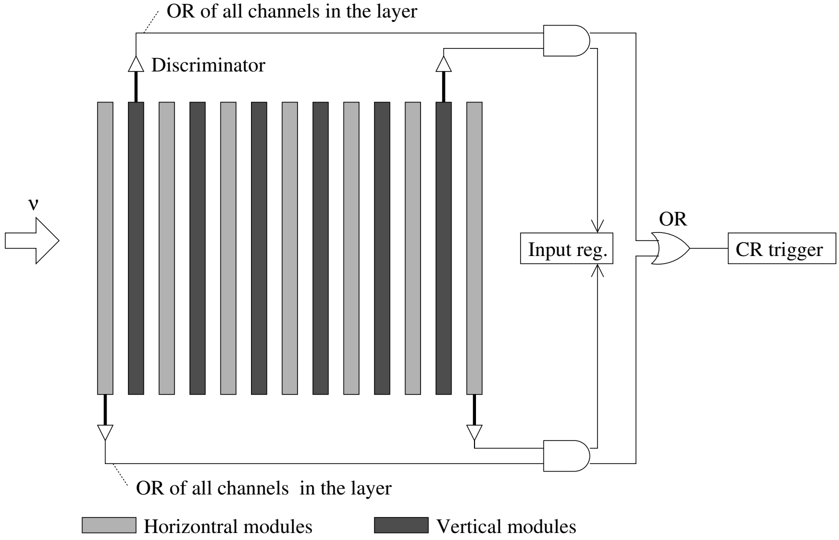

Figure 4.3.1: *MRD cosmic ray trigger schema.*

After applying the correction, a timing resolution of ∼ 1.2 ns was found, good enough to be able to see the bunch structure of the beam (see Figure 2.1.2).

4.4 SciBar 2D Track Reconstruction

For the SciBar track reconstruction a Cellular Automaton Tracker was already used for the K2K SciBar, and has been reimplemented in SciBooNE. SciBar Cellular Automaton Tracker (sbcat) is based on the same principles than the game of life. A cellular automata is a dynamical system which evolves in discrete time steps and usually in a two-dimensional space divided in cells. Each cell can take several states described by a value.

The laws of the evolution are local. That means that the dynamics of the system is controlled by a fixed set of rules and the new state of a cell is calculated on the basis of its neighboring cells states. The change of states are made simultaneously and in parallel for all cells. The SciBar geometrical setup, organized into layers, is the reason why a segment model for the Cellular Automaton algorithm has been chosen.

The energy deposited by particles crossing the detector is given as a set of hits distributed in the two views. If some contiguous hits in the same layer (X or Y directions) are found, a cluster is created. The cluster energy is the sum of the energy of the cluster hits, and the time and position is the average position and time of the hits. At this stage, hits are treated like one hit clusters.

A segment is a straight line that connects two clusters. The clusters must be in adjacent layers to be connected. Besides, for clusters containing only one hit, the angle of the segment with respect the z-axis must be smaller than 1.1 radians.

To create tracks, the segments have to be connected. To connect two segments they have to be consecutive, having one point in common. Also, the segments must be compatible with being a track. For each two consecutive segments, a linear fit using the edge position of both segments is performed. The χ^2 of this fit must be smaller than 4.5 to consider the segments compatible with being a track.

The track is constructed starting from the most upstream segment with an unconnected upstream extreme. This is a first level segment. Level 2 is assigned to the segments connected to the first level segment. A weight is assigned to each segment according to the level. Every time that a free edge is found, a track is created. The weight is equivalent to the time evolution of the track. A minimum length of 3 layers to reconstruct a track is required, corresponding to 8 cm.

The evolution rules of the cellular automaton, using the game of life nomenclature, can be summarized as follows (see Figure 4.4.1):

- **Cell (segments)**: For each of the two SciBar views, along X and Y, a cell is identified as a straight line segment connecting two hits in neighboring layers. The cell weight represents the position of a cell within a track, also called level of evolution.

- **Neighbors**: Two cells are neighbors if they have a common edge.

- **Rules**: The cell are initialized with a position value equal to 1. During each evolution step and for each cell the algorithm looks for forward neighboring segments, increasing their level of evolution by one unit. The evolution stops when no more forward neighboring cells are found.

- **Time**: Time evolves discretely, with all cells in the same level evolving simultaneously.

A large fraction of fake tracks may be produced at this level in the sense that for the same set of hits, several tracks can appear. Hence, a second

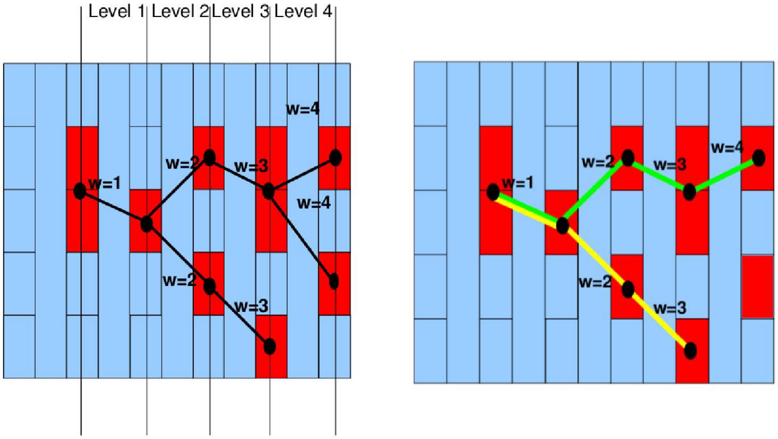

Figure 4.4.1: *Segment, level and weight definition and created tracks.*

step selects the best track candidates. Good rejection power of fake tracks is accomplished at this level, while keeping high track finding efficiency for true tracks, as described below. If 2D tracks have less than 3 non common hits, the longest track is chosen. If the tracks have similar length, less than 3 layers of difference, a linear fit is performed and the track with smaller χ^2 is preferred. On the other hand, if 2D tracks have more than 3 non common hits, they are not removed and the smaller is stored as split track of the longest one.

The reconstruction efficiency for single tracks with length greater than 10 cm is 99%.

4.5 SciBar 3D Track Matching

The 2D tracks are nothing more than the projection over the XZ and YZ planes of the 3D track created by the particles. The 3D track reconstruction is obtained by matching 2D tracks from both top and side views having common edges. The matching process follows a criterion with an order of preference based on the distance between the edges of the tracks in both projections. Figure 4.5.1 shows the class of the matching for the different cases considered. Class I corresponds to tracks with starting edge situated in the same layer, that is separated by one plane (1.3 cm). Class II and class III are considered to take into account xtalk and vertex activity effects and allows one and two

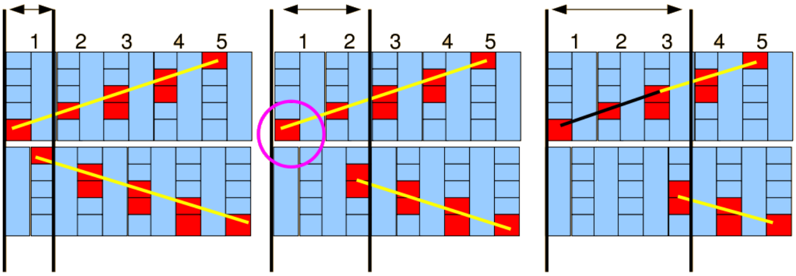

Figure 4.5.1: From left to right: *Class I, II and III 3D matching cases. Top and bottom tracks corresponds to XZ and YZ views. Layers, containing one plane of each view are numbered. Classes II and III are implemented to consider X-Talk (center) and vertex activity (right) in the tracks.*

layers of separation, respectively.

When several 2D tracks in one view are competing to match with one in the other view, the χ^2 of energy deposition criterion is applied. The χ^2 is calculated as the difference of the energy deposition of every hit in one plane and the mean energy of its two neighbours.

Similar track times are also required. Only 2D tracks with a time difference of less than 50 ns can be successfully matched to each other.

Once 2D tracks are matched, we are able to perform the last correction to the ADC value of the hits, that is the correction for attenuation length. SciBar fibers have a measured attenuation length of 3.48 meters on average (see Figure 4.5.2). Knowing the 3D position of a hit, we can calculate the distance from the energy deposited by the particle to the PMT, that allows us to correct the ADC value by the attenuation length of the fiber and also by the time the light takes to reach the PMT.

4.6 SciBar-MRD Matching and Particle Identification

As a general Charged Current event definition one “on time” track starting in SciBar is required to reach the MRD. Those events are called MRD-matched events. The requirement for a SciBar track to be matched with the MRD is to point towards a transverse distance of 10 cm around the starting point

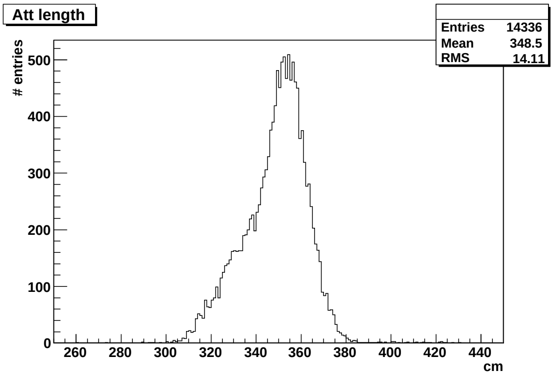

Figure 4.5.2: *Measured light attenuation length of SciBar fibers.*

of the MRD track and with a maximum angle difference depending on the muon momentum, from 0.4 rad for more energetic muons, that are not much affected by rescattering, to 1.1 rad for less energetic ones. Because a length of 4 layers is required to reconstruct MRD tracks, and many times muons have not enough energy to cross four layers, a hit based matching is also applied when MRD tracks are not available. Hit based matching consists on extrapolating SciBar reconstructed tracks and look for MRD hits on the first layer around the SciBar extended track trajectory.

The muon angle (θ_μ) is measured using only SciBar track information, which is more accurate and it is not affected by the possible rescattering in the EC or MRD that can affect the MRD part of the track. The cosine of the angle is obtained taking the distance traveled by the particle inside SciBar in the beam direction and dividing it by the distance traveled in the transversal direction: $cos(\theta) = Z/T$ where $T = \sqrt{X^2 + Y^2}$ and Z,X and Y are the traveled distances in the Z, X and Y directions respectively.

The muon momentum (p_μ) is calculated through the muon kinetic energy (E_{kin}) using range information and the expected energy deposition (dE/dx) in each detector. The muon kinetic energy is measured as follows:

$$E_{kin} = E^{SciBar} + E^{EC} + E^{Wall} + E^{MRD} \tag{4.6.1}$$

where $E^{SciBar} = 2.04$ MeV$/cm \times L_{SB}$ (being L_{SB} the reconstructed track length in SciBar) $E^{EC} = 90.8/cos(\theta_\mu)$ MeV, $E^{Wall} = 3.3/cos(\theta_\mu)$ MeV and E^{MRD} is computed with a range to energy table obtained using the

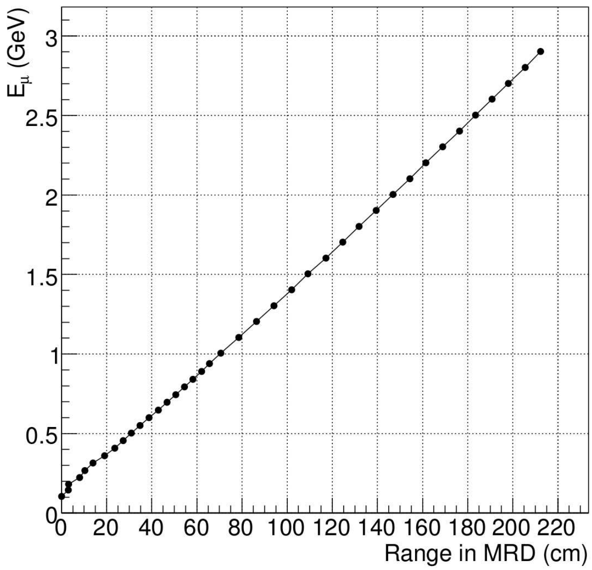

Figure 4.6.1: *Range to muon energy conversion table for the MRD detector.*

MC. Fig. 4.6.1 shows the range to energy conversion table used to calculate E^{MRD}. For muons stopped inside the MRD, the muon momentum resolution is 50 MeV/c

Analysis of fully contained events in SciBar is also performed. Muon tagging is done by looking for a *michel electron* at the end of the muon track, that is a decay electron from muon decay at rest. Even if the michel electron track is too short to be reconstructed, we are able to infer the presence of the michel electron using the TDC information. If a michel electron is present, we are able to see a second TDC hit about 2 μs after the muon track. In Figure 4.6.2 the time difference between the muon track and the second TDC hit at the end of the track can be seen. Figure 4.6.2 also shows a fit to an exponential corresponding to a muon lifetime of $(2.003 \pm 0.047) \times 10^{-6}$s, in good agreement with expectations. The muon kinetic energy for SciBar-stopped muons is calculated with a range to energy table build specifically for SciBar using the MC.

In addition to MRD matching and *michel electron* tagging, particle identification is also based on SciBar dE/dx information. While MRD matching

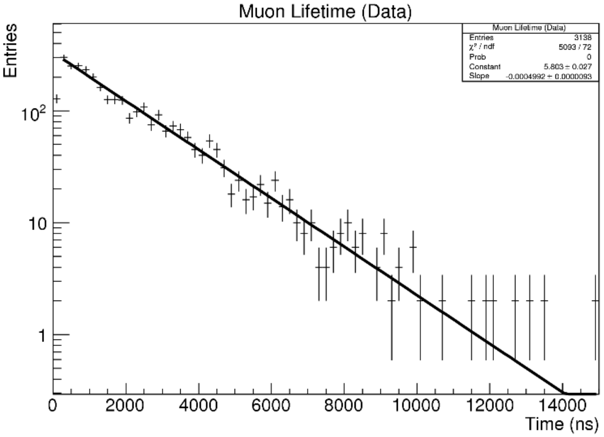

Figure 4.6.2: *Life time for muons stopping in SciBar.*

is effective to distinguish between muons and other particles as charged pions and protons, dE/dx information is used to separate proton from charged pion, muon, and electron tracks. In the SciBooNE energy range, protons leave a larger amount of energy per unit track length while pions and other light particles act as mips leaving less energy per track length, as shown in Figure 4.6.3. This fact allows us to define the Muon Confidence Level (MuCL). Confidence level is first defined plane by plane as the fraction of the expected dE/dx for muons over the observed dE/dx of the track. The expected dE/dx for muons is obtained from cosmic-ray muons. The Muon Confidence Level (MuCL) of a track is calculated by combining the confidence level of each plane in the following way:

$$MuCL = P \times \sum_{i=0}^{n-1} \frac{(-lnP)^i}{i!} \tag{4.6.2}$$

where $P = \prod_{\imath=1}^{n} CL_i$, n is the number of planes penetrated by the track, and CL_i is the confidence level at the $\imath$-th plane

In this way, MuCL tells us how similar is a track is to a minimum ionizing particle track, as can be seen in Figure 4.6.4.

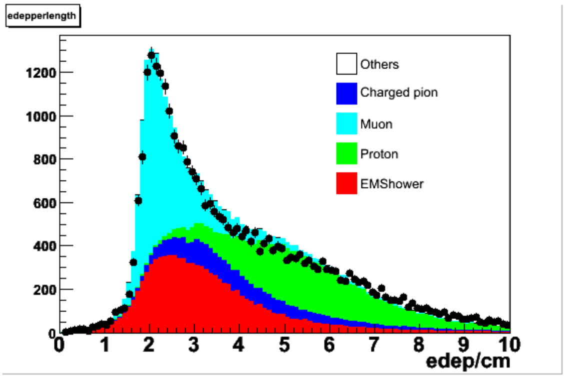

Figure 4.6.3: *dE/dx distribution for 2 track, non MRD matched events.*

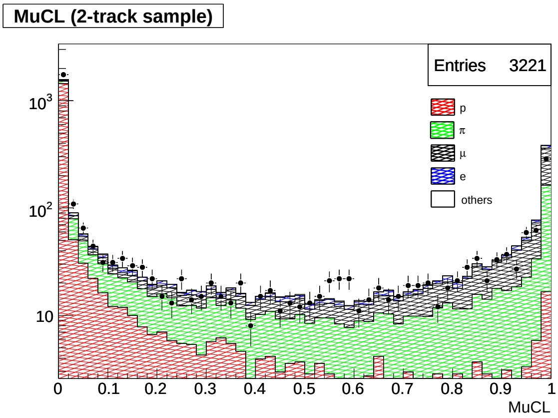

Figure 4.6.4: *MuCL distribution of the MRD stopped, 2-track sample. MC is normalized by the number of MRD matched events.*

4.7 2nd Reconstruction.

The default track reconstruction has a poor performance for events with high track multiplicity (3 tracks or more). This fact is mainly due to track overlapping in one of the two views. For this analysis, a second step in track reconstruction has been done increasing by a $\sim 50\%$ the high track multiplicity statistics.

To improve the high track multiplicity event reconstruction the first step has been to store the tracks reconstructed by the default SciBar Cellular Automaton Tracker (sbcat) and seek for hits that have not been used to reconstruct those tracks. Those hits are called 'Free Hits'.

Then, sbcat is run again using the free hits as input and new projections are reconstructed. Given that the hits associated to the default reconstructed tracks are not processed this time but only the free hits are, it is easier for sbcat to find new projections and short tracks. Those new projections will be matched to reconstruct new tracks.

Before the projection matching, another step is done. Taking the free hits left after the 2nd sbcat, a transversal sbcat (sbtcat) is applied. The sbtcat is applied having in mind the topology of the $CC - \pi^0$ events with high angle tracks being produced.

The sbtcat is a modified version of sbcat where layers and channels have been switched. This modification is equivalent to apply a 90^o rotation to the SciBar detector as shown in figure 4.7.1, so the track finding algorithm works in the transversal direction and not in the beam direction as sbcat does. In this way, new projections with angles close to the X and Y directions can be created. Finally, a matching between the new created projections is made in order to create new 3D tracks.

The 3D matching for those new projections follows the same rules than the default matching. The result of the 2nd reconstruction is about 15% more high track multiplicity events.

4.8 Extended Tracks.

Given the peculiarities of the electromagnetic showers produced by photons in SciBar, sbcat fails to reconstruct correctly the showers in the following ways:

- Splitted tracks. Gammas not producing showers but compton electrons can be reconstructed as two or more single and disconnected tracks one after the other and following the same direction.

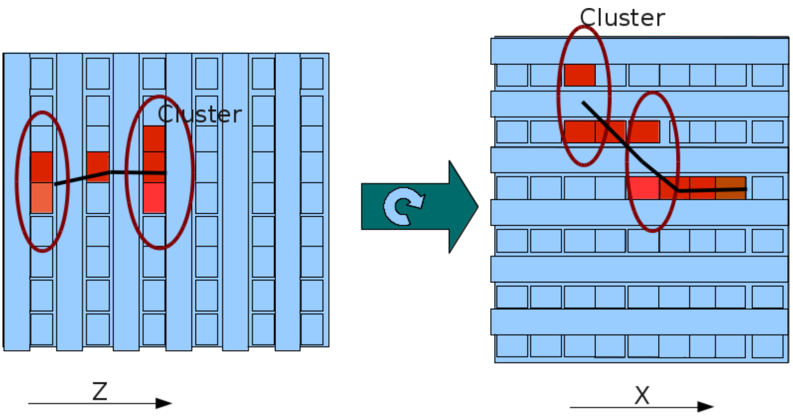

Figure 4.7.1: *Diagram showing the rotation applied in sbtcat and the change in what is considered a cluster.*

- Disconnected hits. Showers can produce wide tracks and sometimes sbcat reconstructs only thin tracks, because it is unable to collect all the hits around this track.

A software package has been developed to handle this kind of track. In general, what we want is to join splitted tracks and collect surrounding hits in order to correctly reconstruct the size and the energy of the electromagnetic showers.

In particular, the ExtendedTracks package looks for tracks that follow the same direction with a gap smaller than 10 cm between them. Those tracks are considered one single track by the software and a new 3D track is created in substitution of the old ones. The new track has the combined properties of the tracks from which it originates. The initial edge of the track is the same than the initial edge of the first track and the end edge is taken from the last track.

For two tracks to be considered one extended track, they have to meet some requirements:

- Distance between the tracks. The distance between the end edge of the first track and the initial edge of the last track should be smaller than 10 cm.

- Similar time. The time difference between the tracks has to be less than

20 ns to be joined in a extended track.

- Similar MuCL. Both tracks should have a MIP-like dE/dx in order to be joined in a extended track. For the MuCL variable, the minimum is set to 0.03.
- The reduced χ^2 of a linear fit to the extended track should be smaller than a given threshold. XZ and YZ projections are fitted separately. The hit positions of the track projections forming the extended track are fitted according to a straight line function. The resulting reduced χ^2 of the fit should be smaller than 10. In this way, only tracks that follow the same direction can form an extended track.

Also, the Extended Track algorithm collects all the hits that are not associated to any other track and whose distance to the main track is smaller than 10 cm.

The hits are added if they meet the following requirements:

- distance to the extended track smaller than 10 cm
- the hits are not associated to any track projection, or the track projection which are associated to is shorter than 10 cm.
- the time difference between the hit time and the time of the extended track is smaller than 20 ns
- the hit has at least 10 p.e. of energy.

The extended track list is used in the following for the event selection and particle reconstruction and it includes the actual extended tracks plus the single tracks that are not used to create any extended track.

While the angle reconstruction for all particles is calculated in the same way as the muon, as seen in Sec. 4.6, the momentum reconstruction for the non-muon particles is based on the hit-by-hit deposited energy. The kinetic energy for the non-muon particles is obtained by adding the energy deposited in each of the hits forming part of the extended track.

Chapter 5

Analysis

In this chapter we will see the event selection (Sec. 5.1) and reconstructed quantities (Sec. 5.2) that lead to the neutrino-induced charged current neutral pion production analysis. The event selection has been made taking into account the low event statistics maximizing the number of selected events while keeping the purity as high as possible. In order to handle the relatively low purity after the event selection, we also performed a background subtraction using a fit over the data to evaluate the signal and background components (Secs. 5.3-5.4).

The mesurement of the Muon Neutrino induced Charged Current Neutral Pion production cross section will be finally presented in Sec. 5.5.

5.1 Event Selection.

Given the energy range probed by SciBooNE, two channels contribute to the majority of signal events. The first contribution is due to the production and subsequent decay of a Δ resonance in a charged current interaction. The second channel is charged current multi pion production through DIS. For this analysis, signal events are characterized by a muon track and a π^0 coming out from the interaction nucleus. All other event topologies will be considered background. This signal definition based on final state particles is chosen because CC-π^+ events with a pion charge exchange inside the interacting nucleus will be indistinguishable from a CC-π^0 at the neutrino interaction vertex.

Since neutral particles do not deposit energy in SciBar, neither neutral pions nor the two photons in which it decays the 98.8% of the times can be directly detected. An object called 'Gamma Candidate' is defined to refer to tracks and energy clusters created by the electrons and positrons produced during the electromagnetic shower (EM) when photons convert. Therefore, the final state topology that characterizes CC-π^0 events in SciBar is a muon coming out from the event vertex [1] and two gamma candidates either reconstructed from a track in SciBar or a cluster of energy in the EC.

The cuts described below are applied to the full DATA sample in order to select CC-π^0 events. The cuts have been chosen trying to maximize the purity of the CC-π^0 event sample without loosing much selection efficiency. Several DATA/MC comparison plots will be shown below. Unless otherwise specified all MC distributions are absolutely (POT) normalized.

1. At least one MRD-matched track. As a definition of charged current event, a set of three event filters are applied. This set of filters is common for all the SciBooNE high energy CC analyses and is the definition of MRD-matched event. The filters are:

    - A SciBar track pointing towards MRD track or hits. As explained in Sec. 4.6, the SciBar track must point to a reconstructed MRD track or, if there is not a reconstructed track in MRD, must point to a set of MRD hits. Either track or hits must start in an acceptance area of 264×222 cm^2 in the first layer of the MRD.
    - Both SciBar and MRD tracks inside the beam time window. Only tracks inside the 2 μs beam window are considered for the MRD matching. This cut is also applied to reduce cosmic ray background as can be seen in Figure 5.1.1.
    - Neutrino interaction inside the Fiducial Volume. To avoid cosmic ray and other external backgrounds the tracks are required to start inside a volume of $260 \times 260 \times 154.6$ cm^3 (9.6 tons) in SciBar. Figure 5.1.2 shows the interaction vertex position in SciBar, considered as the upstream edge of the SciBar-MRD matched track. Muon tracks are used for the vertex position reconstruction beacuse they emanate from the neutrino interaction vertex in CC interactions, and because they are a minimum ionizing particle that leave a clean and long track inside SciBar while other particles leave more blurry tracks.

      The Fiducial Volume in SciBar is defined as follows:

      $$-130 \text{ cm} < X, Y < 130 \text{ cm and } 2.62 \text{ cm} < Z < 157.2 \text{ cm}$$

---

[1] We will consider the initial edge of the μ track as the event vertex.

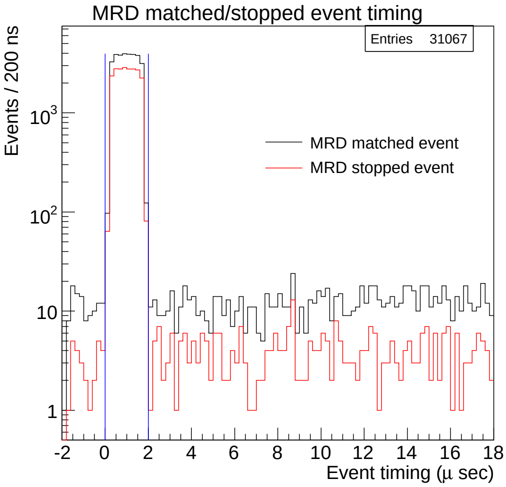

Figure 5.1.1: *Timing distribution of SciBar-MRD matched event (CC sample). Entire neutrino mode data (9.90E19 POT) are used for this plot. We found 29871 MRD-matched event in the beam timing window (shown in blue line) while the number of estimated cosmic backgrounds is 125.2 (0.4%).*

in the SciBar system of reference.

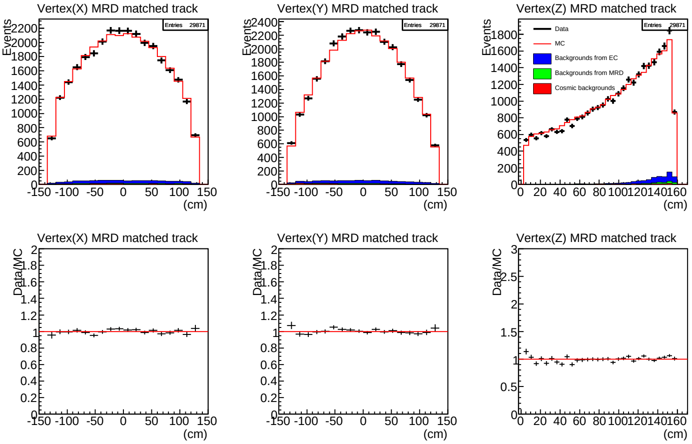

Figure 5.1.2: *Vertex distribution for MRD-matched tracks in X, Y and Z directions. Red line on top plots shows area-normalized Monte-Carlo, and filled histograms show the small background contributions from cosmic rays and EC/MRD neutrino interactions. Bottom plots shows DATA-MC ratio.*

An MRD-matched track which matches those three conditions is called a muon candidate. This muon candidate sample contains a negligible fraction of cosmic ray muons. The reason is that most of the cosmic ray muons have high angles with respect the beam direction and so do not leave a track crossing both SciBar and MRD detectors.

2. One and only one muon. Do not expect events with more than one muon, that is one MRD-matched track. Besides, since the event vertex is defined by the start of the muon track, ambiguities are avoided by selecting events that contain only one muon.

3. Time cut. All tracks contained in the event are required to be on time with the muon track. This cut is applied to remove events in which one of the tracks is a cosmic ray crossing the detector during the beam time window, or a track produced by a secondary particle after a decay. The cut is set to 20 ns around the muon track time as shown in Figure 5.1.3.

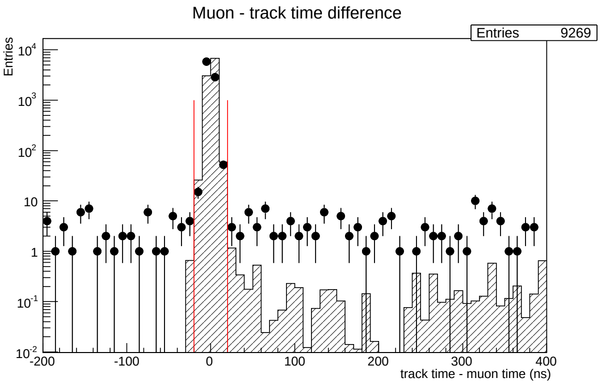

Figure 5.1.3: *Time difference in nanoseconds between muon and other tracks in the event. Dots are DATA, the filled histogram is MC. Beyond 400 ns, time differences extend uniformly in the entire 20 μs long DAQ window due to the cosmic ray tracks. Note that the MC simulation does not include any contribution from cosmic ray tracks.*

4. At least 2 Gamma Candidates. Gamma candidates are of three types depending on the way they are detected. The most common is a gamma that converts inside SciBar and whose track is completely contained in this detector. The second type of gamma candidate is a photon converting in SciBar that reaches the EC. In this case the properties of the gamma are defined by the SciBar track except for the energy, which is the sum of the deposited energy in SciBar plus the deposited energy in the EC cluster. Finally, a third type of gamma candidate is defined when the photon does not convert in SciBar but directly in the EC. In this case, the direction of the gamma is defined by the line that connects the event vertex with the EC cluster. Only one gamma candidate of the third type is allowed per event given the ambiguity in the position of the clusters if more than one is found. The following cuts are applied track by track to check whether they can be considered gamma candidates. The resulting number of gamma candidates found per event can be seen in Figure 5.1.9.

   - No tracks ending near the detector edges. This cut has two goals. First, it is a containment requisite for the gamma candidates. To achieve a good resolution in the π^0 energy and momentum reconstruction, it is important to recover as much electromagnetic shower energy as possible and the gamma candidates with leaking energy are rejected. Second, we apply this cut assuming all the tracks starting from the event vertex. The tracks entering the detector from the sides or upstream are reverted and also rejected, converting this cut also in a veto for cosmic rays and neutrino interactions that take place in the walls of the detector hall.

Only tracks with and ending point inside ± 135 *cm* for the transversal direction and $10 - 171$ *cm* in the beam direction can be considered gamma candidates.

- Disconnection cut. Most of the protons and charged pions present in the events come from the neutrino interaction vertex, while it is expected that photons travel on average for one radiation length (40 cm in SciBar), before converting and producing a visible signal. A natural quantity, then, to discriminate between photon track candidates and other types of tracks is the track flight distance, defined as the 3-dimensional distance between the track edge closest to the vertex and the neutrino interaction vertex. The disconnection cut is set to be at least 12 cm for gamma candidates. This cut has been set by maximizing efficiency times purity in a Monte-Carlo sample.

  Figure 5.1.4 shows the flight distance distribution for all the non-muon tracks to the event vertex. In this plot, the first bin will be removed by the cut. Figure 5.1.4 also shows the MC predictions for this quantity broken according to the true particle type responsible for the SciBar track.

- MuCL. The Muon Confidence Level is a quantity that characterizes the dE/dx of a particle(see Sec. 4.6). Tracks with MuCL close to 1 are muon-like tracks, produced by Minimum Ionizing Particles (MIP's). MuCL values close to 0 are proton-like tracks. Figures 5.1.5 and 5.1.6 shows the MuCL value by particle type. For the gamma candidates muon-like tracks are expected. Nevertheless, a study to maximize efficiency times purity has been made using the Monte-Carlo and it has been found that a MuCL > 0.005 cut rejects most of the protons while keeping a large amount of gamma candidates. The first bin in Fig. 5.1.6 will be removed by the MuCL cut.

- EC cluster energy. For the gamma candidates of the third type (gamma conversions in the EC), the energy deposited in the clus-

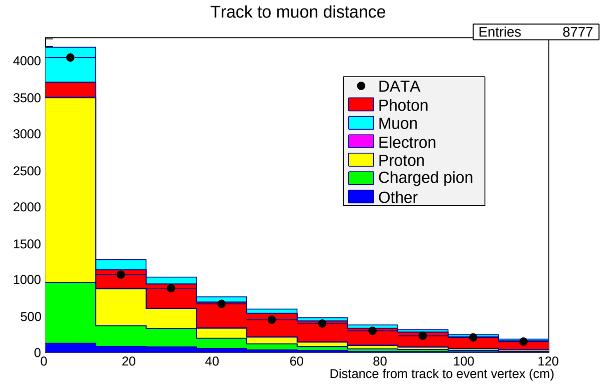

Figure 5.1.4: *Reconstructed flight distance distribution for all the non-muon SciBar tracks. The color histograms indicate the MC contributions according to the true particle type of the track, while the data are shown with points.*

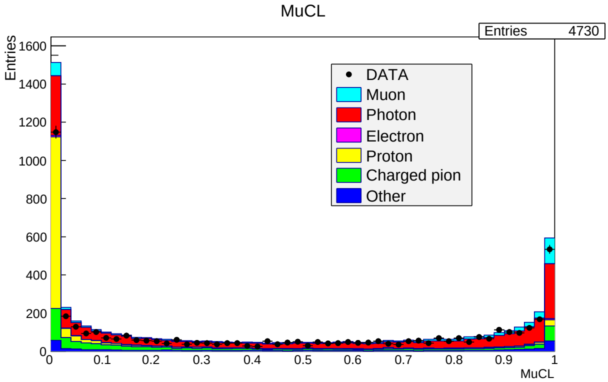

Figure 5.1.5: *Muon Confidence Level for all non-muon SciBar tracks in both DATA and MC. Only tracks with* $MuCL > 0.005$ *can become Gamma Candidates.*

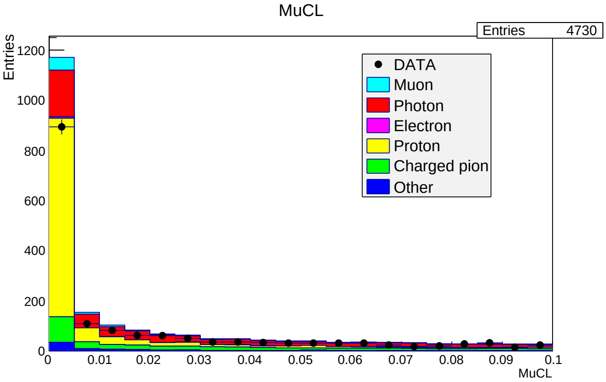

Figure 5.1.6: *Detail of the Muon Confidence Level for all non-muon SciBar tracks in both DATA and MC. Notice the finer binning in this plot compared to the previous one in order to better show the cut point. Only tracks with* $MuCL > 0.005$ *can become Gamma Candidates.*

ter of the first (top view) layer of the EC is required to be at least 15 MeV. For the gamma candidates converting in SciBar and reaching the EC (type 2) only geometrical matching is required. In Figure 5.1.7 and 5.1.8 the cluster energy in both EC layers is shown. The clusters coming from muons are selected by geometry matching and subtracted from the pool of clusters allowed to make gamma candidates.

5. Neutral Pion Candidate. To reconstruct a neutral pion we need at least 2 gamma candidates in the event. In addition, it is found that two gamma candidates with small opening angle between them reconstruct into neutral pion candidates with very low mass. This fact appears when a single electromagnetic shower produces two aligned tracks that are reconstructed independently. Such events correspond to either poorly reconstructed π^0s or to events with no π^0s, and we therefore reject them by requiring a minimum gamma opening angle (see below). The number of neutral pion candidates per event after applying the gamma opening angle cut can be seen in Figure 5.1.10.

   - GammaOpeningCosine. A cut is set over the opening angle of the two gamma candidates used to reconstruct a neutral pion. Again,

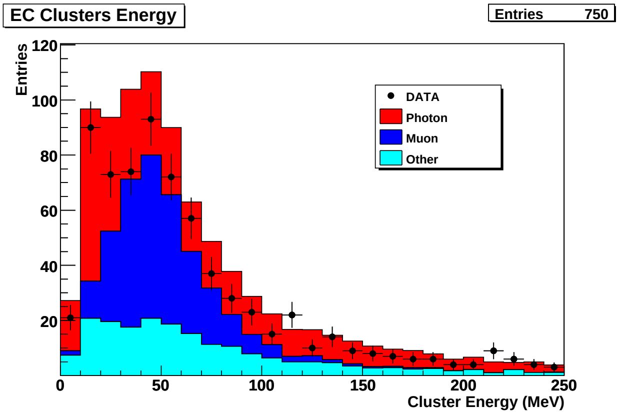

Figure 5.1.7: *Cluster energy in the 1st EC layer for both DATA and MC.*

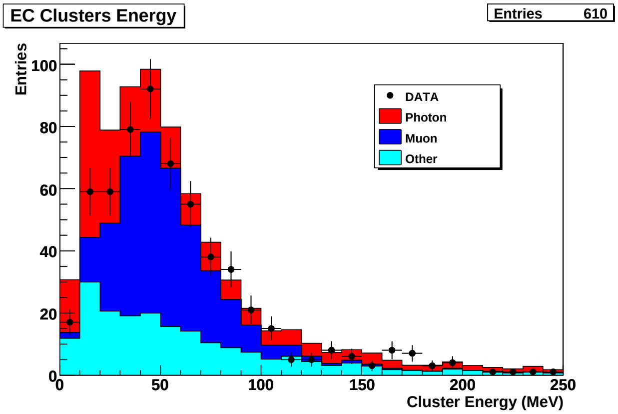

Figure 5.1.8: *Cluster energy in the 2nd EC layer for both DATA and MC.*

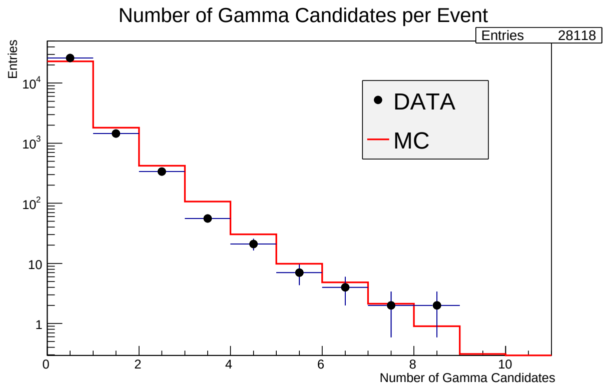

Figure 5.1.9: *Number of Gamma Candidates per event for both DATA and MC.*

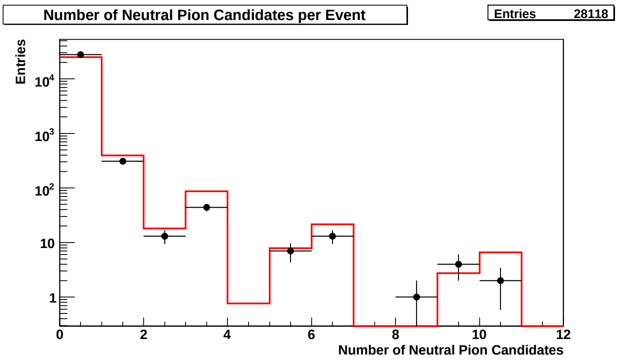

Figure 5.1.10: *Number of Neutral Pion Candidates per event for both DATA (points) and MC (histogram).* The number of neutral pion candidates is given by the combinations of the gamma candidates in the event allowed by the opening angle cut. Because of simple combinatorics and if no opening angle cut was present, only 0, 1, 3, 6, 10... neutral pion candidates would be allowed, corresponding to the cases of <2, 2, 3, 4 and 5 gamma candidates respectively.

using efficiency times purity studies, the cut is set such that the cosine of the opening angle should be equal or smaller than 0.95. The opening angle between MC gamma candidates in terms of how good the neutral pion is reconstructed can be seen in Figure 5.1.11. As can be seen in the figure, a large contribution from badly reconstructed events is present for $cos(\theta) > 0.95$. Those events typically correspond to a photon whose track is split by the reconstruction algorithm and mimics two close photons, producing a reconstructed neutral pion which is biased toward the low mass region. A DATA/MC comparison of the γ candidates opening cut is also shown in Fig 5.2.5.

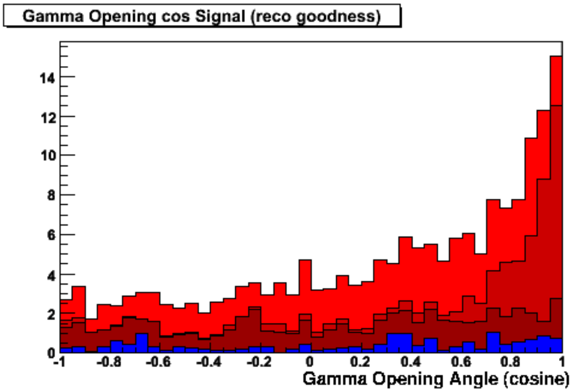

Figure 5.1.11: *Gamma Opening Angle for for MC signal events in terms of how good is the* π^0 *reconstruction. The lightest red histogram is a good reconstructed pion (2 gamma candidates that come from the same neutral pion). The darker red histogram correspond to only one gamma which comes from the neutral pion but reconstructs as 2 different tracks. The darkest red histogram correspond to a neutral pion reconstructed with one gamma which comes from the neutral pion and another track that does not. And the blue histogram corresponds to a neutral pion reconstructed by tracks that do not come from the neutral pion decay.*

6. 1 Neutral Pion Candidate. The last event selection cut applied to select $CC - \pi^0$ is to reject events containing more than 1 neutral pion.

Those cuts yield a final data sample of 308 events and give us an expected signal purity and efficiency expressed in Table 5.1.1. This table also shows the reduction in the number of data events after each sequential cut.

Notice that no requirements are set for final state particles other than gamma candidates and muon candidate tracks. Proton tracks are allowed but not required. This allows for both fully reconstructed and partially reconstructed events. The same applies to charged pion tracks, allowing to reconstruct either resonance or multi pion events.

	# Events	Purity	Efficiency
MRDMatch	30271	6.15%	27.39%
1 muon	29069	5.46%	23.14%
Track on muon time	28118	5.46%	22.93%
$\geq$ 2 Gamma candidates	428	36.38%	3.02%
1 π^0 candidate	308	38.23%	2.08%

Table 5.1.1: *Event selection summary table, showing the data events passing each cut with the absolute efficiency and purity for all cuts used in the* $CC-\pi^0$ *analysis.*

5.2 Kinematic distributions.

Once the event selection is done, the reconstruction of the particles and their kinematic properties can be performed. All DATA/MC comparisons shown below use an absolutely (POT) normalized MC sample.

Unless otherwise stated, the MC in the following plots is broken into four final state topologies: Signal events as defined above and three backgrounds. Background events containing neutral pions, events with no neutral pions, and events produced outside SciBar detector.

Background events with neutral pions are typically CC interactions where neutral pions are produced by hadronic interactions in the detector material away from the neutrino interaction nucleus. A small component of NC events with π^0s exiting from the target nucleus is also present.

As seen in Sec. 4.6, the muon momentum is reconstructed using the range information. The bump at high energies seen in Figure 5.2.1 is due to the muons escaping the MRD, and corresponds to the maximum muon momentum the MRD is able to reconstruct (1.2 GeV/c). This effect can be clearly seen by plotting the momentum of MC muons in terms of how the muon penetrates in the detector. In Figure 5.2.2 can be seen which fraction of muons are stopped inside the detector (blue), which fraction escapes through a side of the detector (red) and the fraction that escapes through the downstream part of the detector (green) which is the fraction that is concentrated at 1.2 GeV/c.

Also the angle θ_μ with respect to the beam direction is reconstructed (see Sec. 4.6) and can be seen in Figure 5.2.3. In this figure we can clearly see that the muons produced in the neutrino interactions travel mostly along the beam direction.

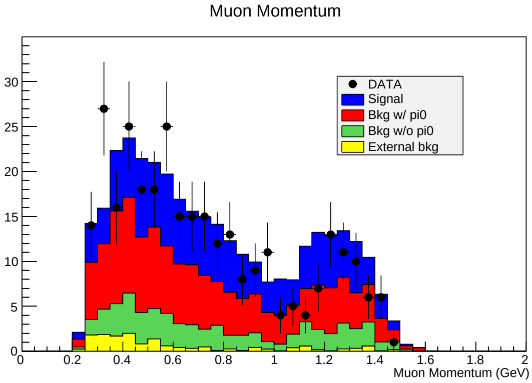

Figure 5.2.1: *Muon momentum of selected CC-π^0 events for both DATA and MC.*

The gamma candidates are also reconstructed. As the gamma particles cannot be directly seen in the SciBar detector, what is reconstructed is the electromagnetic cascade that a gamma photon produces inside the detector. The photons are reconstructed as extended tracks (as explained in Section 4.7) with a direction and an energy deposition associated to them, and as explained above, are identified by the dE/dx and the distance to the event vertex.

In Figure 5.2.4 can be seen the reconstructed energy of the gammas. Two entries per event are shown in Figure 5.2.4, accounting for the two photons in which the neutral pion decays. The opening angle between the photons can also be reconstructed. In Figure 5.2.5, the cosine of the gamma opening angle is shown. Notice that the bin 0.95-1 is missing. This is due to the cut in the event selection to avoid the overlapping of the gammas and the mis-reconstruction of the neutral pion mass.

The π^0 angle and momentum are reconstructed by using the momentum

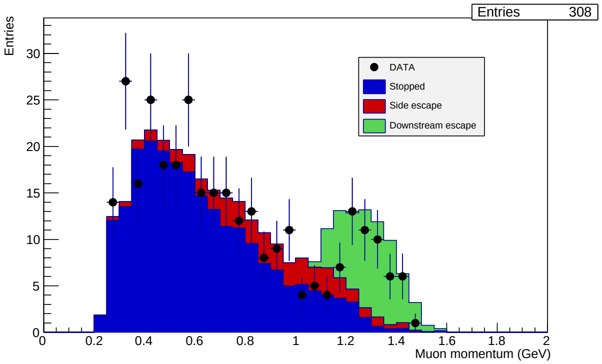

Figure 5.2.2: *Muon momentum in terms of the penetration in the detector. Blue histogram accounts for the MC muons stopped inside the detector. The red histogram color represents the MC muons that are escaping through one side of the detector. Green histogram represents MC muons escaping through the downstream edge of the detector.*

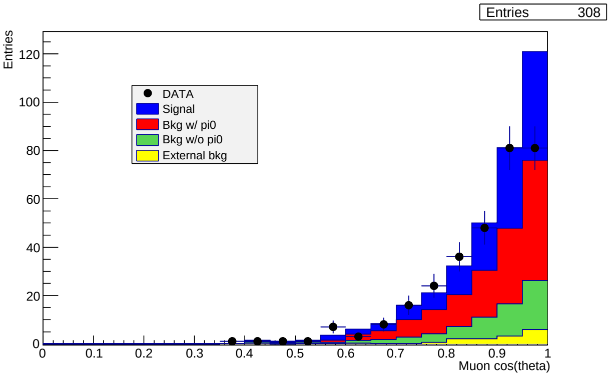

Figure 5.2.3: *Cosine of the angle of the muons with respect to the beam direction of selected CC-π^0 events for both DATA and MC.*

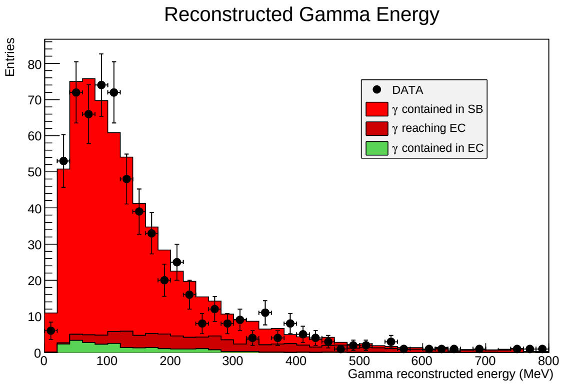

Figure 5.2.4: *Reconstructed energy for the gamma candidates. The Monte-Carlo is divided in terms of how the gamma is reconstructed: Shower contained in SciBar (dark red histogram), Shower starting in SciBar and reaching the EC (light red histogram) and Shower contained in the EC (green histogram).*

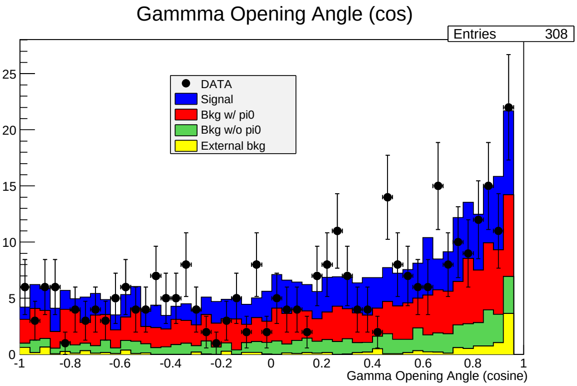

Figure 5.2.5: *Cosine of the opening angle for the two gamma candidates of selected CC-π^0 events for both DATA and MC. The bin 0.95 - 1 is missing due to the event selection cut to avoid mis-reconstructed gamma pairs.*

information from the two photons: $\vec{P}_{\pi^0} = \vec{P}_{\gamma_1} + \vec{P}_{\gamma_2}$. The distribution of the cosine of the angle between the π^0 direction and the beam direction is shown in Figure 5.2.6, while the π^0 momentum is shown in Figure 5.2.7.

The π^0 mass is reconstructed using equation 5.2.1.

$$M_{\pi^0} = \sqrt{2 \cdot E_{\gamma_1} \cdot E_{\gamma_2}(1 - cos(\theta_{12}))} \tag{5.2.1}$$

where θ_{12} is the opening angle between the two gammas (Fig. 5.2.5) and E_{γ_1} and E_{γ_2} are the gamma energies (Fig. 5.2.4). The reconstructed invariant mass of the neutral pions is shown in figure 5.2.8

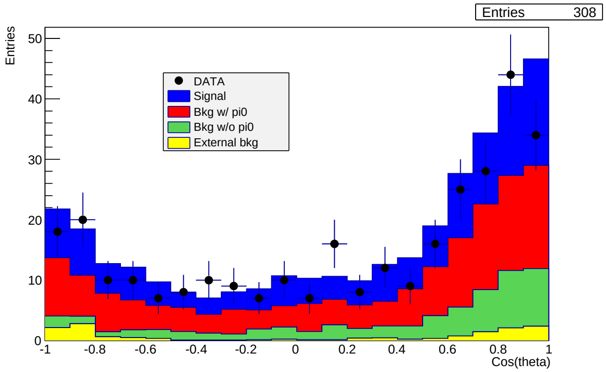

Figure 5.2.6: *Cosine of the angle of the reconstructed neutral pion with respect to the beam direction of selected CC-π^0 events for both DATA and MC.*

5.3 Fit Method.

Because of the difficulty to obtain a high purity sample for the $CC\pi^0$ events, the MC is fitted to the DATA in order to extract the background contribution to the sample. This fit is performed taking advantage of the differences in the distributions of signal, of background containing neutral pions and of background with no neutral pions.

Performing a fit to evaluate the signal and background components in the MC will lead to a cross section measurement that is both less MC-dependent as well as more accurate (with reduced systematic uncertainties).

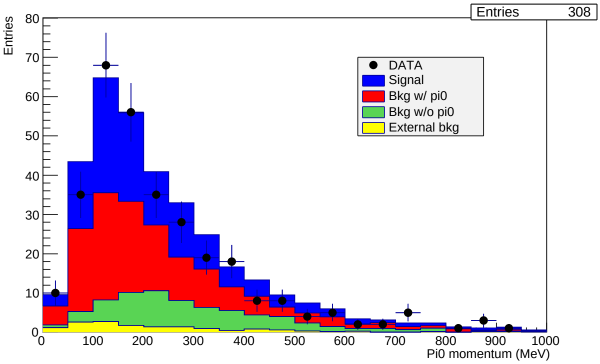

Figure 5.2.7: *Reconstructed momentum of the neutral pion of selected CC-π^0 events for both DATA and MC.*

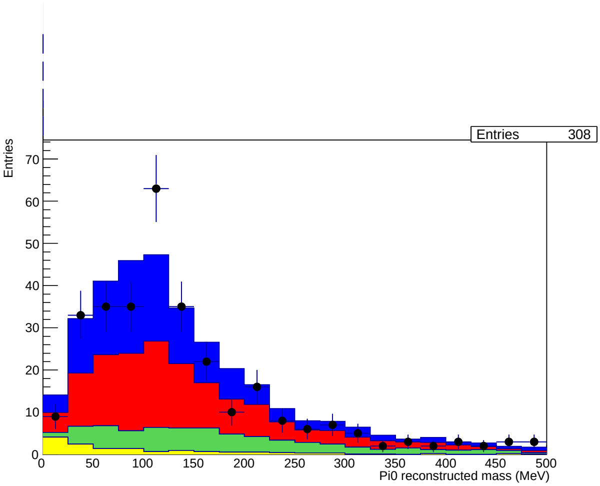

Figure 5.2.8: *Reconstructed invariant mass of the neutral pion of selected CC-π^0 events for both DATA and MC.*

The fit is performed through a χ^2 minimization. The χ^2 function to be minimized is shown in Equation 5.3.1. In the equation, P_k are fit parameters to renormalize the components of the MC and k accounts for the number of components in which the MC is broken.

The fit is performed simultaneously on two variables. On the reconstructed neutral pion mass, that separates the signal and background with neutral pions from the events that contain no π^0. And, at the same time, on the reconstructed distance between the event interaction vertex and the reconstructed position of the neutral pion (pion distance to the vertex, Fig. 5.3.1). This second observable separates the signal from background with π^0, that is, typically CC events that contain a neutral pion but this particle is produced outside the neutrino interaction nucleus. The χ^2 function in Eq. 5.3.1 is a sum over the bins of this 2-D fit.

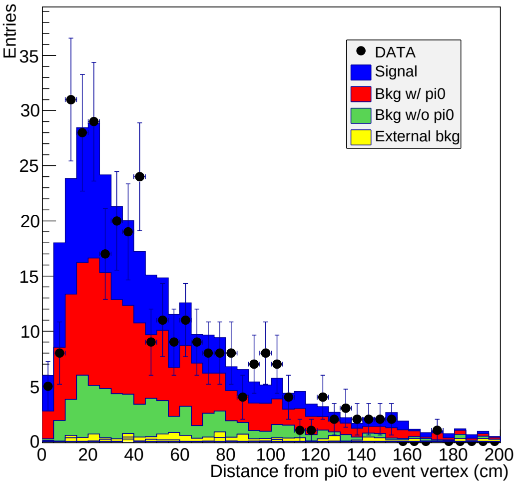

Figure 5.3.1: *Reconstructed distance between neutral pion and interaction vertex.*

$$\chi^2 = \sum_{bins} \left(\sum_k P_k \cdot N_{MC_k} - N_{DATA} + N_{DATA} \times log \left(\frac{\sum_k P_k \cdot N_{MC_k}}{N_{DATA}} \right) \right) \tag{5.3.1}$$

A binning study has been performed using the MC to extract the maximum information from the fit without introducing statistical noise. The choice of eight bins per variable has been found to be the optimal binning. No big changes in the fit error have been found by changing the bin boundaries during the study. The chosen binning for each of the 2-dimensional histogram variables are the following:

$$mass\ variable : \{0, 50, 100, 150, 200, 250, 350, 500, 2000\}\ \text{MeV} \tag{5.3.2}$$

$$distance\ variable : \{0, 10, 20, 30, 40, 50, 70, 100, 2200\}\ \text{cm} \tag{5.3.3}$$

To perform the fit, the MC is broken down in 6 categories, the signal contribution and five background contributions. Given that three of the background components are small, only the two main components are allowed to vary in the fit. The backgrounds in which the MC is broken are listed below:

- Background with π^0. Those are events that are not signal but a neutral pion is produced. $NC - \pi^0$ and $CC - \pi^0$ events with secondary neutral pions are among this background.
- Background without π^0. Those are events that do not contain a neutral pion in the final state.
- Cosmic ray contamination. Selected events produced by cosmic muons. The number of cosmic rays is evaluated using real data by measuring events outside the beam window trigger.
- MRD/EC events. Those events are neutrino interactions produced in the MRD or the EC. All those interactions are considered background even if there is neutral pion production.
- “Dirt” events. Those events are neutrino interactions produced in the walls of the detector hall. All those interactions are also considered background.

The background contributions that are allowed to vary in the fit are the background with π^0 and the background without π^0. Cosmic, MRD/EC and

“Dirt” backgrounds have a very small contribution and they are fixed in the fit. This background contribution can be quantified from figures in Sec. 5.2, where the three categories are grouped into the ”external backgrounds” category. The variables used for the fit can be seen in Figure 5.3.2. The Data and the MC samples allowed to vary are shown in the plot. The 1-D projections of the variables over which the 2-D fit is performed can be seen in Fig. 5.2.8 and 5.3.1.

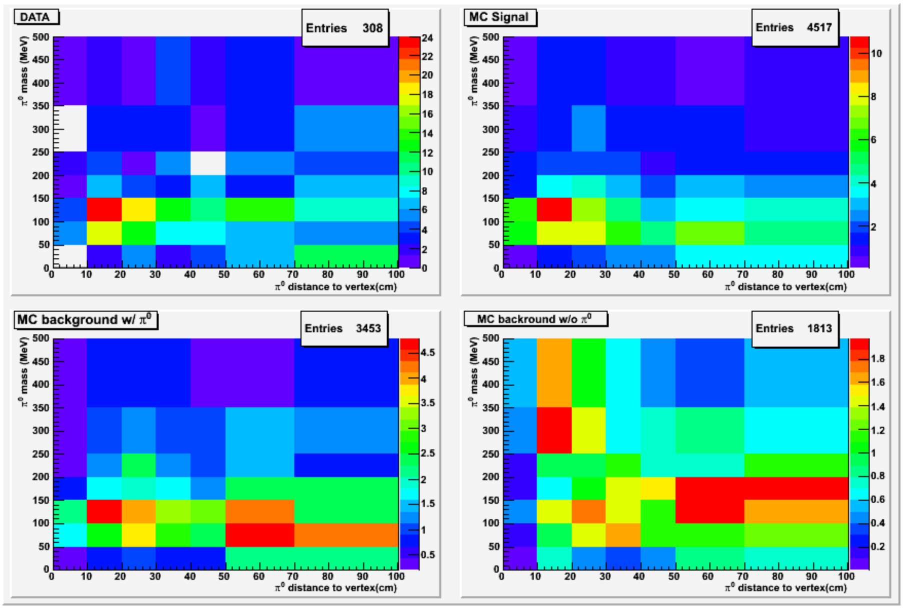

Figure 5.3.2: *Data and MC histograms used for the fit. Only the templates for the two MC contributions that are allowed to vary are shown.*

The detailed χ^2 function used for the fit is Eq. 5.3.4 in which the MC has been broken down into its different contributions and also includes the DATA/MC normalization constant Fn, explained below.

$$\chi^2 = \sum_{ij} \left(Fn \times N_{ij}^{MC} - N_{ij}^{DATA} + N_{ij}^{DATA} \times log \left(\frac{Fn \times N_{ij}^{MC}}{N_{ij}^{DATA}} \right) \right) \quad (5.3.4)$$

where N_{ij}^{MC} is defined as in Eq. 5.3.5

$$
\begin{aligned}
N_{ij}^{MC} \equiv P0 \cdot N_{ij}^{sig} + P1 \cdot N_{ij}^{bkgw\pi^0} + P2 \cdot N_{ij}^{bkgwo\pi^0} + \\
+ N_{ij}^{DIRT} + N_{ij}^{MRDEC} + N_{ij}^{COSMIC}
\end{aligned}
\tag{5.3.5}
$$

P0, P1 and P2 are the fit parameters that will be varied to minimize the χ^2 function. N^X are the number of events of data and the expected number of events for each category of the MC. Fn accounts for the DATA/MC normalization constant, it is extracted from the known POT of data ($0.99 \cdot 10^{20}$) and MC ($1.5 \cdot 10^8$).

The fit result is given in the Table 5.3.1.

Parameter	Best fit	1σ error
P0	0.96	0.28
P1	1.19	0.60
P2	0.20	0.50

Table 5.3.1: *Parameter values and errors for the fit.*

The value of the χ^2/dof is 1.29 for 64-3=61 dof. The covariance matrix is shown in the Table 5.3.2:

	P0	P1	P2
P0	1	-0.83	0.21
P1	-0.83	1	-0.65
P2	0.21	-0.65	1

Table 5.3.2: *Covariance matrix of the fit parameters.*

As shown in Tab. 5.3.1, the data overall normalization as well as the shape of the 2-dim distribution in (m_{π^0}, d_{μ,π^0}) space are essentially compatible with the signal and background yields predicted by the nominal MC. Also, the signal component is the one that can be extracted more precisely (with 30% fit uncertainty, see Tab. 5.3.1), despite being largely anti-correlated with the background with π^0 component (see Tab. 5.3.2).

Once the fit parameters are obtained, we can compare the DATA with the tuned MC. In the tuned MC, each MC component has been rescaled by the respective fit parameter. For example, in Fig. 5.3.3 DATA and the tuned

MC are compared for the distance between the π^0 production point and the interaction vertex and in Fig 5.3.4 DATA and the tuned MC are compared for the reconstructed neutral pion mass.

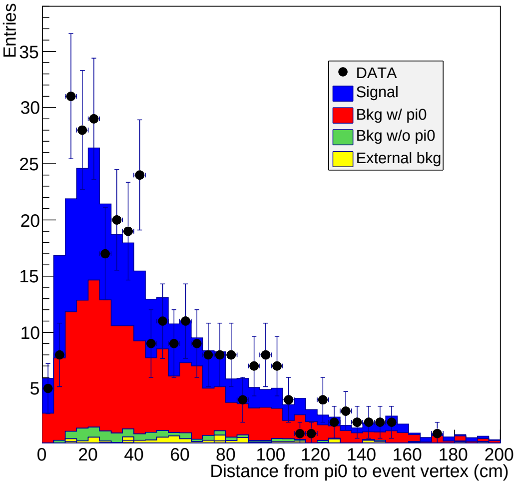

Figure 5.3.3: *Reconstructed distance between neutral pion and interaction vertex after fit. Because of detection resolution effects, also the signal contribution is expected to peak away from zero distance (see blue histogram).*

5.4 Fake data studies.

To check the robustness of the fit, fake data studies have been performed. Two checks have been performed in the fake data studies. A check in the response of the fit comparing MC with himself, and a check on the recovery of signal and background yields for a variety of signal/background strengths. All of the checks show a good response and the results are within expectation.

The first check has been performed preparing a fake data sample from the MC by adding a random Poisson variations in the bin contents of the MC histograms to simulate statistical uncertainties. A fit of the default MC over the fake data sample is performed. As it is expected, all the fit parameters are

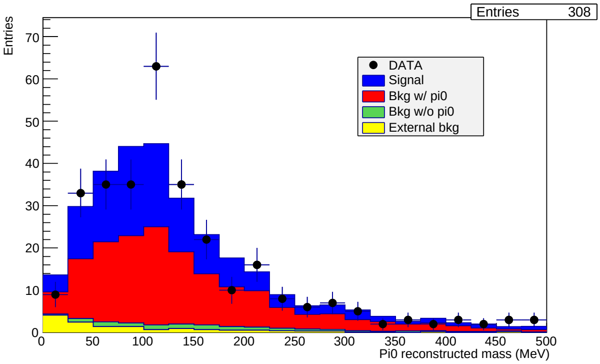

Figure 5.3.4: *Reconstructed invariant mass of the neutral pion of selected CC-π^0 events for both DATA and MC after the fit.*

consistent with 1, within the fit error.

The second robustness check is made preparing a fake data sample as in the first check and then manually increasing, one at a time, each of the contributions and thus, obtaining tree samples: One with increased signal, another one with increased background with π^0 and a third one with increased background without π^0. The process is repeated twice, for different contribution increments. In the first round, the contributions are increased by a factor of 2 and, in the second round, by a factor of 3. If the fit is robust the fit parameter associated to the changed contribution, either the signal or one of the backgrounds, should be increased in the same proportion.

The results of the second check are shown in Fig. 5.4.1. Each of the dots in the figure represent a different check. The black dots represent the signal fit parameter of the checks where the signal sample has been increased by the factor indicated on the x-axis leaving untouched the background samples. The fit parameters of the background that contains neutral pions and the one that contains no π^0s are represented The blue and green dots respectively when its corresponding contributions are increased.

Given these checks, all returning fit parameters within expectations, we conclude that our fit method is robust even against large MC mis-modelling of background yields.

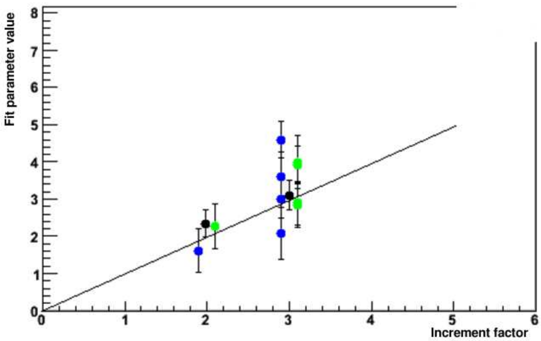

Figure 5.4.1: *Black dots represent the signal fit parameter when the signal sample is increased. Blue dots represent the background that contains neutral pions and green dots represent the background that contains no neutral pions.*

5.5 Absolute $CC - \pi^0$ cross section.

In this section, the extraction of the Muon Neutrino induced Charged Current Neutral Pion production cross section per nucleon will be explained. The cross section can be measured from the number of $CC - \pi^0$ events, the mass of the detector and the neutrino flux.

Two methods have been tested for the extraction of the number of signal events.

The first tested method relied on the background subtraction $N_{CC-\pi^0} = N_{CC-\pi^0(DATA)} - N_{CC-\pi^0(norm\ bkg)}$, where $N_{CC-\pi^0(DATA)}$ accounts for the number of detected events in the detector and $N_{CC-\pi^0(norm\ bkg)}$ accounts for the number of background events extracted mainly from the Monte-Carlo simulation. The Monte-Carlo simulation is normalized to the data using the number of total Charged Current events. The number of $CC - \pi^0$ is then corrected by the efficiency of the selection cuts ($\varepsilon_{CC-\pi^0(signal)}$) estimated with Monte-Carlo. To extract the CC-π^0 cross section with this method, Eq. 5.5.1 is used.

$$\sigma_{CC-\pi^0} = \frac{\frac{N_{CC-\pi^0(DATA)} - N_{CC-\pi^0(norm\ bkg)}}{\varepsilon_{CC-\pi^0(signal)}}}{\int\limits_{FV} \frac{d\Phi}{dE} dE \cdot N_{POT_{DATA}} \cdot N_N} \tag{5.5.1}$$

Where Φ is the neutrino flux crossing the Fiducial Volume (FV) of the detector, $N_{POT_{DATA}}$ is the number of DATA protons striking the production target, and N_N is the number of nucleons in the SciBar Fiducial Volume.

The second, which was finally chosen, is using the fit method. The Monte-Carlo simulation has been fitted to the experimental data in order to extract the number of signal events in the data sample. The fit method is explained in Section 5.3.

Once the Monte-Carlo is fitted to the data, the number of signal events is extracted from the number of Monte-Carlo signal events times the signal fit parameter (Par0) over the event selection efficiency as seen in the numerator of Equation 5.5.2.

$$\sigma_{CC-\pi^0} = \frac{\frac{Par0 \cdot N_{CC-\pi^0(signal)}}{\varepsilon_{CC-\pi^0(signal)}}}{\int\limits_{FV} \frac{d\Phi}{dE} dE \cdot N_{POT_{DATA}} \cdot N_N} \tag{5.5.2}$$

As explained for Eq. 5.5.1, Φ is the neutrino flux crossing the FV of the detector, $N_{POT_{DATA}}$ is the number of DATA protons striking the production target, and N_N is the number of nucleons in the SciBar Fiducial Volume.

The neutrino flux is estimated by using the Monte-Carlo. Only the flux crossing the detector FV with a neutrino energy greater than 370 MeV is taken into account. This energy threshold is set to the minimum neutrino energy needed to produce a neutral pion in the final state. The energy threshold has been estimated using the MC. In Figure 5.5.1 the neutrino energy signal events is shown.

The flux $d\Phi/dE$ in Eq. 5.5.2 is expressed per POT as seen in Equation 5.5.3. The number of DATA Protons On Target is measured with beam instrumentation as explained in Section 2.1

$$\int\limits_{FV} \frac{d\Phi}{dE} dE = \frac{Weight}{xsecWeight \cdot N_{POT_{MC}}} \tag{5.5.3}$$

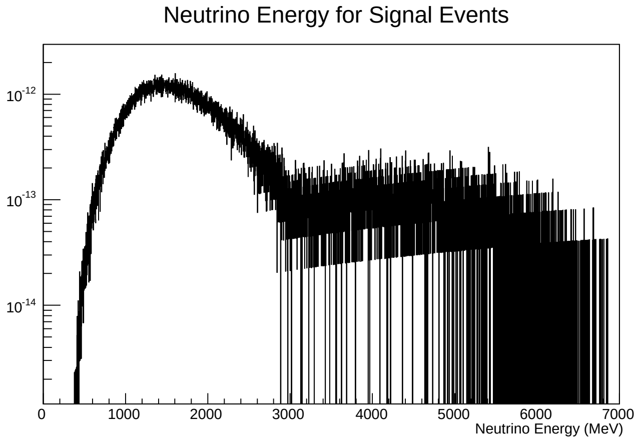

Figure 5.5.1: *Neutrino energy for MC events containing a neutral pion in the final state. The threshold for neutral pion production is 370 MeV according to the Monte-Carlo.*

For the number of Nucleons in the SciBar Fiducial Volume, we first calculate the number of CH molecules using the scintillator volume and density, then we multiply the number of CH by the number of nucleons in them:

$$N_{CH} = N_A \cdot \rho \cdot \frac{V}{A} = 4.70 \cdot 10^{29} \tag{5.5.4}$$

$$N_N = 13 \cdot N_{CH} = 6.11 \cdot 10^{29} \tag{5.5.5}$$

where $V = 260 \times 260 \times 59 \cdot 2.62 \times 0.9399$ cm^3, 59 is the number of SciBar layers in the SciBar Fiducial Volume, 2.62 cm is the SciBar layer thickness, $\rho = 1.032 g/cm^3$, $A = 13$ and $N_A = 6.02^{23}$. The factor 0.9399 in the volume accounts for the air gap between the detector scintillator bars.

The results of the fit method for the cross-section extraction are presented in Chapter 7. Before discussing the results, we discuss the systematic uncertainties affecting the cross-section measurement in Chapter 6.

Chapter 6

Systematic Error Evaluation.

In this section the sources of systematic errors that can affect the total cross section of ν_μ CC-π^0 interactions per nucleon in the SciBooNE CH target will be identified and evaluated . Equation 5.5.2, used to extract the neutrino induced CC_{π^0} cross section, can be investigated to find the possible sources of systematic errors.

The fit that has been used to extract the numerator of the equation 5.5.2 is the factor that can be affected by more systematic sources. The evaluated sources of systematic error affecting the fit result are: Detector systematics, Beam systematics and Neutrino interaction systematics.Those systematic sources can affect the fit either through the selection of the data sample (change in selection efficiency), or through the monte-carlo templates used to perform the fit and calculate the fit parameters.

In the denominator, the neutrino flux per POT (Φ) and the number of POT ($N_{POT_{DATA}}$) can be affected by the beam systematics only, and the number of nucleons (N_N) can be affected by the Detector response systematics.

Correlated changes in numerator and denominator of Eq. 5.5.2 due to the changes in a systematic parameter are properly taken into account. When a systematic affects both numerator and denominator, cancellations are possible and therefore only its effect on the ratio between the two is taken into account.

The systematic uncertainties have been evaluated using the monte-carlo simulation. Each systematic source has been evaluated modifying the default MC changing one parameter of the simulation each time. In this way we can account for how the uncertainty in the knowledge of a given parameter affects the final result. In order to quantify the effect of a systematic uncertainty, we compare the fit result of the varied MC with the fit result of the default MC.

To avoid the low DATA statistics to interfere with the fit result when measuring the systematics, the comparison is made between the fit result from the nominal MC over the expectation fit (MC_{CV}/MC_{CV}) and the fit result from the systematically varied MC over the expectation fit (MC_{syst}/MC_{CV}).

In this analysis, the MC is modified in two different ways:

- The re-weighting method is used to evaluate beam and neutrino interaction systematics. This method consists on changing the relative frequency of the events with respect to the nominal MC simulation. In this method, a large number (typically 100 or 1000) of fake data sets are generated. Each data set corresponds to a specific value of the varied systematic parameter, randomly generated within its error envelope. The effect of this randomly generated systematic variation is evaluated by assigning corresponding weights, event-by-event, to the entire event sample. The impact of the systematic parameter on the observable under study is quantified by the RMS spread introduced by the different fake data set throws. With this method we can change, among other quantities, the frequency of the neutrino interaction channels and the neutrino flux contents.
- Repeating the detector simulation from nominal NEUT event generator output with modified detector parameters. This method is used for the detector systematics. While the re-weighting method does not affect the way the events are reconstructed, changing the detector parameters affects the reconstruction. For the evaluation, only the differences above the fit error of the nominal MC over expectation fit (MC_{CV}/MC_{CV}) (which is $2.94{\cdot}10^{-41}$ cm$^2/N$, to be compared with a nominal MC $CC{-}\pi^0$ cross section of $5.86 \cdot 10^{-40}$ cm$^2/N$) are considered, given that smaller differences can be due to statistical fluctuations. Considering also those would therefore artificially inflate the systematic error budget.

A more detailed explanation of each method can be found in the following subsections.

6.1 Neutrino Beam Systematics.

In this section the systematic uncertainties that affect the neutrino flux are evaluated. The re-weighting method is used to evaluate the beam systematics. The sources of uncertainties affecting the neutrino beam are related to the proton delivery, the particle production (pion and kaon production), the hadronic interactions and the horn magnetic field [42]:

- Proton delivery: The systematic uncertainties over the measurement of the proton beam intensity and beam optics parameters affect the predicted Protons On Target and thus, the overall flux normalization. The neutrino flux uncertainties due to proton delivery are 2% from the proton beam intensity and 1% from the proton beam optics. This systematic source is negligible compared to the other beam systematic sources.

- Particle production: The uncertainties in the production of the pions and kaons affect the neutrino beam composition and energy spectrum. The uncertainty coming from each of the $\pi^{\pm}$ and $K^{+/0}$ particles is measured separately. The π^{+} production has been evaluated using HARP π^{+} double differential cross section data. For the π^{-} and K^{0} production the Sanford-Wang model parametrization is used, and the Feynman scaling model is used for the K^{+} production. Using the model error, random variations of the model parameter are produced. The systematic errors are extracted by processing these systematic variations of each model.

- Horn magnetic field and Hadronic interactions in the target or horn: The hadronic interactions uncertainties (other than particle production) take into account the total hadronic cross section and the inelastic and quasi-elastic cross sections for nucleons in beryllium and aluminum. The horn magnetic field systematics includes ±1 kA uncertainty in the horn current and the uncertainty on the skin depth effect (see Sec. 3.1).

Systematic variations around the central value of each uncertainty source parameter are processed and a fit is performed for each variation. The systematic variation for each source is of an amplitude of the source uncertainty. Given that the variations affect not only the final composition of the selected sample but also the cross section of the different interaction channels, the evaluation of the beam systematics is done over the product of the cross-section ($\sigma_{CC\pi^0}$ in Eq. 5.5.2 with P0=1) times the signal fit parameter (P0 in Eq. 5.5.2). The resulting product is stored in a histogram, one entry per fake data set throw. As explained above, the RMS spread associated with the fake data set variations defines the systematic uncertainty on the extracted CC-pi0 cross section. A summary of the effect of beam systematic uncertainties on the CC-pi0 cross section extraction is given in Tab. 6.1.1

	$\Delta\sigma(cm^2/N)$
π^+ production	$2.58 \cdot 10^{-41}$
π^- production	$8.93 \cdot 10^{-43}$
K^+ production	$3.73 \cdot 10^{-41}$
K^0 production	$1.79 \cdot 10^{-43}$
Horn magnetic field + Hadronic Int.	$6.08 \cdot 10^{-41}$

Table 6.1.1: *Summary of beam systematic uncertainties on the CC-pi0 cross section extraction. Among the contributions, the skin depth effect in the "Horn magnetic field + Hadronic interactions" category is the dominant one at the energies relevant for this analysis.*

6.2 Neutrino Interaction Systematics.

The Neutrino Interaction uncertainty evaluation has been done using the re-weighting method as well. For simplicity, we rely on the readily-available parametrization from an alternative event generator (NUANCE, [31]) to generate a systematically varied NEUT. In this case, the re-weighting is performed by obtaining a NUANCE-based ratio ($NUANCE_{syst}/NUANCE_{CV}$) and applying it as a re-weighting factor to the $NEUT_{CV}$.

The parameter uncertainties that have been evaluated are the axial mass (M_A) for CC-QE, CC-coherent, 1 pion production and multi-pion production interactions, the nuclear Fermi Momentum (p_F), the nucleon Binding Energy (E_B) and the NC isoscalar axial-vector contribution (Δs). The value of the parameters are shown in Tab. 6.2.1 together with the parameter uncertainties assumed.

All those parameters except $M_{A_{1\pi}}$ and $M_{A_{Multi-\pi}}$ have a negligible contribution to the Neutrino Interaction systematics as can be seen on Tab. 6.2.2.

6.3 Detector Systematics.

Detector response systematic uncertainties have been evaluated by generating a set of new monte-carlo simulations. For each of the simulations, one of the detector properties has been varied using the knowledge we have of the detector. Each one of the evaluated detector properties affects the event reconstruction in a different way. Detector response parameters can affect the track finding efficiency, the particle identification or the energy reconstruction,

Parameter	Value
$M_{A_{CCQE}}$	1.21 ± 0.22 GeV/c^2
$M_{A_{coh}}$	1.0 ± 0.28 GeV/c^2
$M_{A_{1\pi}}$	1.21 ± 0.28 GeV/c^2
$M_{A_{multi-\pi}}$	1.30 ± 0.52 GeV/c^2
p_F	217 ± 30 MeV/c
E_B	25 ± 9 MeV/c
ΔS	0.0 ± 0.1

Table 6.2.1: *Parameters being evaluated in the Neutrino Interaction systematics.*

	$\Delta\sigma(cm^2/N)$
$M_{A_{(ccqe)}}$	$1.76 \cdot 10^{-42}$
$M_{A_{(coh)}}$	$2.64 \cdot 10^{-45}$
$M_{A_{(1\pi)}}$	$4.62 \cdot 10^{-41}$
$M_{A_{(multi-\pi)}}$	$1.50 \cdot 10^{-41}$
p_F	$4.92 \cdot 10^{-43}$
E_B	$2.63 \cdot 10^{-43}$
Δs	$6.00 \cdot 10^{-44}$

Table 6.2.2: *Summary of the effect of neutrino interaction systematic uncertainties on the CC-π^0 cross section extraction.*

among other quantities.

The detector properties that have been evaluated are the xtalk in the in the SciBar MA-PMT, the Birk's constant of the SciBar scintillator, the SciBar hit threshold, the SciBar PMT charge resolution and the SciBar TDC dead time. The way to estimate the systematic error consists on redoing the event selection using those new samples and measuring the difference between the final result with respect to the default monte-carlo.

- The cross talk systematic accounts for the uncertainty on the amount of light transferred across the fibers to their neighbors in the MA-PMT's. Nominally, the transferred light follows the scheme shown in Fig. 4.1.4. For the adjacent channels the transmitted light is 3.15 ± 0.4%. The systematic variation applied for the cross talk is $\pm 1\sigma$. The xtalk affects the track reconstruction by increasing the noise around the tracks.

- Birk's constant accounts for the scintillator quenching. The amount of light produced in the scintillators is not directly proportional to the energy deposited by the detected particle. The light produced by the scintillator follows the Birk's law. The Birk's constant measured in the SciBar scintillators is 0.0208 ± 0.0023 cm/MeV and a 1σ variation has been applied to evaluate this systematic. The Birk's constant affects the energy reconstruction.

- Hit threshold accounts for the number of detected photo-electrons in a single SciBar channel necessary to reconstruct a hit. A hit is a base element in the track reconstruction process and indicates a bar crossed by the particle. The threshold is set at 2 photo-electrons. On the other hand, the conversion constant from photo-electrons to deposited energy has been measured channel by channel using cosmic-ray muons and a channel-by-channel variation of ±20% has been found. Thus a ±20% variation to the hit threshold (±0.4 *p.e.*) is applied. This systematic affects the track finding efficiency and the energy reconstruction.

- The PMT resolution of a single photo-electron in the SciBar detector has been set in the monte-carlo simulation to be 50%. This value reproduces correctly the dE/dx measured from cosmic-ray muons. On the other hand, a 70% resolution for a single photo-electron has been measured in the laboratory. A ±20% variation on the PMT resolution has been applied to evaluate this systematic to cover this difference.

- The SciBar TDC dead time is set to 55 ns in the simulation with ±20 ns uncertainty [59]. A 1σ variation has been applied to evaluate this systematic.

As seen in Tab. 6.3.1, the only contributions to the systematic uncertainty that are larger than the MC statistical error ($2.94 \cdot 10^{-41}$ cm^2/N) come from the hit threshold and the TDC dead time.

6.4 Result of total cross section error evaluation.

Table 6.4.1 shows the summary of the systematic error evaluation affecting the total $CC - \pi^0$ cross section. The "Fit" row corresponds to the 30%

		Fit parameter	$\sigma\times$FitPar	$\Delta\sigma(cm^2/N)$
xtalk	upper	0.994719	$5.83\cdot10^{-40}$	$-3.10\cdot10^{-42}$
	lower	1.00369	$5.88\cdot10^{-40}$	$2.16\cdot10^{-42}$
birk	upper	1.04332	$6.12\cdot10^{-40}$	$2.54\cdot10^{-41}$
	lower	0.964142	$5.65\cdot10^{-40}$	$-2.10\cdot10^{-41}$
hitthresh	upper	0.967205	$5.67\cdot10^{-40}$	$-1.92\cdot10^{-41}$
	lower	0.892164	$5.23\cdot10^{-40}$	$\mathbf{-6.32\cdot10^{-41}}$
pmtres	upper	1.0259	$6.01\cdot10^{-40}$	$1.52\cdot10^{-41}$
	lower	1.02963	$6.04\cdot10^{-40}$	$1.74\cdot10^{-41}$
tdcdead	upper	0.945107	$5.54\cdot10^{-40}$	$\mathbf{-3.22\cdot10^{-41}}$
	lower	0.945534	$5.54\cdot10^{-40}$	$-3.19\cdot10^{-41}$

Table 6.3.1: *Summary of the effect of detector systematic uncertainties on the CC-pi0 cross section extraction. The only contributions that are larger than the MC statistical fluctuations come from hit threshold lower and TDC dead time upper variations.*

fit uncertainty discussed in Sec. 5.3. The ”Beam”, ”NuInt” and ”Detector” rows correspond to the systematic uncertainties discussed in Secs. 6.1- 6.3, respectively.

Source	$\Delta\sigma(\cdot10^{-40})(cm^2/N)$
Fit	± 1.9
Beam	± 0.7
NuInt	± 0.5
Detector	-0.7
Total	**+2.1 -2.2**

Table 6.4.1: *Summary of total cross section systematic error evaluation.*

As can be seen in Tab. 6.4.1, the dominant error affecting the total cross section result is the fit error.

6.5 Systematic uncertainty evaluation on kinematic distributions.

The systematic errors can also affect the shape of the kinematic reconstructed quantities. Because of that, a study of systematic errors over the kinematic variables has been also performed. The following plots shows the total MC with the associated systematic errors. Also the plots with the relative contribution of systematic errors for each variable are shown.

Given that no background subtraction is performed in the kinematics plots presented in this section, the fit is not re-evaluated for each systematic variation in this case. The methodology to obtain the systematic errors on the kinematic plots is to make a comparison bin-by-bin of the central value plot against each of the systematically varied plot. This comparison is made with the nominal post-fit kinematic distributions. The systematic errors in this section are assumed to be symmetric in order to reduce statistical fluctuations in the bin-by-bin systematic measurement.

The systematic uncertainties affecting the distributions of muon momentum (Figs. 6.5.1 and 6.5.2), muon angle (Figs. 6.5.3 and 6.5.4), pi0 momentum (Figs. 6.5.5 and 6.5.6), pi0 angle (Figs. 6.5.7 and 6.5.8) and pi0 invariant mass (Figs. 6.5.9 and 6.5.10) are shown below. The bin-by-bin systematic uncertainties are typically of order 20-30% for all observables, with similar contributions from beam, neutrino interaction, and detector response systematic error sources.

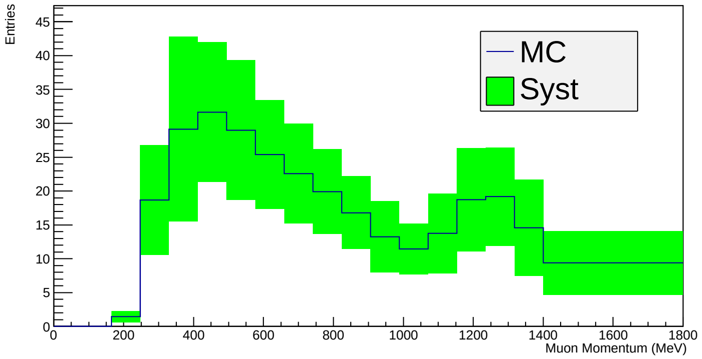

Figure 6.5.1: *Muon momentum MC distribution with systematic errors. Notice that the last bin is an overflow bin.*

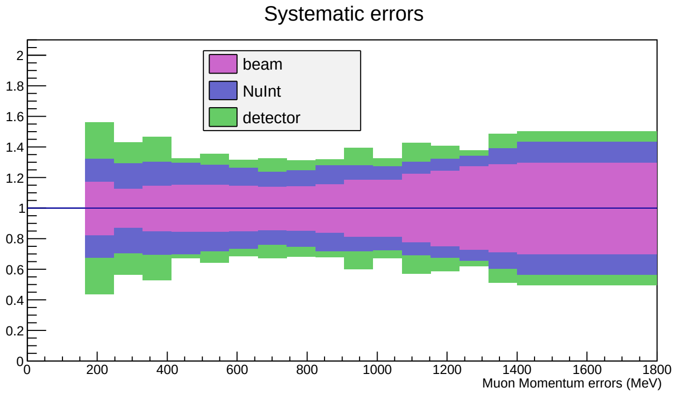

Figure 6.5.2: *Relative contributions to the systematic errors for the muon momentum.*

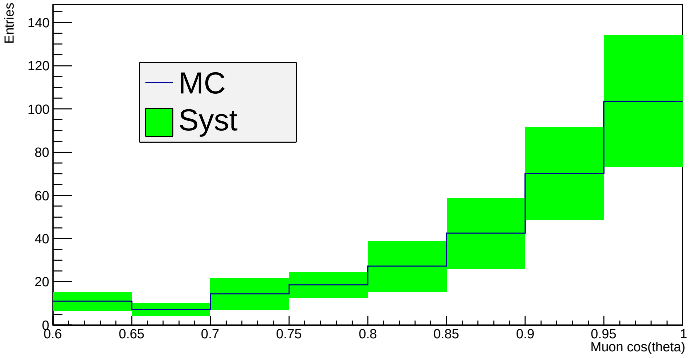

Figure 6.5.3: *Muon angle with respect to the beam direction MC distribution with systematic errors. Notice that the first bin is an underflow bin.*

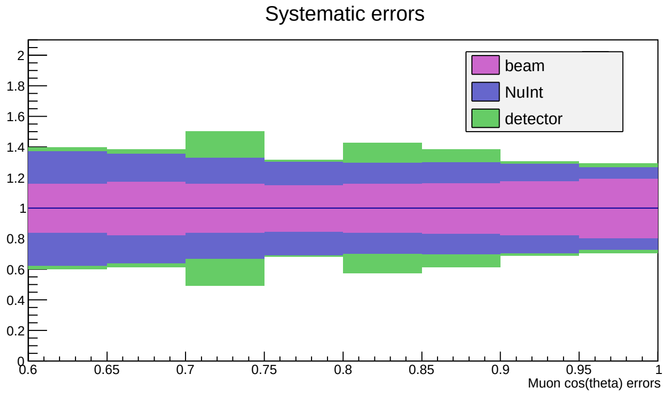

Figure 6.5.4: *Relative contributions to the systematic errors for the muon angle with respect to the beam direction.*

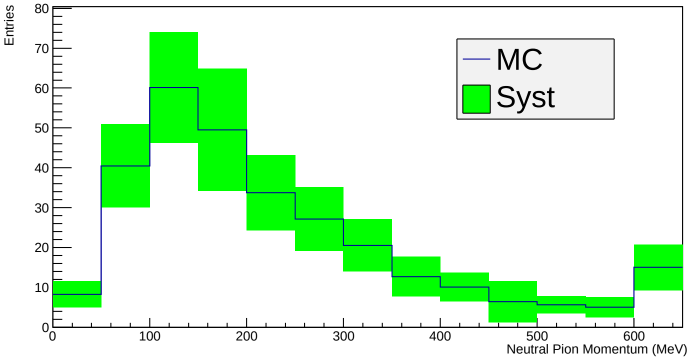

Figure 6.5.5: *Neutral pion momentum MC distribution with systematic errors. Notice that the last bin is an overflow bin.*

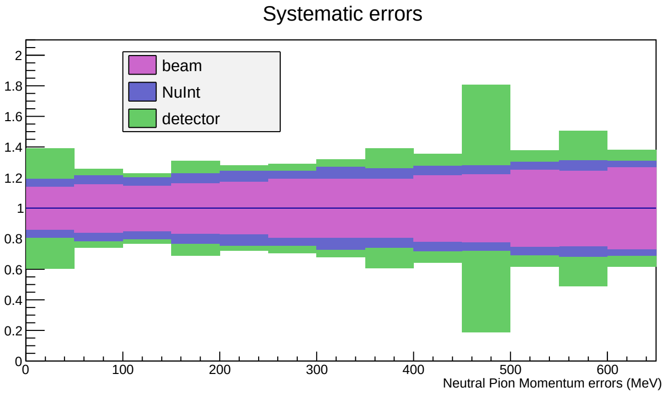

Figure 6.5.6: *Relative contributions to the systematic errors for the* π^0 *momentum.*

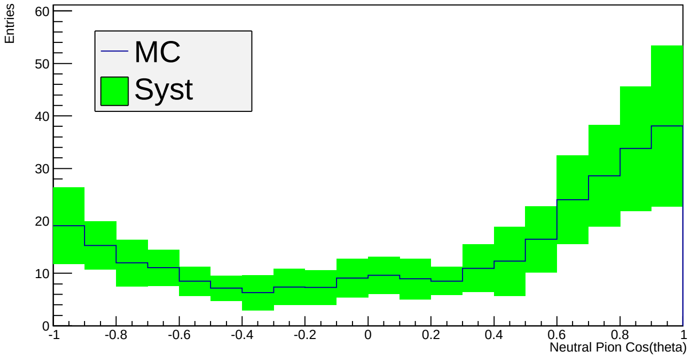

Figure 6.5.7: *MC of the neutral pion cosine of the angle with respect to the beam direction with systematic errors.*

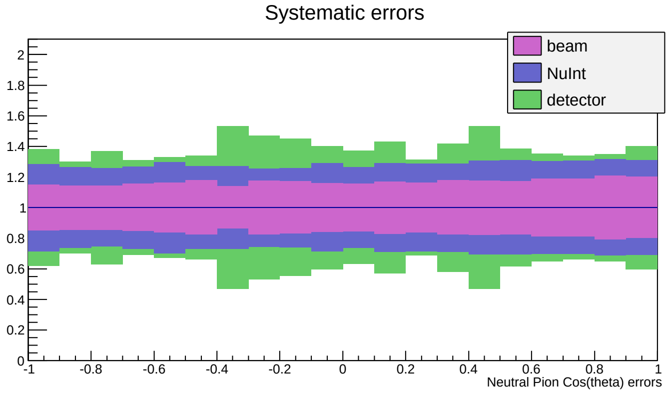

Figure 6.5.8: *Relative contributions to the systematic errors for the neutral pion cosine of the angle with respect to the beam direction.*

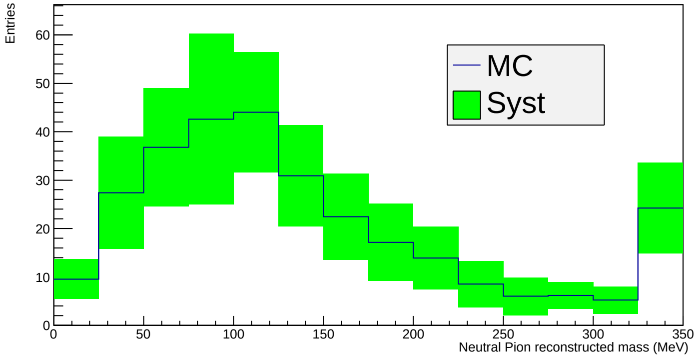

Figure 6.5.9: *Neutral pion reconstructed mass MC with systematic errors. Notice that the last bin is an overflow bin.*

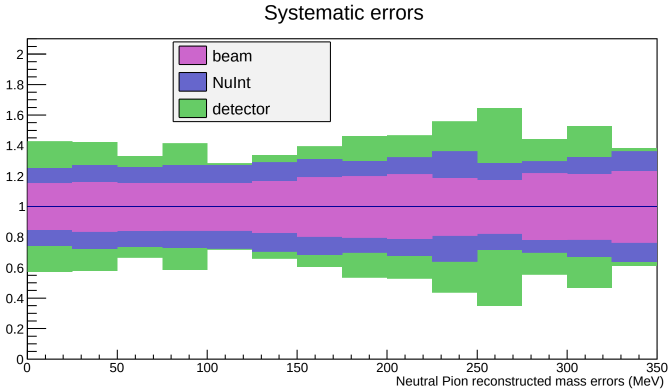

Figure 6.5.10: *Relative contributions to the systematic errors for the neutral pion reconstructed mass.*

Chapter 7

CC-π^0 analysis results

In this section, analysis results are presented. Sec. 7.1 discusses the flux-averaged CC-π^0 production cross section measured with SciBooNE, comparing it to NEUT MC expectations and earlier MiniBooNE results. A discussion on how well the NEUT simulation is expected to reproduce the energy dependence of the CC-π^0 cross section based on SciBooNE and MiniBooNE data is given in Sec. 7.2. Sec. 7.3 gives details of the production kinematics measured for the muon and π^0 candidates, again comparing to expectations. Finally, Sec. 7.4 gives an outlook of upcoming CC-π^0 results in other experiments.

7.1 Flux-averaged cross section

The neutrino-induced CC-π^0 cross section result obtained in the present analysis, taking into account all the considered errors, is shown in Eq. 7.1.1:

$$\langle\sigma_{\mathrm{CC}-\pi^0}\rangle_\phi = (5.6 \pm 1.9_{\mathrm{fit}} \pm 0.7_{\mathrm{beam}} \pm 0.5_{\mathrm{int}} - 0.7_{\mathrm{det}}) \times 10^{-40}\ \mathrm{cm}^2/\mathrm{N} \quad (7.1.1)$$

at an average muon neutrino energy of 0.89 GeV. This average energy is estimated from the MC simulation as the flux-averaged neutrino energy (see Fig. 3.1.2) above CC-π^0 production threshold (about 370 MeV, see Fig. 5.5.1).

This result can be quantitatively compared with the CC-π^0 cross section result of the MiniBooNE experiment [32], see Tab. 7.1.1. The comparison is straightforward given that the beam, nuclear target and the signal definition are essentially the same for both experiments. Concerning the beam, both experiments are exposed to the on-axis portion of the BNB neutrino flux, resulting in very similar flux-averaged neutrino energies in Tab. 7.1.1. The

Experiment or Simulation	$\langle\sigma_{\mathrm{CC}-\pi^0}\rangle_\phi$ (10^{-40} cm^2/N)	$\langle E_\nu\rangle_\phi$ (GeV)
SciBooNE	$5.6^{+2.1}_{-2.2}$	0.89
MiniBooNE	6.6 ± 1.1	0.97
NEUT	5.8	0.89

Table 7.1.1: *Comparison of the flux-averaged CC-π^0 production cross section $\langle\sigma_{\mathrm{CC}-\pi^0}\rangle_\phi$ measured in SciBooNE (this analysis), with NEUT-based [47] expectations and with MiniBooNE results [32]. The table also gives the flux-averaged neutrino energy $\langle E_\nu\rangle_\phi$ for each measurement/expectation.*

nuclear target is essentially CH for SciBooNE, while it can be approximated with CH_2 for MiniBooNE, hence very similar. Both SciBooNE and MiniBooNE adopt an "observable" signal definition, defined in terms of particles exiting the target nucleus. In the MiniBooNE case, the signal is defined as a μ^- and a single π^0 exiting the target nucleus, with any number of nucleons, and with no additional final state mesons. The SciBooNE signal definition adopted here is identical, except for the requirement that additional mesons other than π^0's are also allowed. The SciBooNE signal definition is therefore slightly more inclusive, considering $(\mu^-, \pi^0, \pi^\pm)$ final states as signal. According to NEUT simulations, the difference between the two signal definitions is very small at SciBooNE/MiniBooNE neutrino energies, as can be appreciated in Fig. 7.1.1.

As can be seen in Tab. 7.1.1, the MiniBooNE and SciBooNE cross section results are consistent with each other. This agreement increases our confidence in both results, given the differences between the two detectors. In particular, MiniBooNE has the advantage of having more statistics, allowing to perform an energy-binned cross section measurement (see Secs. 1.4 and 7.2), while SciBooNE has only one measurement point. On the other hand, the SciBooNE measurement has the advantage of relying on a completely different, and more detailed, event reconstruction. Compared to MiniBooNE, the different detector technology provides therefore an independent and possibly more trustworthy way to understand the overall CC-π^0 cross section normalization, providing an "anchor point" for the MiniBooNE energy-binned measurement. As discussed in Sec. 1.4, the SciBooNE cross section measurement cannot be directly compared with experiments other than MiniBooNE due to different signal definitions and/or nuclear targets.

Table 7.1.1 also compares the SciBooNE cross section with the NEUT

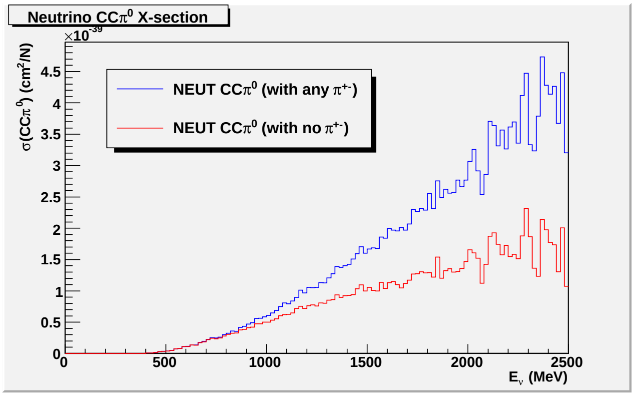

Figure 7.1.1: *NEUT expectations for the CC-*π^0 *production cross section as a function of neutrino energy for both the SciBooNE and MiniBooNE signal definitions (see text for details). The two cross sections are expected to be very similar in the SciBooNE/MiniBooNE energy range.*

expectation. A good agreement is found also in this case. Therefore, the NEUT modelling of π^0-producing resonant and DIS neutrino interactions on carbon, and the NEUT treatment of pion intra-nuclear interactions, appear adequate at SciBooNE energies.

7.2 Cross section energy dependence

In addition to the NEUT overall cross section normalization, also the NEUT cross section energy dependence can be contrasted with measurements from MiniBooNE and SciBooNE. MiniBooNE measured the CC-π^0 production cross section as a function of neutrino energy in the $0.5 < E_\nu < 2.0$ GeV range. The neutrino energy can be reconstructed from the measured μ^- and π^0 kinematics, assuming that the signal events are from the reaction $\nu_\mu n \to \mu^- \pi^0 p$, that the neutron target is at rest, and that the incoming neutrino is traveling along the beam direction. The neutrino energy resolution is expected to be 11%. The cross section measured as a function of reconstructed neutrino energy bins is then unfolded back to 0.1 GeV wide bins of true neutrino energy[1], using a

---

[1] Except for the $1.8 < E_\nu < 2.0$ GeV range, where the cross section is reported in a single 0.2 GeV wide bin.

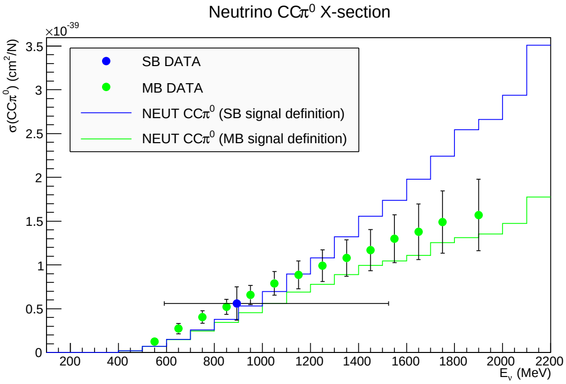

Figure 7.2.1: *CC-π^0 production cross section as a function of neutrino energy as measured by MiniBooNE [32] and as simulated by NEUT [47] for both MiniBooNE and SciBooNE signal definitions. For comparison, the flux-averaged cross section measured by SciBooNE (this analysis) is also shown at $\langle E_\nu \rangle = 0.89$ GeV. The SciBooNE vertical error bars include both fit and systematic uncertainties, while the horizontal error bars represent the asymmetric RMS spread in the expected neutrino flux energy distribution (see Fig.3.1.1) above CC-π^0 production threshold (about 370 MeV neutrino energy).*

response matrix coonstructed from the Monte-Carlo simulation. As shown in Fig. 7.2.1, despite the fact that NEUT seems to slightly underestimate the cross section as measured by MiniBooNE (as already shown in Tab. 7.1.1), the shape of the MiniBooNE energy dependence is accurately reproduced by NEUT.

SciBooNE data can also provide some insight on the accuracy of the NEUT CC-π^0 cross section energy dependence. While SciBooNE does not have enough event statistics to produce an energy-binned cross section measurement as MiniBooNE did, some information can be obtained by comparing the reconstructed neutrino energy spectra of all (signal plus background) CC-π^0 candidates as measured by SciBooNE and as predicted by the NEUT Monte-Carlo simulation. The neutrino energy is reconstructed by using the same assumptions and the same observables as in the MiniBooNE case:

$$E_\nu^{rec} = \frac{m_p^2 - m_n^2 - m_X^2 + 2m_n E_X}{2(m_n - E_X + |\vec{p}_X|\cos(\theta_{\nu X}))} \tag{7.2.1}$$

where $p_X \equiv p_\mu + p_{\gamma 1} + p_{\gamma 2}$ is the four-momentum of a composite, fictitious, particle representing the muon plus π^0 final state system, and $\theta_{\nu X}$ is the angle between the direction of such "particle" and the incoming neutrino direction. In order to more accurately reconstruct the muon momentum and therefore the neutrino energy, the SciBooNE CC-π^0 sub-sample corresponding to MRD-stopped muon events only has been used. This sample corresponds to 231 out of 308 data events.

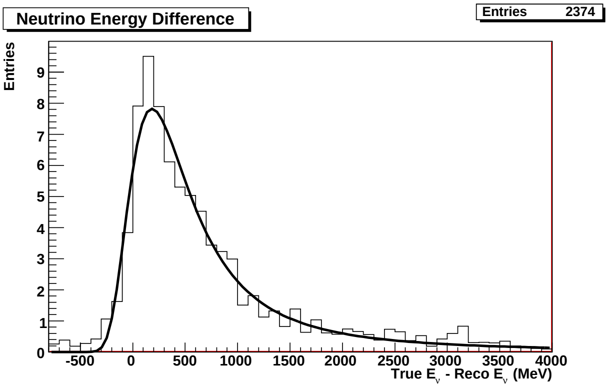

Figure 7.2.2: *Difference between the neutrino "true" energy and the reconstructed energy (true - reco) for CC-π^0 selected Monte Carlo signal events in the MRD-stopped sample.*

A Monte-Carlo study to quantify the accuracy of the neutrino energy reconstruction as defined in Eq. 7.2.1 for selected CC-π^0 signal events in the MRD-stopped sample has been performed, and the results shown in Figs. 7.2.2 and 7.2.3. According to this study, the reconstruction introduces a significant bias and smearing. The neutrino energy is underestimated by about 200 MeV on average, and the neutrino energy resolution is of order 20%. Nevertheless, the neutrino energy measurement is clearly correlated with the actual neutrino energy (see Fig. 7.2.3), and therefore provides some information on the cross section neutrino energy dependence.

The SciBooNE DATA/MC comparison of the reconstructed neutrino energy for the MRD-stopped CC-π^0 sample is shown in Fig. 7.2.4. In this figure, the MC contributions have been renormalized according to the fit parameters given in Tab. 5.3.1, extracted from the more inclusive MRD-matched sample fit. Despite a small data excess in the MRD-stopped sample, we can see

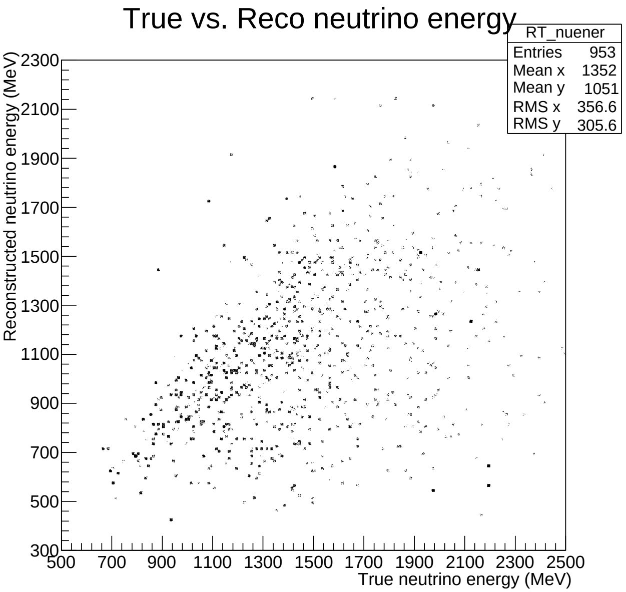

Figure 7.2.3: *True versus reconstructed neutrino energy for CC-π^0 selected Monte Carlo signal events in the MRD-stopped sample. Notice the different scale ranges for the reconstructed and the true energies.*

in Fig. 7.2.4 that the NEUT-based Monte Carlo reproduces well the shape of the reconstructed neutrino energy measured by SciBooNE. In summary, the NEUT modelling of the CC-π^0 cross section energy dependence has been experimentally verified by both SciBooNE and (especially) MiniBooNE data.

7.3 Particle production kinematics

SciBooNE data allows us to study not only the total cross section of muon neutrino CC-π^0 interactions on a CH target, but also the production kinematics of the final state muon and π^0 candidates. These distributions can be compared with the NEUT expectations, for a more detailed evaluation of how well NEUT describes CC-π^0 processes. For the comparison, we rescale the Monte-Carlo contributions according to the results of the fit in the (pion

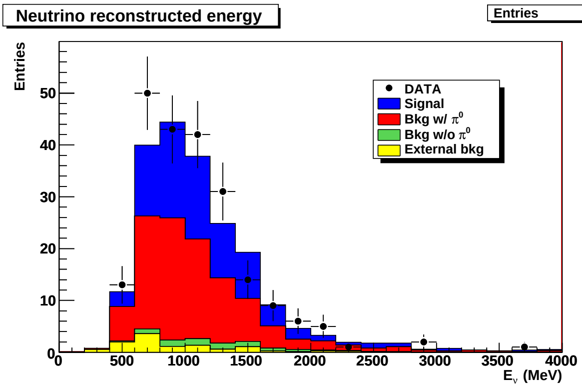

Figure 7.2.4: *Reconstructed neutrino energy for the MRD-stopped CC-*π^0 *sample for DATA and MC.*

mass, muon-to-pion distance) reconstructed variables (Tab. 5.3.1). The main effect of this Monte-Carlo tuning is to decrease the expected contribution from backgrounds without π^0's. If our fit model provides a good description of the data, we expect to maintain a good DATA/MC agreement in the kinematic distributions that were adequately described already before the fit, and to improve the MC description where DATA/MC discrepancies were present.

Figures 7.3.1 and 7.3.2 show the DATA/MC comparison for the muon candidate kinematics, in terms of muon momentum as well as angle between the muon and the beam direction, respectively. The DATA/MC agreement is generally good, except perhaps some MC excess in the muon forward direction. As can be seen by comparing Fig. 5.2.3 with Fig. 7.3.2, the disagreement in the muon forward direction is reduced with the post-fit Monte-Carlo.

The same distributions (particle momentum and direction with respect to the beam) are shown in Figs. 7.3.3 and 7.3.4 for the π^0 candidate as well. Before the fit, the nominal Monte-Carlo simulation tends to predict a slightly harder π^0 momentum distribution (see Fig. 5.2.7), as well as a slight MC excess in the π^0 candidate forward direction (see Fig. 5.2.6). The reduction of the background without π^0 component preferred by the fit, which is concentrating in the high momentum, forward direction region, helps in improving the DATA/MC agreement also in this case, as shown in Figs. 7.3.3 and 7.3.4.

While not strictly related to particle production kinematics, we show in Fig. 7.3.5 also the post-fit DATA/MC comparison for the π^0 candidate re-

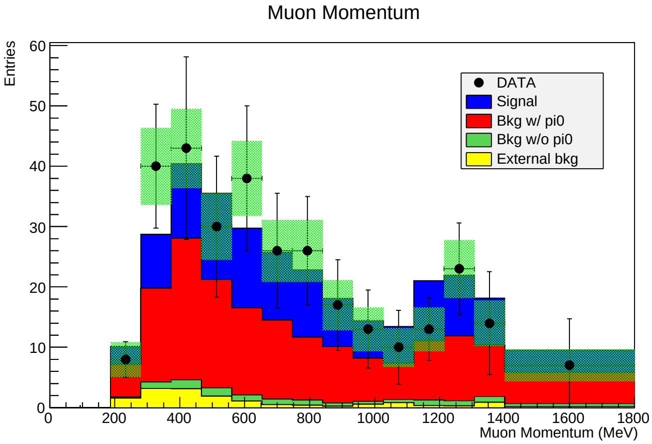

Figure 7.3.1: *Muon candidate momentum after the fit for both DATA and MC, for selected CC-π^0 events in the MRD-matched sample. The DATA statistical errors are shown with green boxes, while the black error bars give the total (statistical plus systematic) uncertainties.*

constructed mass. Compared to the pre-fit comparison in Fig. 5.2.8, the DATA/MC comparison appears satisfactory in both cases, with a slight improvement in the post-fit case in the high mass (>150 MeV/c^2) region.

Overall, our fit methodology is satisfactory also in the sense that it maintains or improves DATA/MC agreement in all distributions studied, including the particle production kinematic distributions that are not used in the fit. Therefore, we can conclude that the nominal NEUT simulation provides a fair description of SciBooNE CC-π^0 data kinematic distributions, and that this description can be further improved by a simple renormalization of the various signal and background components.

A final note on the largest background contribution, that is the background with π^0's. As can be seen in Figs. 7.3.1-7.3.5, the shapes of the signal and of the background with π^0 components are very similar in all distributions. Therefore, it appears difficult to isolate the two components from each other, beyond what already accomplished via the muon-to-pion distance observable exploited in the fit (see Fig. 5.3.1).

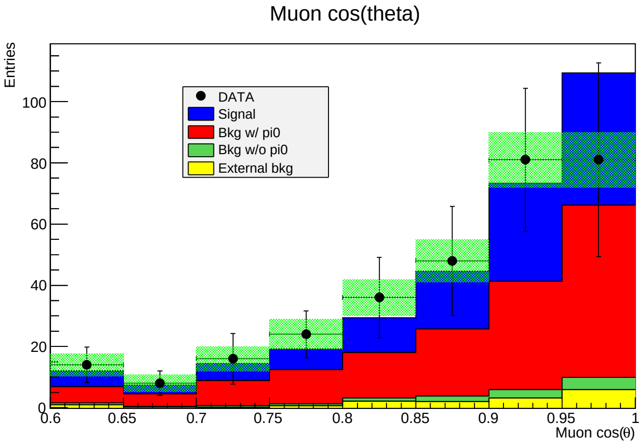

Figure 7.3.2: *Cosine of the angle between the muon candidate direction and the beam direction after the fit for both DATA and MC, for selected CC-*π^0 *events in the MRD-matched sample. The DATA statistical errors are shown with green boxes, while the black error bars give the total (statistical plus systematic) uncertainties.*

7.4 Other upcoming experimental results

For completeness, we conclude this chapter with a brief outlook of upcoming experimental results on charged-current π^0 production with experiments other than SciBooNE. New results by the currently operating neutrino experiments MINERvA (USA) and T2K (Japan) are expected soon.

The MINERvA experiment is designed to perform precision studies of neutrino-nucleus scattering using ν_μ and $\bar{\nu}_\mu$ neutrinos incident at 1-20 GeV in the NuMI beam at Fermilab (USA). The detector is comprised of a finely-segmented scintillator-based inner tracking region surrounded by electromagnetic and hadronic sampling calorimetry. By placing MINERvA immediately upstream of the MINOS near detector, a neutrino detector composed of magnetized iron plates interleaved with scintillator planes, charge and momentum measurements of forward-going muons can be made. The experiment started taking data in neutrino mode in March 2010, and switched to antineutrino mode in November 2010. Preliminary results for $\bar{\nu}_\mu$-induced CCπ^0 interactions were presented in [71].

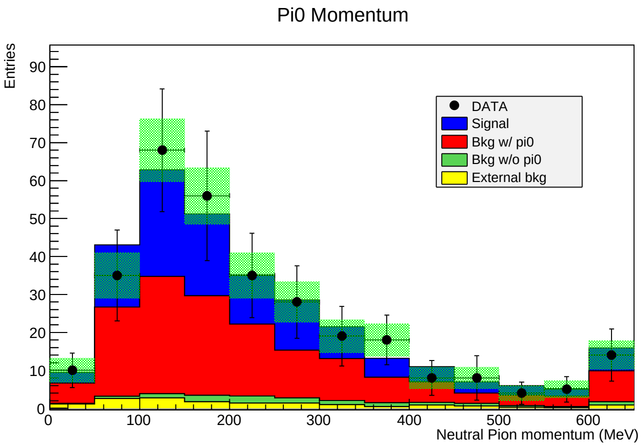

Figure 7.3.3: *Neutral pion candidate momentum after the fit for both DATA and MC, for selected CC-π^0 events in the MRD-matched sample. The DATA statistical errors are shown with green boxes, while the black error bars give the total (statistical plus systematic) uncertainties.*

The left panel in Fig. 7.4.1 shows the reconstructed π^0 invariant mass distribution of the selected CCπ^0 inclusive events, that is events with a μ^+, a π^0 and any other particle(s) in the final state. Preliminary results for a CCπ^0 exclusive selection consisting of the three-body final state (μ^+, π^0, n) were also presented. Once events in the 70-200 MeV/c^2 invariant mass range are selected, a CCπ^0 inclusive purity (efficiency) of 54% (4.2%) is expected. With about 10^{20} accumulated protons on target, more than $3 \cdot 10^3$ antineutrino-induced CCπ^0 event candidates were selected. These preliminary results suggest a measured CCπ^0 event rate that is somewhat lower than expectations based on the GENIE neutrino event generator [72]. First steps toward the measurement of the CCπ^0 cross section were also presented in [71], accounting for backgrounds, detector resolution and signal efficiency. The right panel of Fig. 7.4.1 shows the energy dependence of the total CCπ^0 cross section as a function of neutrino energy. For this plot, data and expectations are normalized to each other. From this plot, the simulation appears to reproduce well the shape of the CCπ^0 cross section as a function of neutrino energy as measured by MINERvA.

The T2K (Tokai-to-Kamioka) experiment is a long baseline neutrino os-

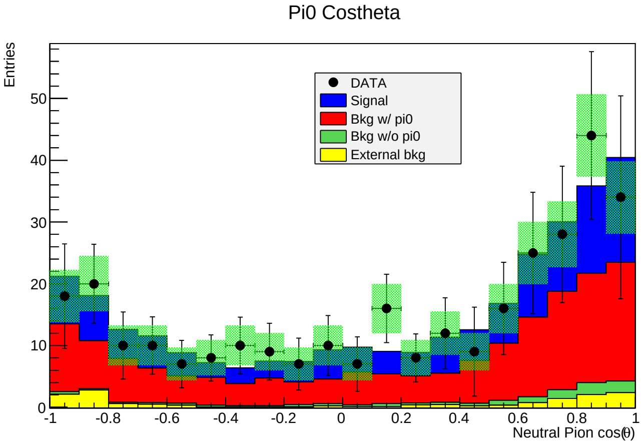

Figure 7.3.4: *Cosine of the angle between the* π^0 *candidate direction and the beam direction after the fit for both DATA and MC, for selected CC-*π^0 *events in the MRD-matched sample. The DATA statistical errors are shown with green boxes, while the black error bars give the total (statistical plus systematic) uncertainties.*

cillation experiment. T2K's physics goals include precision measurements of the oscillation parameters ϑ_{13}, Δm^2_{23} and ϑ_{23}. T2K's far detector is Super-Kamiokande, located at a 295 km baseline from neutrino production in Tokai. In addition to neutrino oscillation studies, the T2K neutrino beam (with $E_\nu \sim 1$ GeV) and the T2K near detector complex at 280 m from the production target (ND280) enable in-depth neutrino interaction studies at energies covering the transition between the resonance production and the deep inelastic regimes. ND280 is a magnetized off-axis tracking detector. The off-axis detector elements are contained inside the CERN UA1 magnet. A pi-zero detector (PØD), consisting of tracking planes of scintillator bars alternating with either water target/brass foil or lead foil, is located at the upstream end of the magnet. Downstream of the PØD, the tracker, comprising three Time Projection Chamber (TPC) and two Fine Grained Detector (FDG) consisting of layers of finely segmented scintillating bars, is designed to measure charged current interactions in the FDGs. The PØD, TPCs, and FDGs are all surrounded by an electromagnetic calorimeter (ECal) for detecting γ-rays that do not convert in the inner detectors, while the return yoke of the magnet is

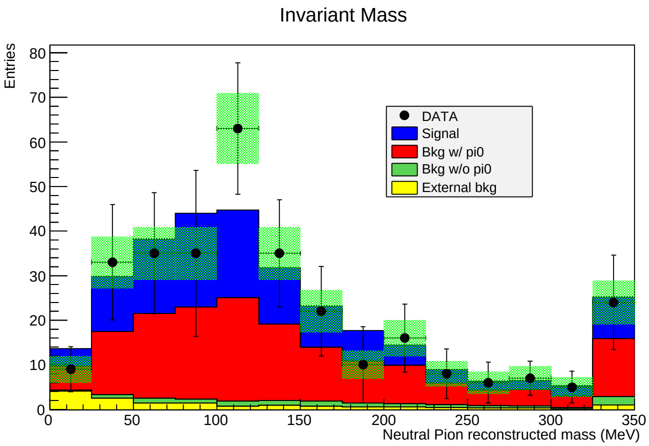

Figure 7.3.5: *Neutral pion candidate reconstructed mass after the fit for both DATA and MC, for selected CC-π^0 events in the MRD-matched sample. The DATA statistical errors are shown with green boxes, while the black error bars give the total (statistical plus systematic) uncertainties.*

instrumented with scintillator to measure the ranges of muons that exit the sides of the off-axis detector. T2K began accumulating neutrino beam data for physics analysis in 2010, and data corresponding to more than $6 \cdot 10^{20}$ protons on target have already been collected. Expectations for ν_μ CCπ^0 interaction studies in the tracker of the ND280 detector were presented in [73].

The expected topology for a ν_μ CCπ^0 interaction in the ND280 tracker is shown in Fig. 7.4.2. Events are selected by requiring a muon and at least two π^0 decay products. The neutrino interaction vertex is assumed to be the muon track upstream position, and is required to be within the FGD1 Fiducial Volume. The muon track is required to reach TPC2, and to be compatible with a muon-like dE/dx profile in the TPC. As shown in Fig. 7.4.2, photons from π^0 decay can be identified upon conversion either as showers in the calorimeter or as electron-positron pairs in the TPC. The current event selection predicts a ν_μ CCπ^0 purity (efficiency) of 62% (32%). The analysis of ND280 real data is currently underway.

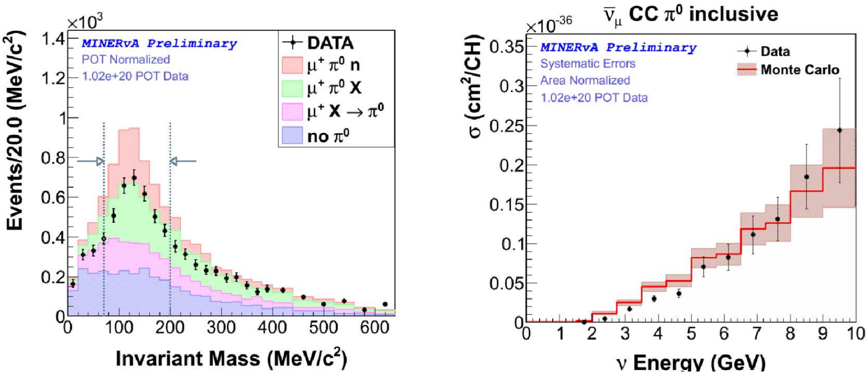

Figure 7.4.1: Left: *preliminary Data/MC comparison of reconstructed* π^0 *invariant mass in MINER*ν*A. Antineutrino-induced CC*π^0 *inclusive events are events with either a* (μ^+, π^0, n) *final state (red), or* (μ^+, π^0, X) *(green). Only events with an invariant mass between 70 and 200 MeV/*c^2 *are selected.* Right: *preliminary total observable* $\bar{\nu}_\mu$ *CC*π^0 *inclusive cross-section as a function of neutrino energy in MINER*ν*A. Data and MC are area-normalized, in the right panel.*

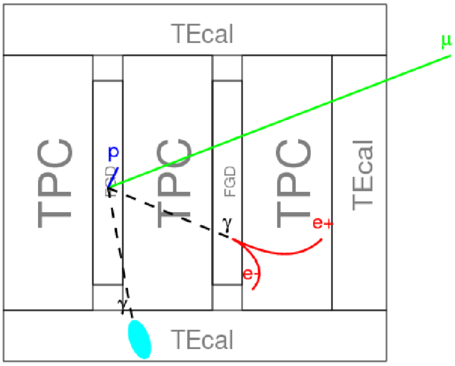

Figure 7.4.2: *Schematic of how a CC*π^0 *interaction manifests itself in the tracker part of the T2K ND280 near detector.*

Chapter 8

Conclusions

Neutrinos have recently provided indication for physics beyond the Standard Model of particle physics via the discovery of flavor oscillations. For this reason, oscillation experiments are presently the main focus of the neutrino community. We have now entered a phase of precision neutrino oscillation measurements, such as the recent T2K evidence for sub-leading $\nu_\mu \rightarrow \nu_e$ oscillations with an accelerator-based neutrino source.

Those precission measurements impose a challenging requirements on our knowledge of neutrino interactions with target nuclei. This is particulary true in the few-GeV neutrino energy region. This is the most relevant region for neutrino oscillation experiment, yet the least understood one, with most of experimental input dating back to the 70's and 80's.

New cross section measurements are needed to meet the necessary understanding of neutrino interactions of both signal and background components in neutrino oscillation searches. SciBooNE is part of this new program, together with the MINERvA experiment and near detectors at oscillation experiments. SciBooNE cross section measurements are particularly relevant as input to T2K analyses, given the similarity in the neutrino energy spectrum between the two experiments.

SciBooNE already reported cross section measurements in various channels, as summarized in Sec.2.5, including: charged-current inclusive, CC quasi-elastic, CC single charged pion production, and neutral-current neutral pion production channels. Other experiments are also contributing to producing new neutrino-nucleus cross section results.

This thesis focuses on the measurement of charged-current neutral pion production (CC-π^0) in neutrino interactions with a CH target. This channel is particularly important for oscillation measurements relying on Cherenkov detectors, such as the far detector of T2K, because neutral pions are an important contribution to the background in $\nu_\mu \to \nu_e$ appearance measurements.

In this analysis a CC-π^0 event is defined by its final state. One muon and one neutral pion are required to come out from the target nucleus, while nucleons and charged pions are allowed but not required ($\nu_\mu + N- > \mu - +\pi^0 + N' + X$).

This is an important but notoriously difficult measurement because it requires the use of the three SciBooNE sub-detectors (SciBar, EC and MRD). It is also the only analysis in SciBooNE where a minimum of three reconstructed tracks are required, one from the muon and two from each one of the two neutral pion decay gammas. Finally, since the CC-π^0 cross section represents only about a 7% fraction of the total CC cross section at SciBooNE energies, backgrounds are significant and need to be well understood.

As part of my work related to the SciBooNE detector construction and commissioning, I have been involved in the SciBar geometry alignment analysis and in the MRD sub-detector construction. In particular, I have been responsible of the refurbishment of the MRD photomultiplier tubes (re-used from previous experiments), of the construction of the MRD scintillator modules and of the MRD cabling.

Concerning the reconstruction of CC-π^0 interactions, I have extended and improved the standard SciBar reconstruction algorithms used in previous SciBooNE analyses (see Sec. 4.7), increasing the efficiency for large track multiplicity events and for large angle tracks.

With respect to the low rate of CC-π^0 events, I have developed a robust analysis technique using a data-driven approach to measure backgrounds (Sec. 5.3), complemented with a detailed systematic error evaluation (Chap. 6).

The three main results obtained in this analysis, reported in Chapter 7, are as follows:

Flux-averaged CC-π^0 cross section: the flux-averaged cross section has been measured to be: $\langle \sigma_{\mathrm{CC}-\pi^0} \rangle_\phi = (5.6 \pm 1.9_{\mathrm{fit}}{}^{+0.9}_{-1.1}{}_{\mathrm{syst}}) \times 10^{-40}$ cm^2/N at a mean neutrino energy of 0.89 GeV. This result can be directly compared with the CC-π^0 cross section result of the MiniBooNE experiment. As can be seen in Tab. 7.1.1, the measurements are consistent, increasing the confidence in both experimental results. Table 7.1.1 also shows the comparison with the NEUT event generator prediction. Good agreement is found also in this case, indicating that the NEUT modelling of neutral pion production in charged-current neutrino interactions is adequate at SciBooNE energies.

CC-π^0 cross section energy dependence: the NEUT CC-π^0 cross section energy dependence prediction can be checked using MiniBooNE and SciBooNE data. From Fig. 7.2.1 we can observe that NEUT accurately reproduces the energy dependence measured by MiniBooNE. SciBooNE, on the other hand, does not have enough statistics to perform an energy-binned measurement of the CC-π^0 production cross section as MiniBooNE did. Nevertheless, an indication of the adequacy of the NEUT energy dependence modelling can be obtained in this case by comparing the reconstructed neutrino energy distribution obtained in the SciBooNE broad-band spectrum with NEUT-based simulations. As shown in Fig. 7.2.4, the simulation reproduces well the SciBooNE energy distribution.

Kinematics of final state particles: the production kinematics of the final state particles (μ, π^0) has also been studied and compared with NEUT expectations. A good agreement between data and expectations is generally found, with the possible exception of the forward muon direction (see Figs. 5.2.3 and 7.3.2). We conclude that the nominal NEUT simulation already provides a fair description of SciBooNE CC-π^0 data kinematics distributions, and that this description can be further improved with a simple renormalization of the signal and background components in our fit.

List of Figures

List of Tables

Glossary

ADC	Analogical to Digital Converter. 1, 42–47, 50, 51, 56
BNB	Booster Neutrino Beam. vii, 1, 15–17, 30, 31
DIS	Deep Inelastic Scattering. 1, 7, 8, 11, 12, 38, 40, 64
EC	Electron Catcher. vii, viii, x, xi, 1, 15, 22–25, 34, 43, 51, 52, 57, 65, 68, 69, 71, 82, 117
FDG	Fine Grained Detector. 1, 113
FNAL	Fermi National Accelerator Laboratory. vii, 1, 20, 26, 47
FSI	Final State Interactions. xii, 1
FV	Fiducial Volume. x, xii, 1, 65, 88, 89, 114
GEANT4	simulation software. viii, 1, 34, 36, 42, 43
MA-PMT	Multi-Anode Photo-multiplier. viii, xiii, xiv, 1, 18, 20, 22, 46, 47, 49, 94
MC	Monte-Carlo. viii, ix, xii–xv, 1, 34, 36, 44, 49, 58, 65, 67, 69, 74, 75, 79, 81–88, 90, 91, 95, 97, 103, 106–110
MIP	Minimum Ionizing Particle. 1, 46, 47, 63, 69
MRD	Muon Range Detector. vii–x, 1, 15, 22, 25–27, 34, 44, 52, 56–58, 65, 67, 75, 82, 107, 117
MuCL	Muon Confidence Level. xi, 1, 59, 63, 69
NEUT	The default SciBooNE neutrino event generator. viii, xiv, 1, 34, 36, 41, 42, 91, 93, 103–106, 108, 110, 117, 118
NUANCE	neutrino event generator used by MiniBooNE and to evaluate some SciBooNE systematics. 1, 93

p.e.	photo-electrons. xiv, 1, 43, 44, 46, 47, 63, 95
PMT	Photo-Multiplier Tube. xiv, 1, 22, 24–27, 42, 43, 45, 46, 50, 52, 56, 94, 95
POT	Protons On Target. viii, 1, 16, 41, 65, 75, 84, 88, 90, 92
QE	Quasi-Elastic. 1, 11, 12
sbcat	SciBar Cellular Automaton Tracker. viii, ix, 1, 53, 61, 62
TDC	Time to Digital Converter. viii, xiv, 1, 22, 42–44, 50, 52, 58, 94, 95
TPC	Time Projection Chamber. 1, 113, 114
WLS	wavelength shifting. 1, 18, 20

Bibliography

[1] J. L. Alcaraz-Aunion and J. Catala-Perez, AIP Conf. Proc. **967** (2007) 307.

[2] W. Pauli, Phys. Today **31N9** (1978) 27.

[3] E. Fermi, Z. Phys. **88**, 161 (1934).

[4] F. Reines and C. L. Cowan, Phys. Rev. **92** (1953) 830.

[5] S. Sakata, Prog. Theor. Phys. **16** (1956) 686.

[6] G. Danby, J. M. Gaillard, K. A. Goulianos, L. M. Lederman, N. B. Mistry, M. Schwartz and J. Steinberger, Phys. Rev. Lett. **9** (1962) 36.

[7] R. Davis, Jr., D. S. Harmer and K. C. Hoffman, Phys. Rev. Lett. **20** (1968) 1205.

[8] B. Pontecorvo, Sov. Phys. JETP **6** (1957) 429 [Zh. Eksp. Teor. Fiz. **33** (1957) 549].

[9] Z. Maki, M. Nakagawa and S. Sakata, Prog. Theor. Phys. **28** (1962) 870.

[10] M. L. Perl, G. J. Feldman, G. S. Abrams, M. S. Alam, A. Boyarski, M. Breidenbach, J. Dorfan and W. Chinowsky *et al.*, Phys. Lett. B **70** (1977) 487.

[11] W. Gajewski [IMB Collaboration], Nucl. Phys. Proc. Suppl. **28A**, 161 (1992).

[12] Y. Fukuda *et al.* [Kamiokande Collaboration], Phys. Lett. B **335** (1994) 237.

[13] C. B. Bratton *et al.* [IMB Collaboration], Phys. Rev. D **37** (1988) 3361.

[14] K. Hirata *et al.* [KAMIOKANDE-II Collaboration], Phys. Rev. Lett. **58** (1987) 1490.

[15] Y. Fukuda *et al.* [Super-Kamiokande Collaboration], Phys. Rev. Lett. **81** (1998) 1562 [hep-ex/9807003].

[16] K. Kodama *et al.* [DONUT Collaboration], Phys. Lett. B **504** (2001) 218 [hep-ex/0012035].

[17] Q. R. Ahmad *et al.* [SNO Collaboration], Phys. Rev. Lett. **87** (2001) 071301 [nucl-ex/0106015].

[18] K. Eguchi *et al.* [KamLAND Collaboration], Phys. Rev. Lett. **90** (2003) 021802 [hep-ex/0212021].

[19] M. H. Ahn *et al.* [K2K Collaboration], Phys. Rev. D **74** (2006) 072003 [hep-ex/0606032].

[20] P. Adamson *et al.* [MINOS Collaboration], Phys. Rev. Lett. **101** (2008) 131802 [arXiv:0806.2237 [hep-ex]].

[21] K. Abe *et al.* [T2K Collaboration], Phys. Rev. Lett. **107** (2011) 041801 [arXiv:1106.2822 [hep-ex]].

[22] F. P. An *et al.* [DAYA-BAY Collaboration], Phys. Rev. Lett. **108** (2012) 171803 [arXiv:1203.1669 [hep-ex]].

[23] J. K. Ahn *et al.* [RENO Collaboration], Phys. Rev. Lett. **108** (2012) 191802 [arXiv:1204.0626 [hep-ex]].

[24] T. .Eberl [ANTARES Collaboration], eConf C **1111101** (2011) 1 [arXiv:1205.2173 [astro-ph.HE]].

[25] S. Boser [IceCube Collaboration], arXiv:1205.6405 [astro-ph.HE].

[26] Z. Djurcic [MiniBooNE Collaboration], arXiv:1201.1519 [hep-ex].

[27] R. D. Ransome [MINERvA Collaboration], AIP Conf. Proc. **1441** (2012) 411.

[28] Y. Hayato, Acta Phys. Polon. B **40**, 2477 (2009).

[29] D. Rein and L.M.Sehgal, Ann. of Phy. **133** 1780 (1981).

[30] J. Beringer *et al.* [Particle Data Group Collaboration], Phys. Rev. D **86**, 010001 (2012).

[31] D. Casper, Nucl. Phys. Proc. Suppl. **112**, 161 (2002) [hep-ph/0208030].

[32] A. A. Aguilar-Arevalo *et al.* [MiniBooNE Collaboration], Phys. Rev. D **83**, 052009 (2011) [arXiv:1010.3264 [hep-ex]].

[33] A. A. Aguilar-Arevalo *et al.* [SciBooNE Collaboration], hep-ex/0601022.

[34] K. Nitta *et al.* "The K2K SciBar Detector", Nucl. Instr. And Meth. A**535**: 147-151 (2004).

[35] Construction and test of calorimeter modules fot the CHORUS experiment, Nucl. Instr. And Meth. A**349**: 70-80 (1994).

[36] K. Kaneyuki (T2K Collaboration), "T2K experiment", Nucl. Phys. Proc. Suppl. **145**: 178-181, (2005).

[37] K. Hiraide [SciBooNE Collaboration], arXiv:0810.3903 [hep-ex].

[38] Y. Kurimoto *et al.* [SciBooNE Collaboration], Phys. Rev. D **81** (2010) 033004 [arXiv:0910.5768 [hep-ex]].

[39] Y. Kurimoto *et al.* [SciBooNE Collaboration], Phys. Rev. D **81** (2010) 111102 [arXiv:1005.0059 [hep-ex]].

[40] A.A. Aguilar-Arevalo *et al.* (MiniBooNE Collaboration), "Measurement of muon neutrino quasi-elastic scattering on carbon", Phys. Rev. Lett. **100** (2008) 032301, e-Print: arXiv:0706.0926 [hep-ex]

[41] H. Chen *et al.* [MicroBooNE Collaboration], FERMILAB-PROPOSAL-0974.

[42] A. A. Aguilar-Arevalo *et al.* [MiniBooNE Collaboration], Phys. Rev. D **79** (2009) 072002 [arXiv:0806.1449 [hep-ex]].

[43] S. Agostinelli *et al.* [GEANT4 Collaboration], Nucl. Instrum. Meth. A **506**, 250 (2003).

[44] K. Hiraide *et al.* [SciBooNE Collaboration], Phys. Rev. D **78**, 112004 (2008) [arXiv:0811.0369 [hep-ex]].

[45] M. Hasegawa *et al.* [K2K Collaboration], Phys. Rev. Lett. **95**, 252301 (2005) [hep-ex/0506008].

[46] D. Rein and L. M. Sehgal, Nucl. Phys. B **223**, 29 (1983).

[47] Y. Hayato, Nucl. Phys. Proc. Suppl. **112**, 171 (2002).

[48] D. Rein and L. M. Sehgal, Phys. Lett. B **657**, 207 (2007) [hep-ph/0606185].

[49] E. A. Paschos, A. Kartavtsev and G. J. Gounaris, Phys. Rev. D **74**, 054007 (2006) [hep-ph/0512139].

[50] L. Alvarez-Ruso, L. S. Geng, S. Hirenzaki and M. J. Vicente Vacas, Phys. Rev. C **75**, 055501 (2007) [Erratum-ibid. C **80**, 019906 (2009)] [nucl-th/0701098].

[51] D. Rein and L. M. Sehgal, Annals Phys. **133**, 79 (1981).

[52] Y. Itow *et al.* [T2K Collaboration], hep-ex/0106019.

[53] Y. Nakajima *et al.* [SciBooNE Collaboration], Phys. Rev. D **83**, 012005 (2011) [arXiv:1011.2131 [hep-ex]].

[54] J. L. A. Aunion, FERMILAB-THESIS-2010-45.

[55] Y. Nakajima [SciBooNE Collaboration], AIP Conf. Proc. **1405**, 47 (2011).

[56] A. A. Aguilar-Arevalo *et al.* [MiniBooNE Collaboration], Phys. Rev. D **81**, 092005 (2010) [arXiv:1002.2680 [hep-ex]].

[57] VLyubushkin *et al.* [NOMAD Collaboration], Eur. Phys. J. C **63**, 355 (2009) [arXiv:0812.4543 [hep-ex]].

[58] K. B. M. Mahn *et al.* [SciBooNE and MiniBooNE Collaborations], Phys. Rev. D **85**, 032007 (2012) [arXiv:1106.5685 [hep-ex]].

[59] G. Cheng *et al.* [MiniBooNE and SciBooNE Collaborations], Phys. Rev. D **86**, 052009 (2012) [arXiv:1208.0322 [hep-ex]].

[60] K. N. Abazajian, M. A. Acero, S. K. Agarwalla, A. A. Aguilar-Arevalo, C. H. Albright, S. Antusch, C. A. Arguelles and A. B. Balantekin *et al.*, arXiv:1204.5379 [hep-ph].

[61] G. Cheng *et al.* [SciBooNE Collaboration], Phys. Rev. D **84**, 012009 (2011) [arXiv:1105.2871 [hep-ex]].

[62] R. P. Feynman, Phys. Rev. Lett. **23**, 1415 (1969).

[63] A. Dellacqua, G. Parrour, S. Giani, P. Kent, A. Osborne, S. Ravndal, L. Silvestris and H. Fesefeldt *et al.*, CERN-DRDC-94-29.

[64] M. G. Catanesi *et al.* [HARP Collaboration], Eur. Phys. J. C **52** (2007) 29 [hep-ex/0702024].

[65] C.H. Llewellyn Smith, Phys. Rep. 3C 261 (1972).

[66] M. Gluck, E. Reya and A. Vogt, Eur. Phys. J. C **5**, 461 (1998) [hep-ph/9806404].

[67] A. Bodek and U. K. Yang. Modeling deep inelastic cross section in the few GeV region. Nucl. Phys. Proc. Suppl., **112**:70-76, 2002.

[68] D. Rein and L.M. Sehgal, "Coherent pi0 Production in Neutrino Reactions", Nucl. Phys. B**223** 29 (1983).

[69] L. L. Salcedo, E. Oset, M. J. Vicente-Vacas and C. Garcia-Recio, Nucl. Phys. A **484**, 557 (1988).

[70] W. M Yao *et al.* (Particle Data Group), Journal of Physics G**33** 1 (2006).

[71] J.L. Palomino and A. Higuera on behalf of the MINERvA collaboration, "Coherent and neutral pion production results from MINERvA," 8th International Workshop on Neutrino Nucleus Interactions in Few-GeV Region (NuInt 12), `https://indico.fnal.gov/contributionDisplay.py?contribId=80&sessionId=17&confId=5361`

[72] L. Fields *et al.* [MINERvA Collaboration], Phys. Rev. Lett. 111, **022501** (2013) [arXiv:1305.2234 [hep-ex]].

[73] M. Batkiewicz on behalf of the T2K collaboration, "ν_μ CCπ^0 reaction in the Tracker of the ND280 detector in the T2K experiment," 8th International Workshop on Neutrino Nucleus Interactions in Few-GeV Region (NuInt 12), `https://indico.fnal.gov/contributionDisplay.py?contribId=47&sessionId=16&confId=5361`